Investigation and Application of Microscale Semiconductor Lasers and Cavities

Thesis by

Raviv Perahia

In Partial Fulfillment of the Requirements

for the Degree of

Doctor of Philosophy

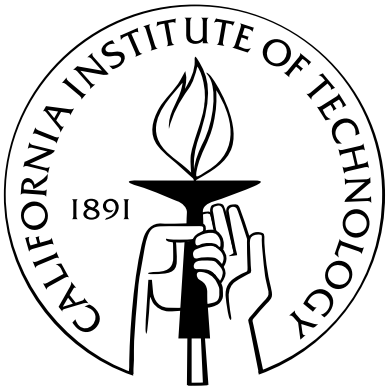

California Institute of Technology

Pasadena, California

2009

(Defended May 21, 2009)

To my mother, father, and brother

Acknowledgements

First and foremost I must thank my advisor Professor Oskar Painter. His charisma, excitement, and extreme doggedness is what first drew me to his lab and kept me going.

Our group has been a great source of scientific curiosity and strength. I heartily thank the senior members of the group Kartik Srinivasan, Paul Barclay, Matt Borselli, and Tom Johnson for taking me in when I joined. We have had many, great, scientific and philosophical discussions over the years. My first instinct whether I am in need of a brainstorm, a discussion, or help dealing with an unruly clean room tool, is to walk down the hallway to seek their council. But alas, they have moved on.

I thank Chris Michael, Jessie Rosenberg, Qiang Lin, Matt Eichenfield, Thiago Alegre, Ryan Camacho, Amir Safavi-Naeini, Jasper Chan, and Jeff Hill for an increasingly interesting and dynamic scientific atmosphere. Chris has been a supportive partner in stress over the past several months. Special thanks goes my office mates Jessie, Qiang, and Thiago. Jessie has been my office mate for the past 5 years and that should speak for itself, it has been a pleasure. I also thank Orion Crisafulli for the interesting time we had sharing an office together in the beginning of both of our graduate careers. I can not think of a better situation than having Qiang sitting right next to me, as his physical intuition and open willingness to teach has been a great help. Finally, while Thiago is a fairly recent addition to our group, he has breathed new life into several projects I've been working on. His enthusiasm is contagious and I can not thank him enough.

I would like to thank my committee, Professors Axel Scherer, Kerry Vahala, and Changhuei Yang for always supportive interaction over the past several years.

I can not thank enough the countless graduate students and staff members that I have interacted with over the years at Caltech. I do not recall a single instance where someone did not take at least 10 minutes of the their time, if not much more, to help me or give me their perspective. Particular thanks goes to Joyce Poon for help with initial metal deposition at Caltech.

Outside of Caltech I have had the pleasure of interacting with the groups of Professor F. Capasso

at Harvard and R. Colombelli at Universite Paris-Sud 11. I worked very closely with Virginie Moreau and my special thanks to Michael Bahriz for showing me Paris by bicycle.

I must thank the staff of the Kavli Nanoscience Institute: Guy DeRose, Melissa Melendes, Bophan Chhim, and Mary Sikora. Guy DeRose has been of particular help during several research critical moments. There are portions of this thesis that could not have been done without the proficient use of the Leica beam writer. For instruction and help on the tool I must thank Matt Matheny, Derrick Chi, Uday Khankhoje, Mike Shearn, and Jingqing Huang.

I must also thank Joe Haggerty at the Aero Machine shop and his crew Ali Kiani and Bradley S. John. In the physics machine shop I thank Mark Gonzales for taking the time to train me. Project manager Mark Trojanowski and I have had a chance to collaborate on the building of several labs at Caltech, a process that I have very much enjoyed.

My graduate career could not have ever progressed without the help of Cierina Marks at just the right moment. I have also thoroughly enjoyed my always great and efficient interaction with Lyn Hein. It has been a special treat to interact with the support staff at Caltech including the cut shop, transportation, the general stockroom, electric shop, and last but not least the HVAC department. I have spent many hours sweating with these guys trying keep our labs up and running.

Part of the reason I chose to pursue graduate work is directly due to my interaction with Boston University Professors Anna Swan, Bennett Goldberg, Selim Ünlü, Karl Ludwig, and Shyam Erramilli. I thank them for their tutelage, inspiration, and motivation.

Finally to the most important thank you. I could not have done this without the extremely rich and stimulating environment my mother, father, and bother have given me. They provided great support through the ups and downs of graduate school.

Last but not least I must thank a close group of friends at Caltech that have kept me going. Special appreciation goes to Waheb Bishara, Jen Dionne, Deepak Kumar, and Jenn Stockdill. I also must thank my friends from home and college that have accepted me as a friend even after great periods of neglect.

Abstract

As optical, active, semiconductor devices are miniaturized to the wavelength scale, many applications of cavities, lasers, and detectors become possible. In order to make such devices useful in real-world applications one must first understand how these devices behave when they are reduced in size and what technological barriers must be overcome.

In this dissertation several thrusts are presented toward the investigation and application of microscale active semiconductor cavities. Work is divided into four thrusts: fluid sensing based on surface sensitive quantum cascade lasers, hybridization of surface plasmon modes and waveguide modes as well as lasing in near-infrared subwavelength microdisks, quantum dot based cavities for strong coupling, and nascent work on optomechanical tuning of active cavities. In all four thrusts design and fabrication techniques are used to overcome challenges and capitalize on reduced scale.

Progress in fabrication, design, and testing of surface sensitive quantum cascade lasers is presented. Work focuses on increasing surface sensitivity by modifying the metal contacts on top of active material originally intended to be used with a surface plasmon waveguide. An experiment where isopropyl and ethyl alcohol is differentiated based on laser behavior is carried out. Work toward integration of semiconductor lasers with fluidic delivery systems is explored.

Work then turns to the intimate and advantageous inclusion of metal into subwavelength strained quantum well microdisk lasers in the near-infrared. Optical and thermal characteristics are simulated. Hybridization of surface plasmon mode and waveguide whispering-gallery modes is simulated and experimentally verified. Lasing behavior of such small devices is investigated.

In parallel, work toward improving the probability of achieving a strongly coupled quantum dot microdisk cavity system is carried out. Improvements in fabrication techniques and potential metal integration makes this project a natural extension of the subwavelength microdisk laser project.

Finally, a new project is discussed where the above projects are combined with investigation of optomechanical systems currently ongoing in our lab. Work toward the combination of active optical cavities with optomechanical devices will lead to wide band wavelength tuning functionality.

Contents

List of Figures

List of Tables

Chapter 1

Introduction

This dissertation is a culmination of work tied together by an overreaching goal: understanding the behavior of microscale active optical cavities and leveraging that knowledge to design and create such devices for real-world applications. As this work spans several different projects, I would like to use this introduction to give the reader an overview and motivation for the progression of this work. Background on each project will be provided in subsequent chapters. Research described in this thesis, as is typical in our lab, involves all aspects of research in semiconductor device physics, all carried out in-house: design, fabrication, testing, and modeling. I would therefore like to also give the reader some insight into the tremendous effort necessary to keep such an endeavor working over several years. Namely the upkeep and development of infrastructure and equipment, as well as the fabrication process development that is a combination of science and a finely tuned black art. This work is divided into four major thrusts. (i) The development of fluid/surface sensitive Quantum Cascade (QC) lasers for absorption spectroscopy in the mid infrared (mid-infrared). (ii) The development of sub-wavelength hybrid surface plasmon-waveguide mode lasers. (iii) Improving techniques for achieving a strongly coupled microdisk cavity quantum dot system. (iv) The initial development and design of optomechanically tuned active cavities.

When I first joined the group, one project that especially caught my interest was the potential to expand the use of quantum cascade lasers (QCLs) as chemical sensors in the mid-infrared beyond gas sensing [9]. Recent success in fabrication and testing of quantum cascade photonic crystal surface emitting lasers (QC-PCSELs) [10], as well mid-infrared absorption spectroscopy investigations by M. Miller, including the study of an Alzheimer's related protein β amyloid [2], led to the idea of applying the use of QC-PCSELs toward fluidic delivery based mid-infrared spectroscopy. As a stepping stone, I began working with Professor O. Painter and graduate student J. Rosenberg on PC resonant detectors in the mid-infrared. We pattered gallium arsenide (GaAs) based, quantum dot in

well (DWELL), detector material. This is where I learned the basics of electron beam lithography, plasma based dry etching and deposition, as well as general semiconductor processing.

Once we met with some success in fabrication and testing, J. Rosenberg took over the project and I turned toward the design and fabrication a fluidic mid-infrared absorption spectroscopy sensors using a QC-PCSELs. As the PC holes are reminiscent of "test tubes," the goal was to flow an analyte into the holes and detect its presence through the laser response. The hope was that new advances in QC materials as well as improved design and fabrication techniques would yield lasing at room temperature allowing for integration with a fluidic delivery apparatus. Significant work went into development of an electron beam lithography process that was originally carried out at Bell Labs and was transferred to Caltech. Changing the order of fabrication steps to eliminate metal deposition within PC holes that led to optical loss, as well as use of SiN_x hard mask instead of SiO_2, led to the development of very deep plasma etches for both the hard mask, QC, and indium phosphide (InP) material. Such process development combined with hardware failure has led to my intimate involvement in the maintenance of the Oxford plasma etching and deposition tools. We were able to get PC lasers operating up to liquid nitrogen (LN_2) temperatures and microdisk lasers operating up to room temperature. Since room temperature operation is necessary for sensing, a parallel avenue toward sensing was pursued. Significant simulation and modeling efforts were undertaken to design optical microdisk cavities and ridge waveguide cavities optimized for sensing. Simulations were based on a laser epitaxial structure originally intended to be used with a surface plasmon (SP) waveguide. This means that the active material is not buried under a waveguide layer but is very near the surface. Designs showing that receding the SP metal contact as well as removing the highly doped top layer, originally designed as an ohmic contact, significantly reduces the loss while increasing sensitivity. A proof of concept experiment of sensing typical laboratory solvents was carried out on a surface sensitive air confined ridge waveguide laser. Concurrently, an effort to integrate QC laser chips with polymer based microfluidics was carried out. Microfluidic chips were fabricated from Polydimethylsiloxane (PDMS) and methods for overcoming the strong infrared absorption of the PDMS were explored. This work will be presented slightly out of order, instead starting with the design of surface sensitive laser cavities, continuing with an overview of fabrication and testing of all laser structures, and ending with the fluid sensing.

The quantum cascade portion of this thesis work was done in close collaboration with two groups. Initial work was carried out in collaboration with the Harvard (Boston, MA) group of Professor F. Capasso where we got QC material pre processed with the top contact. Using this

material we developed the PC lithography including beam writing and etching. The brunt of the collaboration moved from Harvard to the group of Professor R. Colombelli at the Universite de Paris-Sud 11 (Orsay, France). The leading graduate student there was Virginie Moreau. For the photonic crystal and microdisk work the Paris-Sud group would preprocess material from Sheffield University (Sheffield, England) and send it to Caltech. We would design and pattern the photonic crystal and disk cavities and send them back to the Paris-Sud group to be wire bonded and tested. The Paris group led the fabrication of air-confined ridge waveguide lasers based on air-confined designs by us. I traveled to Paris-Sud to carry out the sensing experiment in collaboration with V. Moreau bringing along the fluid delivery apparatus and imaging system. The project culminated in the successful demonstrations of the ability to distinguish isopropyl and ethyl alcohol based on laser spectral behavior. In parallel to experiments in France we built a lab specifically for the testing of quantum cascade lasers. This includes the lab infrastructure, the purchase of an advanced Fourier transform infrared spectrometer (FTIR) with step scan capability, and building a photoluminescence setup in the mid-infrared. Two summer undergraduate students aided in the development of PDMS chips and a surface binding technique for proteins.

After three years and significant fabrication and design effort, work on the QC sensing project tapered off due to dwindling availability of QC material. As the QC work was part of an interesting optofluidic grant program, some efforts were made to develop other optofluidic based devices in more manageable wavelengths, i.e., near-infrared or visible. For example, a brief attempt to make a laser dye based SiN_x microdisk laser was carried out. While this mini project was abandoned, SiN_x microdisks were later used to demonstrate optomechanical coupling by M. Eichenfield [11]. The interest in porting our optical designs to the near-infrared where laser material is much more abundant coupled with a new funding program aided in a change of research path.

My work then shifted toward exploring small microdisk sub-wavelength lasers in the near-infrared ($\lambda = 1.3\mu$m). The primary goal was to explore laser phenomena when the cavity supports very few optical modes, i.e., threshold, line width enhancement, and photon correlation. The goal was to not only study the physics of small lasers but also to incorporate them into technologically useful geometries and devices. Many lessons learned from the development of QC lasers for sensing were applied to the design of sub-wavelength lasers. Since metal contacts must be incorporated into these lasers, in the future for electrical injection, we investigated how to intimately include metal into laser cavities and benefit. Instead of just suffering optical loss, we were interested in how enhanced confinement due to surface plasmon modes and enhanced thermal properties could

aid in lasing. Work focused on the design, fabrication, and testing of optically pumped GaInAsP strained quantum well lasers. Fabrication and testing has been carried out on optically pumped laser material but with a constant focus on moving toward electrically pumped geometries. Work has centered around simulated and experientially verified surface plasmon mode and whispering gallery waveguide mode hybridization. Further fabrication efforts focused on moving from optically pumped structures to electrically pumped structures. Several different fabrication paths were explored before a successful path was chosen. An air bridging technique using a low optical loss polymer was developed for future experiments.

The sub-wavelength laser portion of this thesis work was carried out entirely at Caltech with the exception of the epitaxial growth of the laser material that was carried out at Bell Labs [12]. Device fabrication and development was first carried out entirely in our clean room. An electron beam evaporator was installed and fixed by me and fellow graduate student J. Rosenberg. Due to a flood in the lab the plasma etching tool had to be resuscitated. Substantial effort went into upgrading our custom scanning electron microscope (SEM) based beam writing system to allow for aligned lithographies. Eventually, highly precise aligned lithography procedures were achieved using the commercial beam writer found in Caltech's Kavli Nanoscience Institute facility. Focused ion beam inspection was used in the development process. Optical testing involved first disassembling and then reassembling the photoluminescence setup due to a laboratory move from Steele Labs to Watson Labs. T. Alegre joined our group as a posdoc and this project during the optical testing phase. We have collaborated on projects since then.

In parallel to the development of sub-wavelength hybrid mode lasers, work was carried out toward a strongly coupled quantum dot (QD) and optical microcavity system. After initial demonstration by Srinivasan and Painter [13] it became clear that both projects share experimental and technology development goals. In both cases the next experimental step is to look at photon statistics using a Hanbury-Brown-Twiss (HBT) setup at $\lambda = 1.3\mu$m. This is a bit of a challenge over HBT measurements at shorter wavelengths, as the best single photon counters at $\lambda = 1.3\mu$m work in Geiger mode. Furthermore, the incorporation of metal contacts into or at least in very close proximity of a small mode volume cavity is the next necessary step in the development of the QD experiments. Such a contact would allow for QD charge control and application of a strong electric field to the QD. The method for fabrication a strongly coupled QD-microdisk cavity system is stochastic. Many devices are made using material with randomly distributed QDs and then tested for strong coupling. Significant improvements in beam writing, plasma etching of GaAs based ma-

terial systems using just resist (no hard mask), and device quality have been made to increase the odds of getting a strongly coupled device again. An initial attempt to carry out ammonium sulfide based passivation was carried out in order to alleviate optical loss due to surface absorption. These experiments are ongoing.

Finally, in the spirit of synergy between projects such as the QD and sub-wavelength laser project, a new direction is being explored: optomechanical tuning of active micro- and nanoscale optical cavities. In almost every aspect of this thesis work an easy-to-use broadband wavelength tuning functionality would be hugely beneficial. In fact, a majority of time, effort, and precious active material in each and every one of the above projects is spent on the fabrication of high-quality microcavities that are spectrally aligned to a resonance of interest. The need for tuning is not only limited to devices but also to their testing. The work horse method of characterizing optical cavities in our lab is to couple a tunable laser, with tuning range of $\sim$ 100nm, to the cavity under study and measure the transmission spectrum. These external cavity diode lasers are physically large and depend on very precise mechanical motion and alignment. With this in mind, we would like to combine work concurrently being carried our in our group on optomechanical devices to create optomechanically tuned active devices. Initial ideas and fabrication are presented. This project has benefited from fruitful discussion with R. Camacho.

1.1 Thesis Organization

The organization of this thesis follows the progression outlined above. Work on QC lasers and sensing based on QC lasers is collected in chapter 2. The chapter is divided into design, fabrication, and testing of lasers, microfluidic integration, and an experimental sensing sections. Design of hybrid mode lasers including optical and thermal simulations is found in chapter 3. Fabrication procedures for sub-wavelength and hybrid mode lasers are explored in chapter 4. In chapter 5 hybridization and lasing are shown experientially, accompanied by further analysis. Chapter 6 presents work toward strongly coupled QD samples. Future work on tunable active cavities using optomechanics is presented in chapter 7. Final thoughts and conclusions are provided in chapter 8.

Chapter 2

Intracavity Mid-infrared Chemical Sensing with QC Lasers

2.1 Introduction

The mid-infrared region of the spectrum, also known as the fingerprint region, is rich in vibrational and rotational resonances of biological molecules [1]. Proteins, carbohydrates, and nucleic acids can be both identified and their structure probed by infrared absorption spectroscopy as can be seen in figure 2.1. The ability to detect and measure molecular structure, as well as structural changes, can lead to powerful scientific and medical tools. A notable example is Alzheimer's disease. The disease is associated with the presence of Amyloid plaque deposits on brain neurons. Amyloid plaque consists of aggregates of misfolded β-amyloid protein. The Amide I absorption band (C=O vibrational mode) can be probed by infrared absorption spectroscopy and can indicate secondary protein structure [2].

One of the largest hurdles in infrared spectroscopy is that the subject of study is usually found in an environment that is full of absorbing material. Water, for example, is absorbing across the infrared spectrum. Today, if one wants to use a standard Fourier Transform Infrared Spectrometer (FTIR) the sample must be manipulated into a pellet form, dried on a card, placed in between thin salt based plates, or even a fluidic cell. One can right away see the difficulty of studying something like a protein even in vitro. Such difficulties lead to very taxing requirements on intense low noise infrared light sources and high resolution spectrometers. This combination leads to expensive, very large experiments. For example, the Alzheimer's spectroscopy experiment in reference [2] was done using a synchrotron based infrared light source which is 170 meters is diameter and an FTIR which is on the order of ~ 0.75m by 0.75m in size.

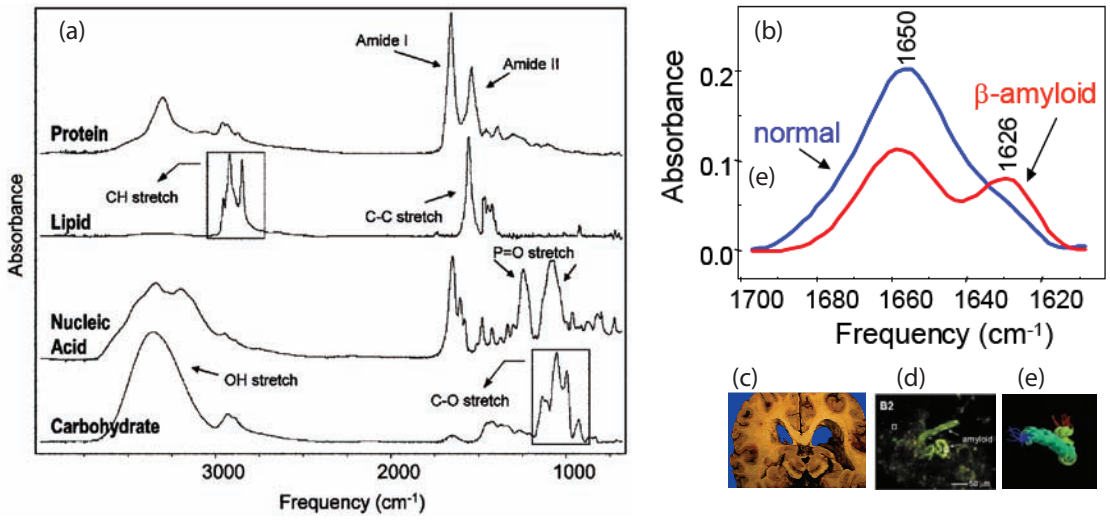

Figure 2.1: (a) Characteristic absorption spectra of several complex biological molecules [1]. (b) Synchrotron based infrared microspectroscopy is used to detect a conformational change of protein secondary structure from α-helix to β-sheet between healthy and diseased tissue in Amyloid plaque buildup in human brain tissue [2]. (c) Image of brain with Amyloid plaque buildup. [1](d) Fluorescence imaging of protein distribution in a tissue sample. (e) X-ray crystallography structure of β-amyloid peptide (1-42) [3].

We approach this work with the goal of using a class of on-chip infrared micro lasers to miniaturize infrared spectroscopy to allow for on-chip characterization of molecular structure with a specific focus on fluidic analytes. One can then bring to bear techniques from both the semiconductor field and micro fluidic field such as scalability, high density integration, and significantly reduced cost to develop a cheap, portable, spectroscopic infrared sensor. Our approach to developing a chip based spectroscopy system in QC lasers in broken down into four thrusts. In section 2.2 the design of surface sensitive ridge waveguide laser cavities and microdisk laser cavities will be discussed. Advances in fabrication techniques and testing of QC microcavities, including photonic crystal, ridge, and disk, are presented in section 2.3. Advances in integration of microfluidic polymer devices, as well as design challenges associated with polymer microfluidics, are discussed in section 2.4. Finally, a proof-of-concept sensing experiment is carried out using ridge air-guided lasers and typical laboratory solvents and presented in section 2.5.

2.2 Microcavity Design

2.2.1 Introduction to Quantum Cascade Lasers and Sensing

Since their first demonstration in 1994 [14], Quantum Cascade lasers (QCLs) have matured into one of the leading laser technologies in the mid-infrared for chemical sensing [9]. Through continued developments in material growth, electronic design, thermal packaging, and optical design, QCLs have now been demonstrated which operate continuous wave at room temperature [15], greatly simplifying their integration and use in spectroscopic applications. With the improving performance of QCLs has also come a diversification of their wavelength coverage, with laser operation demonstrated at wavelengths as short as 2.95μm [16] and as long as 187.5 μm [17].

In addition to these technological advancements, research into novel laser cavity geometries and applications of QCLs has also continued at a steady pace [18, 10, 19, 20, 21, 22]. Owing to their longer operating wavelength and unipolar electrical injection characteristic, QCLs represent a unique semiconductor laser source which is highly forgiving in terms of semiconductor processing. Unipolar injection eliminates steady-state surface recombination currents that hinder conventional diode injection lasers [23, 24, 25], allowing for complicated etched cavity structures such as photonic crystals to be implemented with QCLs [10, 20, 26]. The longer operating wavelength typical of QCLs also allows for the incorporation of metal layers into the cavity design as optical losses scale roughly as the inverse of the wavelength. This fact has been used advantageously in a variety of surface-plasmon lasers in the mid-infrared and THz frequencies [27, 28, 29, 30].

From their inception, QC lasers have become the leading monochromatic light source for chemical sensing as their wavelength bandwidth envelops the fingerprint region. Paralleling the rapid development of QC laser technology is a substantial body of work in the field of mid-infrared chemical sensing [31, 32]. Initial breakthroughs were made in the detection of trace gases [31, 32] and more recently of analytes in liquid form [33, 34, 35, 36, 37, 38]. While spectroscopic techniques have diversified, becoming more compact and increasingly sensitive, almost all QC sensor systems share a similar architecture: a stand-alone tunable QC laser, followed by an interaction region, and an infrared detector. The first chemical sensors employed a tunable laser and a macroscopic multipass optical cell. Nitrous oxide and methane gases diluted in nitrogen were introduced into the cell and absorption spectra were collected using a stand-alone mercury cadmium telluride detector (MCT) over the tuning range of the laser of approximately 2cm^{-1} [39]. Both continuous wave and pulsed lasers have been successfully employed, and in many cases with wavelength tuning achieved purely

by temperature control through current-injection schemes. Such techniques have been enhanced by using high-quality factor (Q) cavities as interaction regions [31]. High-Q cavities are also used for ring down spectroscopy. A tunable CW QC laser is used to pump the high-Q cavity interaction region. The laser is then interrupted and the decay time of the cavity is measured to generate absorption spectra.

The application of QC sensing to fluid phase analytes brought on a more significant change in the interaction region design. Analytes and solvent absorption cross sections in the fluid phase are significantly larger than in the gaseous phase and only very thin pass-through flow cells made of CaF_2 and BrF_2 with a path length on the order of 25 to 100μm can be used [33, 35]. Taking cue from attenuated total reflection (ATR) spectroscopy techniques, several interaction regions have been designed where sensing occurs in the nearfield. Some use a traditional diamond waveguide [34] and others use exposed silver halide optical fibers [37, 36]. Trace gas detection sensitivities are quoted in parts per billion [31]. In the liquid phase sensitivities are lower but the diversity of analytes is steadily growing. The absorption resonances in the liquid phase are often broader than in gas spectroscopy and are superimposed on the background absorption of the solvent. Therefore in liquid sensing schemes multiple lasers and wavelengths are sometimes used to probe multiple absorption peaks of the analyte. More recently there have been efforts to introduce analytes directly to the laser. In one case a permanent index of refraction of chalcogenide glass was photoinduced directly on top of a distributed feedback (DFB) ridge laser [40]. In another, fluid was delivered to an air guided DFB ridge laser using a polymer microfluidic interface [41].

In this section we develop a new sensor design akin to the efforts by [40] and [41] where the analyte is introduced directly into the semiconductor laser cavity, not an external cavity, i.e., intra (semiconductor) cavity sensing. The QC laser and interaction regions are no longer separate components but are integrated into one high-Q cavity. The direct interaction of analytes with the laser field leads to new sensing mechanisms. Intracavity sensing may be able to overcome some disadvantages of cavity assisted sensing. Spectral thermal tuning of QC lasers through temperature tuning is typically on the order of a few cm^{-1} and at maximum a few 10s of cm^{-1}. In our proposed intracavity sensing design we will use the full width of the gain bandwidth which is on the order of $100cm^{-1}$. Most importantly, the integration of laser source, interaction region, and possibly detector holds great potential for miniaturization and portability of future QC sensors.

We analyze the properties of air guided and surface-plasmon guided QCL structures with the goal of maximizing the fraction of the laser mode energy that extends into the external cladding

environment while minimizing loss. Such lasers allow for the internal laser field to interact with external materials or objects, and can be used in a variety of applications from near-field sensing of chemical and biological macromolecules, to nonlinear light generation in deposited nonlinear glasses or nonlinear fluids. We begin in section 2.2.2 with the analysis of different ridge waveguides formed from a laser epitaxial structure originally intended to be operated utilizing surface-plasmon vertical confinement, and with the active region of the laser lying directly at the top semiconductor surface (i.e., no top semiconductor cladding). Through fully vectorial finite-element method (FEM) simulations, we compare the different loss, active region confinement, and field penetration into the surface cladding of air guided and surface-plasmon guided modes of such a structure. In section 2.2.3 we utilize the results of the ridge waveguide analysis to design single mode microdisk laser cavities with greatly enhanced sensitivity to their external cladding environment. Both fully-vectorial 3D FEM simulations with accurate modelling of radiation loss from the microdisks as well as 2D effective index simulations of microdisk structures with nonazimuthally symmetric metal contact features are performed. Finally, the application of such laser devices to integrated microfluidic sensing of chemical and biological macromolecules is discussed in section 2.4. Surface sensitivity and laser performance figures of merit are quantified and an optimally surface-sensitive structure is determined.

2.2.2 Ridge Waveguide Modes

The unique electrical (unipolar) and optical (transverse-magnetic (TM) dipole-moment) properties of QCLs have allowed for the implementation of a variety of unique laser cavity geometries. Of particular interest to this work has been the development of surface-plasmon guided [27] ridge lasers and more recently air-guided ridge lasers [42]. Surface-plasmon guided lasers require no top semiconductor cladding and have a mode intensity which peaks at the top semiconductor surface. Air-guided lasers, with the laser mode penetrating above the top semiconductor surface, offer the opportunity for probing or otherwise interacting with the internal laser field. As will be shown in subsequent sections as well as reference [42], it is possible due to the high vertical resistance and small lateral resistance of high-quality QCL active regions to marry these two design concepts and simultaneously enhance surface sensitivity and laser performance. Below we analyze such laser structures, explaining both the reasons for improved laser performance and quantifying the attainable surface-sensitivity.

The epitaxially grown laser structure that we consider here is shown in Table 2.1. It is a nomi-

Table 2.1: Surface plasmon quantum cascade semiconductor structure [6]

Material	Doping (cm^{-3})	Thickness (nm)	Refractive Index
GaInAs	1×10^{20} [n^{++}]	10	$1.7 - i11$
GaInAs	1×10^{17} [n]	40	$3.47 - i5.48 \times 10^{-4}$
Active region	-	2.635×10^{3}	$3.38 - i1.97 \times 10^{-4}$
($In_{0.53}Ga_{0.47}As/Al_{0.48}In_{0.52}As$)			
GaInAs	5.0×10^{16} [n]	500	$3.48 - i2.73 \times 10^{-4}$
InP	1×10^{17} [n]	2×10^{3}	$3.07 - i3.3 \times 10^{-4}$
InP substrate	5×10^{18} [n]	2.5×10^{5}	$2.36 - i2.1 \times 10^{-2}$

nally surface-plasmon designed device with 50 QC stages grown just 50 nm below the top surface. It is capped with two semiconductor contact layers: a 40 nm lightly n-doped InGaAs layer followed by a 10 nm highly doped n^{++} InGaAs layer.

The vertical modes of several QC SP guided and WG ridges are simulated using 2D finite element method (FEM). A plane transverse to the direction of propagation is modeled by assigning complex indices of refraction or the corresponding dielectric constant and conductivity to each layer of the semiconductor, dielectric, and metal contact. Small 4μm wide ridges are first simulated to more quickly explore the geometry parameter space. Several full-size 36μm ridges with nitride electrical isolation and side contacts are then simulated. Simulation results are tabulated in Table 2.2. A SP guided laser was first simulated by fully covering the QC ridge with a gold contact layer as seen in figure 2.2(b). The mode has a very high mode overlap factor $\Gamma_a = 92.5\%$ with the active region and a loss coefficient of $\alpha_i = 67.5$ cm^{-1}. For comparison, a WG mode is simulated in the same structure by removing the top metal contact leaving 0.5μm metal tabs on each side of the ridge as seen in figure 2.2(c), taking advantage of the top doped layers for current spreading. The WG mode shows a more modest but still high overlap factor $\Gamma_a = 71.5\%$ with the active region, but a higher modal loss $\alpha_i = 90.3$ cm^{-1}.

Experimentation with different current confinement structures, other microcavity geometries, and the very high vertical resistance in this high-quality material indicates that the highly doped top contact (n^{++}) layer is not necessary for current spreading. It in fact may lead to significant absorption loss due to its high doping level (1×10^{20} cm^{-3}). For comparison both the SP and the WG modes are simulated without the highly doped n^{++} layer. The SP mode maintains a high active region overlap with a modest decrease in loss to $\alpha_i = 53.6$ cm^{-1}. The WG mode also retains its

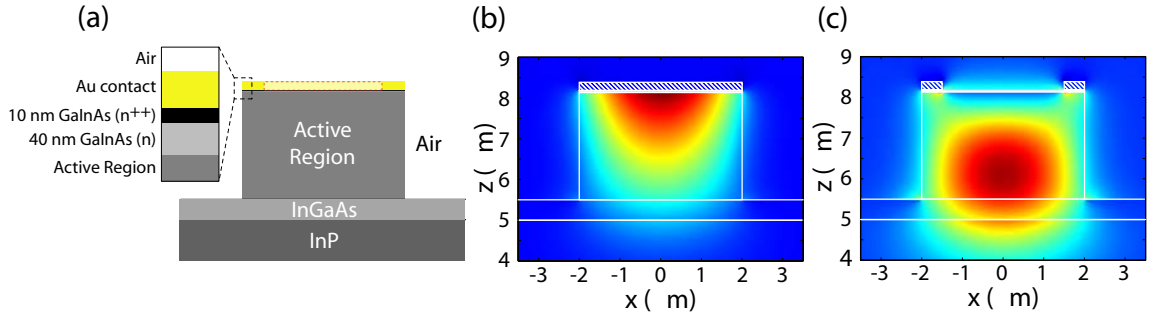

Figure 2.2: Mode plots (E_z) of the different types of ridge laser guided modes: (a) structure diagram (b) surface-plasmon mode when active material is fully covered with metal layer and (c) air-guided waveguide mode (metal region highlighted in red in (a) was removed). Metal contact is denoted by white hatch marks.

original active region overlap but a very significant reduction of loss $\alpha_i = 8.18$ cm^{-1} is observed. Not only does the WG mode have the lowest loss simulated thus far, it also has the greatest mode overlap factor with the external surrounding $\Gamma_e = 0.17\%$. To see if the overlap with the external surrounding can be increased for the SP configuration the metal contact is thinned to 10nm, less than the skin depth of gold. While the external overlap factor increases so its only a factor of 5 times smaller than the WG configuration, the loss increases to the highest value simulated thus far, $\alpha_i = 255.3$ cm^{-1}. The air confined WG design is clearly the best performing and most surface sensitive design.

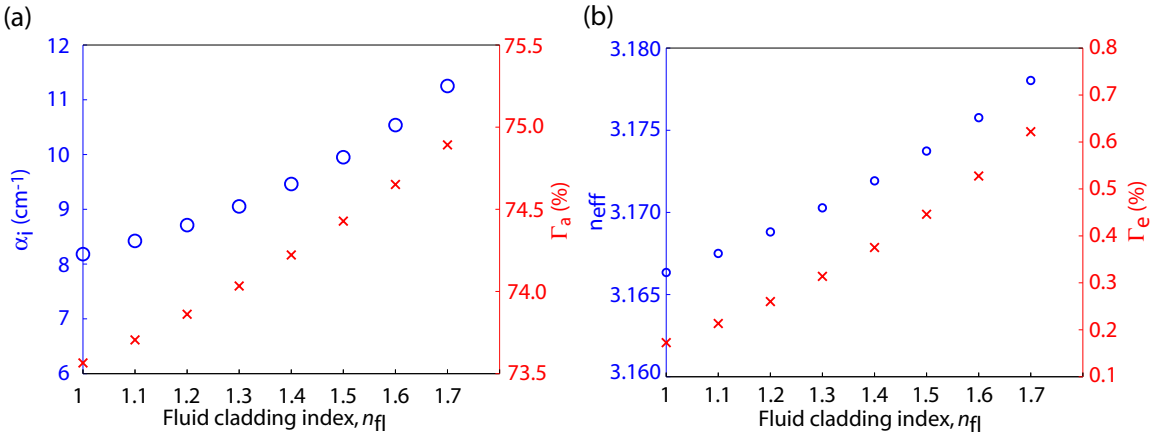

Figure 2.3: QC air confined ridge waveguide ($width = 4$ μm) surface sensitivity to fluid cladding refractive index for the fundamental TM mode at $\lambda = 7.7\mu$m. (a) Loss coefficient α_i and Γ_a versus surface index. (b) Effective index of mode and Γ_e versus surface index.

To evaluate the air-confined WG design (with the highly doped layer removed) for sensing, we

place absorption-free fluid on the top surface and vary its index within an experimentally achievable range of n =1.0-1.7. As a point of reference the index of water is $n = 1.28$ at $\lambda = 7.7$ μm[43]. The waveguide characteristics remain fairly constant with 1.3% increase in mode overlap with the active region and a mild increase in loss to $\alpha_i = 11.3$ cm^{-1} for $n = 1.7$ as shown in figure 2.3(a). What does increase dramatically is the mode overlap with the external sensing region right above the surface, increasing to $\Gamma_e = 0.62\%$ as shown in figure 2.3(b).

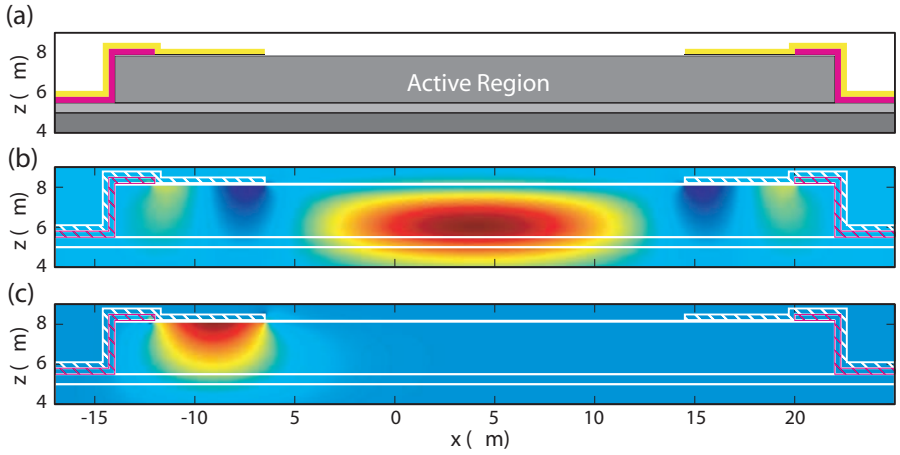

Figure 2.4: Mode plots (E_z) of an the different types of ridge waveguide guided modes: (a) structure diagram of 36μm wide, experimentally fabricated and tested, air confined ridge laser (b) air-guided waveguide mode and (c) one of two nearly degenerate surface-plasmon modes, the other (not shown) is found under the right contact pad. Metal contact and silicon nitride are denoted by white and violet hatch marks respectively.

An experimentally fabricated and tested device (described in section 2.3.3 as well as reference [42]) is also simulated. The laser ridge is 36 μm wide with a 21 μm contact free air guided region as seen in figure 2.4(a). Lossless silicon nitride (SiN_x) used for electrical isolation on the side of the laser ridge is included in the simulation (300nm thick), as well as the contact metal layer coming up the side of the ridge and contacting the edges of the ridge. The structure exhibits three different modes: a low loss centrally located waveguide mode shown in figure 2.4(b) and two nearly degenerate surface plasmon modes each under one of the contacts. The left SP mode is shown in figure 2.4(c). The waveguide mode has the lowest loss by a factor of 5 with $\alpha_i = 8.01$ cm^{-1}, the same as its thin ridge configuration counterpart. The surface mode overlap $\Gamma_e = 9.7\times10^{-2}\%$ is a bit lower than its thin ridge counterpart. Finally we simulate a wide ridge without any metal contacts, tabs, or SiN_x as effectively a 1D simulation to determine the material loss. The material loss of $\alpha_i = 4.23$ cm^{-1} will be used as a reference when developing new resonant cavity designs.

Table 2.2: Ridge waveguide mode summary

Top Laser Claddings	Mode	n_{eff}	α_i (cm^{-1})	$\Gamma_a(\%)$	$\Gamma_e(\%)$
| Au | n^{++} | n |$\cdots$	SP	$3.28 - i4.13 \times 10^{-3}$	67.5	92.5	5.3×10^{-4}
| air | n^{++} | n |$\cdots$	WG	$3.16 - i5.53 \times 10^{-3}$	90.3	71.5	2.0×10^{-1}
| Au | n |$\cdots$	SP	$3.27 - i3.28 \times 10^{-3}$	53.6	91.7	4.7×10^{-4}
| air | n |$\cdots$	WG	$3.17 - i5.01 \times 10^{-4}$	8.18	73.6	1.7×10^{-1}
| thin Au | n |$\cdots$	SP	$3.30 - i1.54 \times 10^{-2}$	251.3	95.5	3.5×10^{-2}
1D: | air | n |$\cdots$	WG	$3.25 - i2.59 \times 10^{-4}$	4.23	73.9	1.3×10^{-1}
Wide ridge: | air | n |$\cdots$	WG	$3.24 - i4.91 \times 10^{-4}$	8.01	75.3	9.7×10^{-2}
Wide ridge: | air | n |$\cdots$	SP	$3.34 - i3.20 \times 10^{-3}$	52.3	91.2	3.5×10^{-2}

2.2.3 Microdisk Cavity Modes

While we have shown air confined ridge waveguides to be low loss and very surface sensitive we explore the microdisk geometry for several reasons. Microdisks offer the opportunity of higher sensitivities and single mode compact and planar designs more amenable to sensor integration. The designs of such microdisks are first explored. The applications of these more compact and planar geometries will be further discussed in section 2.4.

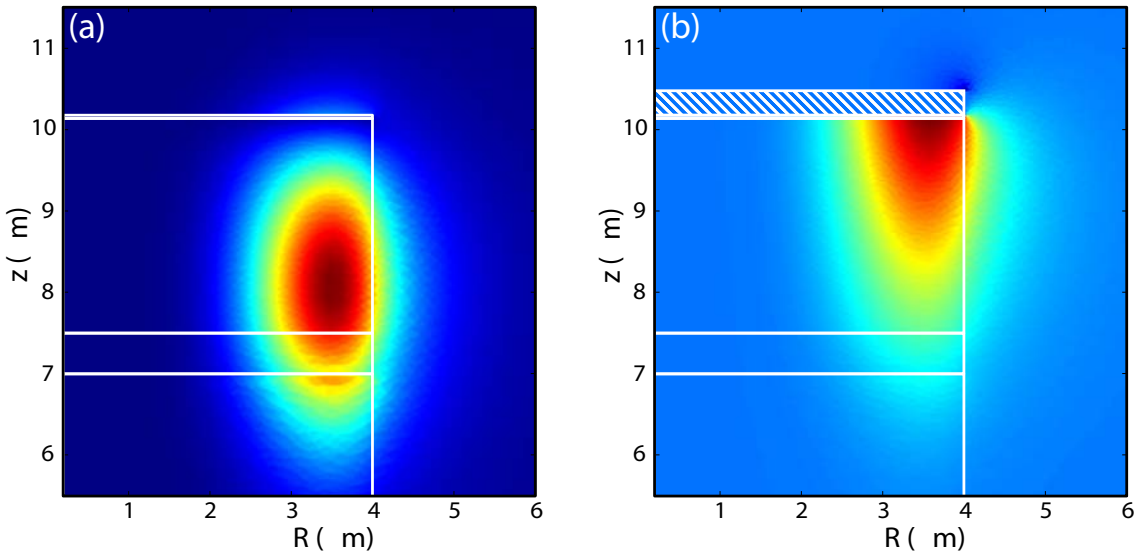

Figure 2.5: Mode plots (E_z) of the azimuthally symmetric 4μm microdisk FEM simulations: (a) air-guided waveguide surface sensitive low loss mode and (b) surface-plasmon guided mode. Metal contact is denoted by white hatch marks.

2.2.3.1 Azimuthally Symmetric FEM Simulations

Microdisk lasers are modeled using 3D, azimuthally symmetric, FEM simulations [44]. The purpose of this cavity design is to design a single mode surface sensitive laser. One way to reduce the number of modes in a resonator is to reduce its cavity length. We first simulate air-guided, contact-free, disks (figure 2.5(a)) of decreasing radii without material loss by setting all indices to be real and record their radiation Q-factor (Q_r) as shown in figure 2.6(a). Since the total cavity Q (Q_T) is related to the material Q (Q_m) through $1/Q_T = 1/Q_r + 1/Q_m$, we choose the smallest radius for which $Q_r > Q_m$ and therefore does not limit Q_T. We calculate Q_m from the 1D simulation in Sec. 2.2.2 through $Q_m \cong (\mathrm{Re}(n_{\mathrm{eff}}))/(2\mathrm{Im}(n_{\mathrm{eff}})) = 6280$. We therefore choose a radius of 4μm with a $Q_r = 9590$ which maintains an active region overlap $\Gamma_a = 72.4\%$ similar to the ridge waveguide configuration. The reduction of disk radius also leads to a great benefit in sensitivity. As shown in figure 2.6(a) the external mode overlap factor with the air surrounding the disk drastically increases with decrease in radius. At a large radius of 12.5 μm, the modal energy confined in the external air cladding is $\Gamma_e = 0.5\%$, about a factor of 3 larger than the thin ridge simulation. At the smaller radius of 4μm the external overlap rises to $\Gamma_e = 1.64\%$, about a factor of 10 better than the thin ridge configuration. From the field profile (E_z) in figure 2.5(a) it can be seen that the increased sensitivity is due the vertical disk sidewall as well as the top surface as in the case of ridge waveguides.

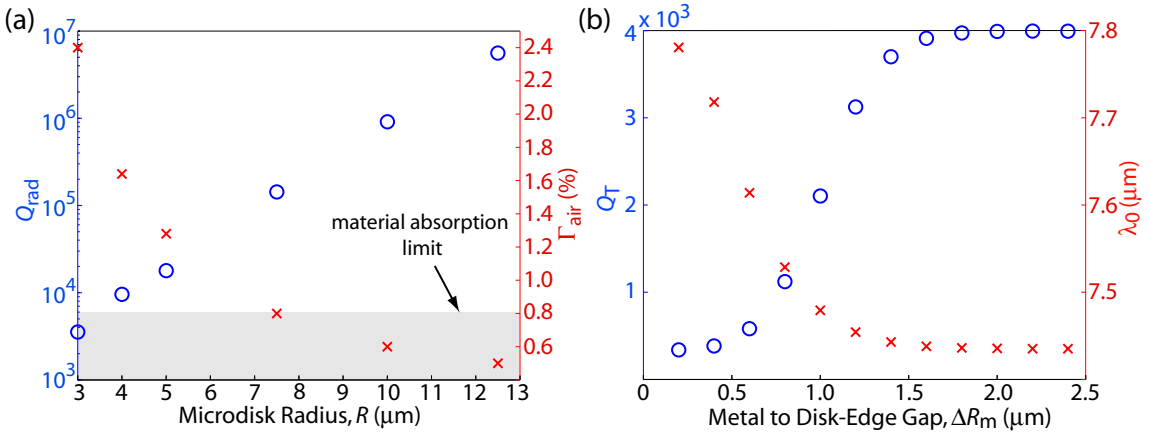

Figure 2.6: (a) Plot of the radiation limited Q-factor and wavelength of the fundamental TM WGM ($\mathrm{TM}_{p=1,v=1,m}$) versus radius (R) of the air-guided QC microdisk. (b) Plot of the Q-factor and wavelength of the fundamental TM WGM ($\mathrm{TM}_{p=1,v=1,m}$) versus the contact metal to disk-edge gap (ΔR) of the partially metal coated QC microdisk.

QC microdisk lasers are electrically pumped and a contact must be added whether or not it also

doubles as a surface plasmon guide. We simulate the 4μm disk fully covered with metal and then gradually pull the contact away from the edge towards the center creating a disk-edge to contact gap (ΔR_m). As in the ridge configuration when the metal is fully removed as seen in figure 2.5(a) there exists a low loss waveguide mode, and when the metal fully covers the disk as seen in figure 2.5(b) a more lossy surface plasmon mode exists. As seen in figure 2.6(b) a very clear transition from a low $Q = 340$ surface plasmon mode to a high $Q = 4000$ waveguide mode occurs when ΔR_m is increased, accompanied by a blue shift in the wavelength. Once the metal has retreated by $\Delta R_m \sim 1.5\mu$m from the edge, the mode becomes unaffected by any more recession of the metal. Since we want the largest contact possible to encourage current spreading we choose a safe recession of $\Delta R_m = 2.5\mu$m to further simulate.

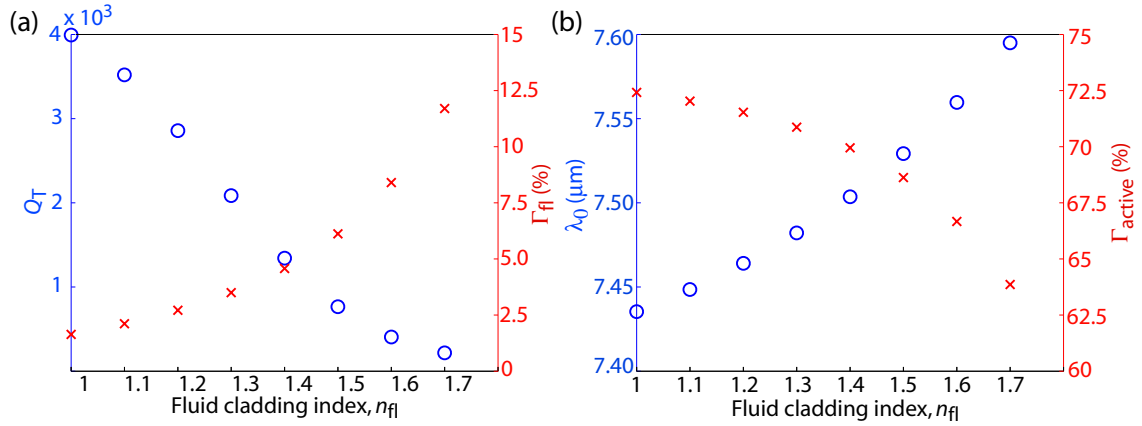

Figure 2.7: QC microdisk ($R = 4$ μm, $\Delta R_m = 2.5$ μm) sensitivity to fluid cladding refractive index for the fundamental TM WGM ($TM_{p=1,v=1,m=8}$). (a) Q and Γ_a versus cladding index. (b) λ_0 and Γ_e versus cladding index.

The air confined microdisk is an optimal laser design, and like its ridge counterpart is evaluated for its sensitivity to index variation of the surrounding. Absorption-free fluid with varying index from n=1.0 to n=1.7 is introduced above and on the side of the microdisk. The increased index to $n = 1.7$ yields a dramatic reduction of Q_T, falling from $Q_T = 4000$ to $Q_T = 340$, as well as a decrease in mode overlap with the active region to $\Gamma_a = 63.9\%$ as shown in figure 2.7. The mode overlap with the fluid is increased substantially to $\Gamma_e = 11.7\%$ and the wavelength tunes over $\Delta\lambda = 160$nm. A microdisk of this radius is extremely sensitive to an external index perturbation because it is too close to the radiation limit. A slightly larger microdisk with radius 7.5μm shows a more modest but still large increase in fluid overlap factor to $\Gamma_e = 3.56\%$ and wavelength tuning $\Delta\lambda = 71.4$nm with only a modest degradation of $Q_T = 4700$ for the same index perturbation as shown in figure 2.8.

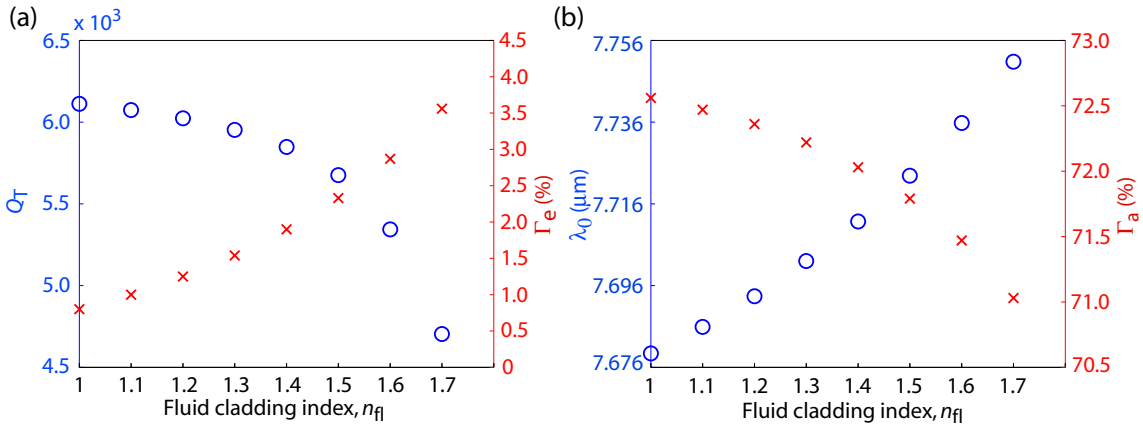

Figure 2.8: QC microdisk ($R = 7.5\ \mu$m, $\Delta R_m = 2.5\ \mu$m) sensitivity to fluid cladding refractive index for the fundamental TM WGM ($TM_{p=1,v=1,m=16}$). (a) Q and Γ_a versus cladding index. (b) λ_0 and Γ_e versus cladding index.

When integrating the microdisk into a sensor, the sensitivity to index variation can be tailored by modifying the radius. To create a sensitive fluid index sensor a small microdisk would be used. On the other hand, to create a sensor that is sensitive to the absorption of a fluid or its components, but is index insensitive, a larger disk would be used.

2.2.3.2 In-Plane FEM Simulations

The air confined disks are further simulated in the plane of the resonator with the goal of single mode operation. The effective indices of the vertically guided SP and WG modes from the thin ridge waveguide simulations are used in the metal and nonmetal covered regions of the disk structure. We choose the same 4μm radius disk to simulate.

The disks are first simulated with a central 3μm diameter metal contact corresponding to a $\Delta R_m = 2.5\mu$m as shown in figure 2.9(a)(b). The TM whispering gallery modes with $Q > 100$, and within $\sim 6.5 - 8.0\mu$m bandwidth are mapped, as shown in figure 2.10(a). The fundamental radial modes come in high $Q \sim 2500$ degenerate pairs of traveling waves, with a very wide mode spacing $\Delta\lambda > 0.68\mu$m. Several 2nd order radial modes also exist within this bandwidth but are of lower $Q < 1000$. Mode mapping using 3D azimuthally symmetric simulations as in Sec. 2.2.3.1 showed no other high-Q higher order vertical modes, allowing the 2D in plane simulations to capture all the modes of the disk.

The disks are then simulated with an experimentally viable contact scheme of four .5μm wide "spoke"-like contacts connecting the outside contact pad to the 3μm disk contact as shown in figure

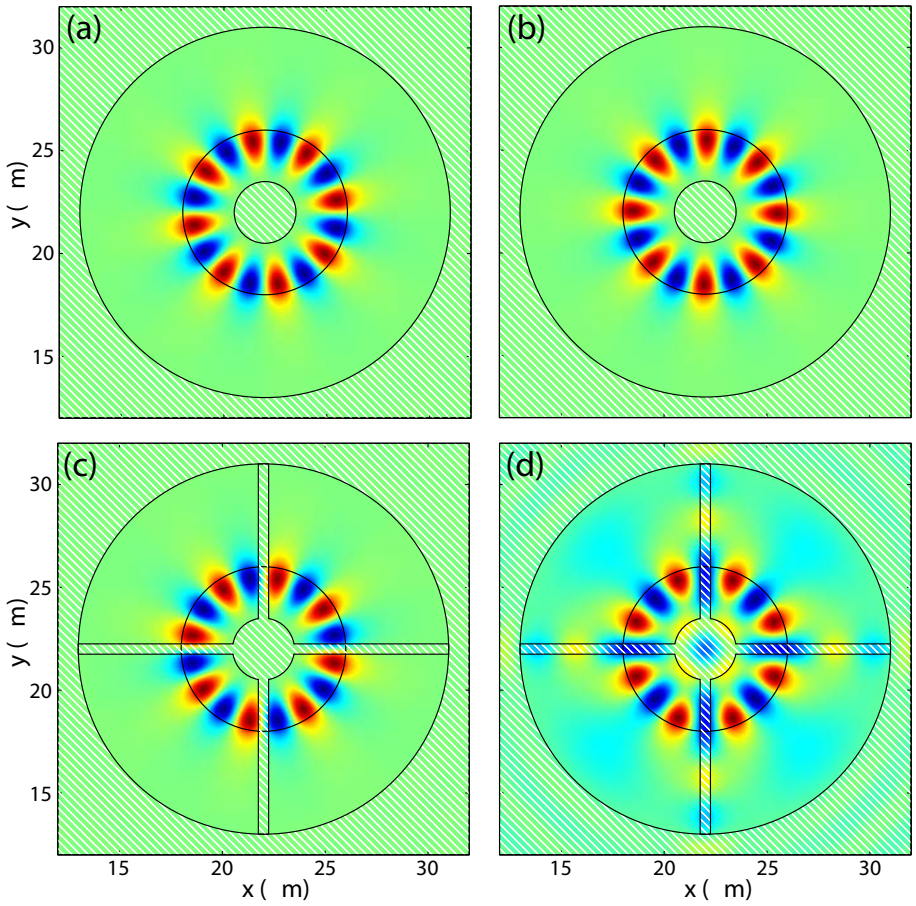

Figure 2.9: In-plane (2D) FEM simulations of an $R = 4\mu$m QC air-guided microdisk without and with four "spoke"-like electrical contacts connecting the outside contact pad to the inner contact region of the disk. Plot shows the E_z field component of the two degenerate $m = \pm 8, p = 1$ modes (a)(b) without contacts, and then the split modes with contacts(c)(d). Top metal contact regions are denoted by white hatch marks.

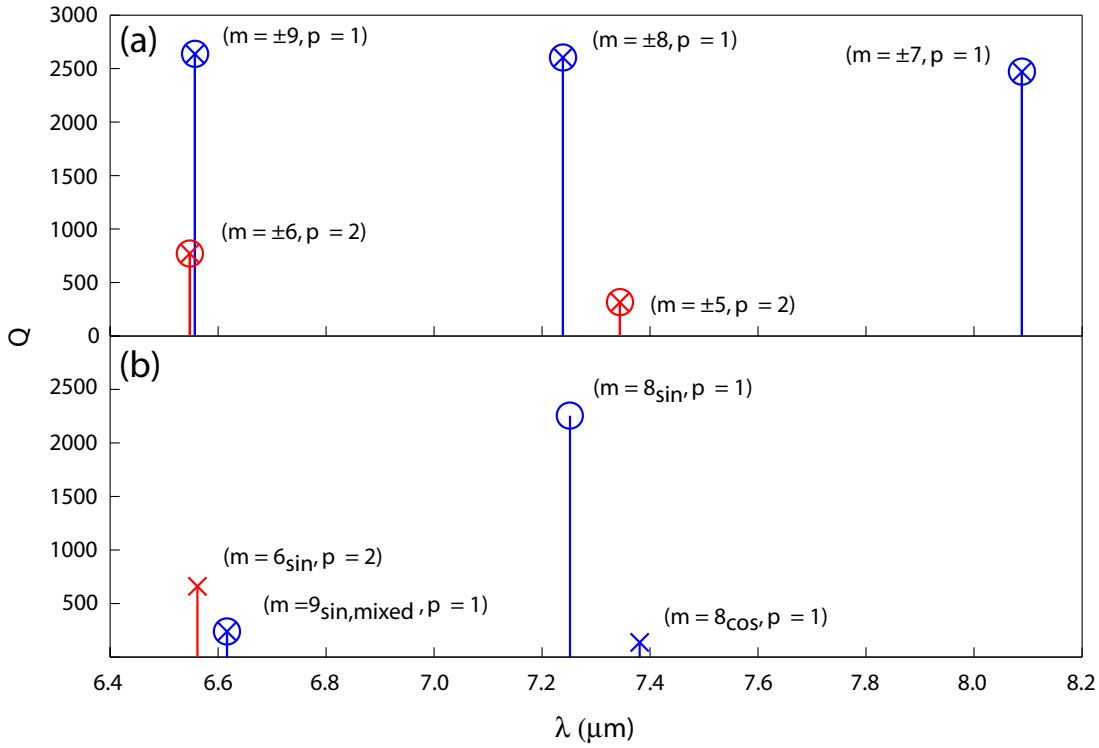

Figure 2.10: Map of a QC air-guided microdisk whispering gallery modes with $Q > 100$ with (a) and without (b) four 0.5μm "spoke"-like electrical contacts connecting the outside contact pad to the inner contact region of the disk.

2.9(c)(d). The modes within an identical bandwidth range are mapped. Modes that do not share the azimuthal parity of the contact scheme are suppressed as the fields can not avoid the lossy contact pattern and possibly couple to radiation modes. Modes that do match the azimuthal parity of the contacts, such as the $m = \pm 8$, $p = 1$ modes are split. One member of the pair (figure 2.9(d)) aligns with the contacts and degrades to a $Q \sim 140$. The other (figure 2.9(c)) avoids the contacts and maintains a high $Q \sim 2300$. It is now clear that adding planar contacts is beneficial in suppressing multi-mode behavior and only slightly degrades the Q of the mode located centrally within the gain bandwidth. We therefore achieve a planar, highly sensitive, lithographically tunable, single mode laser design.

2.2.3.3 Quantitative Laser Design Comparison for Sensing

Laser designs developed thus far are now evaluated as candidates for integrated fluid sensing systems in the mid-infrared. Design independent figures of merit (FOM) are defined to allow for quantitative comparison of different designs here and elsewhere.

To evaluate and compare the performance of QC laser sensor designs two figures of merit can be defined, one for laser performance and one for sensitivity. From second-order perturbation theory on Maxwell's equations we can separate the effect of an analyte with a complex index, i.e., lossy, on the complex frequency of the laser. A detailed derivation is shown in Appendix A.

$$\frac{\Delta\omega_r}{\omega_0} \cong -\frac{\Delta\lambda}{\lambda_0} \cong -\left[\frac{\Delta n_r}{n_0} - \frac{\Delta n_i^2}{2n_0^2}\right]\Gamma_e \tag{2.1}$$

$$\frac{\Delta\omega_i}{\omega_0} \equiv \frac{1}{2Q_e} \cong \left[\left(\frac{\Delta n_i}{n_0}\right)\left(1+\frac{\Delta n_r}{n_0}\right)\right]\Gamma_e \tag{2.2}$$

The real frequency shift ($\Delta\omega_r$) due to the introduction of an analyte in the near field of the laser is directly proportional to the perturbation of the real part (Δn_r) of the index to first order, and the shift of the imaginary component ($\Delta\omega_i$) is proportional to the perturbation of the imaginary part of the index (Δn_i) to first order. In both cases the effect of the perturbation is scaled by the energy overlap factor with the external (sensing) region Γ_e. Loss incurred in the laser will naturally manifest itself in an increased threshold current density. A spectrally non uniform loss can shift the laser frequency as well, as the threshold condition can be most easily achieved when the loss is minimum within the laser material bandwidth. This will be the subject of future experimental work. The lasing

Table 2.3: Summary of figures of merit across material type (WG: Waveguide, SP: SP guide) and mode type (AG: Air Guided, WG: wave guide, SP: SP guide)

Structure	Material	Mode type	$\bar{\Pi}$	$\bar{\Lambda}_e$
ridge, 36μm wide - 1D	SP	AG	4630	8.15
ridge, 36μm wide - 1D	SP	SP	473	1.16×10^{-14}
ridge, 36μm wide + 0.4μm doped layer -1D	WG	AG	293	0.278
ridge, 36μm wide - 1D	WG	AG	485	1.05
ridge, 4μm wide	SP	SP	456	2.34×10^{-3}
ridge, 4μm wide + contacts	SP	AG	2330	5.38
disk, 4μm radius + center contact	SP	AG	2890	65.5
disk, 7.5μm radius + center contact	SP	AG	4430	48.9
disk, 7.5μm radius + center contact + fluid n=1.4	SP	AG	4210	111

threshold condition, gain equals loss, is used to related the loss introduced by the analyte $\Delta n_i/n_0$ to the threshold current density of the laser,

$$J_{th} \cong \frac{\omega}{\langle g'_m\rangle_t \Gamma_a Q_i}\left(1+\Gamma_e Q_i \frac{2\Delta n_i}{n_0}\right), \tag{2.3}$$

where $\langle g'_m\rangle_t$ is the differential gain per unit time. From the threshold current we can define two figures of merit. The first for the overall performance of the laser,

$$\bar{\Pi} = \Gamma_a Q_i = \left(\frac{2\pi n_g}{\lambda_0}\right)\frac{\Gamma_a}{\alpha_i}, \tag{2.4}$$

and the second for sensitivity to an analyte in the external field,

$$\bar{\Lambda}_e = \Gamma_e Q_i = \left(\frac{2\pi n_g}{\lambda_0}\right)\frac{\Gamma_e}{\alpha_i}, \tag{2.5}$$

where n_g is the group index of mode. It now becomes clear that an optimized laser design would maximize the mode overlap with the gain material Γ_a as well as maximize (minimize) Q_i (α_i). An optimized sensing design would increase the energy overlap with the external region Γ_e and maximize (minimize) Q_i (α_i). Figures of merit are summarized for representative simulations in Table 2.3.

Using the tabulated figures of merit in Table 2.3 we can now compare different laser cavity designs across guiding material types and geometries. Along with simulations of material designed

for SP configuration we also simulated an air guided ridge with material epitaxy from an air confined DFB [45] and used in a fluidically tuned device [41].

When comparing the wide 36μm ridges it becomes clear that the surface plasmon material, air confined laser, is the leading candidate as a sensing laser as it has the highest figures of merit ($\bar{\Pi} = 4630$, $\bar{\Lambda}_e$ =8.15). It would have the lowest threshold current and the highest sensitivity to absorption of an analyte. The benefit of the air confined WG mode over the SP mode in SP material is evident in thin ridges as well despite the addition of small metal contacts along the edge of the ridge. Microdisks having many advantages in system integration are shown to perform just as well as the best waveguide and are more than 5 times more sensitive ($\bar{\Pi} = 4430$, $\bar{\Lambda}_e = 48.9$). By varying the radius of the disk one can choose a better performing disk versus a more sensitive disk.

To elucidate the relationship between the absorption coefficient of an analyte and the threshold current density we define a modified sensitivity figure of merit,

$$\Lambda_e = \left(\frac{\lambda_0/n_0}{2\pi}\right)\bar{\Lambda}_e, \tag{2.6}$$

where the fractional change in threshold current density is equal to

$$\frac{\Delta J_{th}}{J_{th,0}} = \alpha_e \Lambda_e. \tag{2.7}$$

Typical laboratory aqueous environments and laboratory solvents have a refractive index of $n \sim 1.4$. As an example isopropyl alcohol has an index n= 1.38 [8] and an absorption coefficient $\alpha_e \sim 880\text{cm}^{-1}$ at 7.7μm as measured by FTIR absorption spectroscopy. From figure 2.8 we choose a microdisk of radius $R = 7.5\mu$m that maintains high performance and increased sensitivity when placed in a $n = 1.4$ environment ($\bar{\Pi} = 4210$, $\bar{\Lambda}_e = 111$, $\Lambda_e = 9.86 \times 10^3$). Given that a $\Delta J_{th}/J_{th,0} = 1\%$ can be detected, the disk is sensitive to a loss of $\alpha_e = 1.01\text{cm}^{-1}$. This corresponds to a sensitivity of 1 part in 870 or approximately 0.1% concentration when diluted in fluid with similar index and little absorption such as methanol.

The design of highly sensitive QC lasers for intra-cavity sensing of biological and chemical molecules has been investigated through fully vectorial finite element simulations. Using perturbation theory, figures of merit were developed to quantitatively compare sensing laser designs. Air-confined ridge lasers and air-confined microdisks were judged to be excellent candidates for sensing, minimizing overall loss while maximizing the overlap factor with the sensing region. The air-confined microdisk geometry allows for the creation of densely packed, single mode, vertically

emitting lasers. Such lasers readily lend themselves to immediate microfluidic integration. Allowing for all the advantages that come with large scale microfluidic integration: multiplexing, low volume sensing, and environmental control. While the sensitivity of these laser sensors are not on par with gas sensing QC laser sensors, the portability and integrability will make them extremely useful. On-going work focuses on the experimental implementation of ridge and microdisk air-confined lasers and their integration with fluidic delivery chips.

2.3 Device Development: Fabrication and Testing

2.3.1 Approach

The design and fabrication of photonic crystal quantum cascade lasers began as a collaboration between K. Srinivasan and Professor O. Painter at Caltech and a group at Bell Labs headed by Dr. F. Capasso. Work was carried out on both optical design [46, 47] and fabrication [48], culminating in pulsed operation lasing at 18K [49, 10]. As QC lasers had already shown themselves as very useful mid-infrared sources for sensing, the natural progression of the work was towards chip based sensing.

The progression of QC laser development is as follows. Coupled with advances in QC material growth the hope was to fabricate room temperature PC lasers amenable to fluidic sensing. The process was modified for electron beam lithography at 15KeV and the use of silicon nitride hard masks. Details of fabrication and testing of QC-PC lasers are presented. Pre-processing, as discussed in this section was carried out by V. Moreau in Professor R. Colombelli's lab at the University of Paris-Sud. The need for creating current confining structure to improve operation, coupled with the expertise in the group in the design of microdisk cavities, led to the fabrication and testing of microdisk lasers. Briefly, the design and fabrication of microdisk lasers with a Bragg grating on the periphery for single mode operation was explored. Finally, as simulations have clearly shown that a low loss surface sensitive air-guided ridge waveguide cavity can be designed, a parallel fabrication of such lasers were carried out by V. Moreau and Professor R. Colombelli at the University of Paris-Sud. This section is divided into two main subsection: 2.3.2 PC lasers, microdisk lasers, and microgear cavities and 2.3.3 air-guided ridge waveguide lasers.

2.3.2 Photonic Crystal and Microdisk QC Lasers

2.3.2.1 Fabrication

The processing of QC-PC lasers in a combination effort by 3 groups: Sheffield, Paris-Sud, and Caltech. A processing flow is presented in figure 2.11. The processing begins with MOVPE growth of the QC structure shown in table 2.1. The Paris group then uses optical lithography and wet etching to form a current confining mesa. In later fabrication runs this step was skipped. A SiN_x insulator is deposited via plasma enhanced chemical vapor deposition (PECVD) and optical lithography, and reactive ion etching (RIE) is used to open up windows inside the current confinement mesa in the SiN_x. Next a thick Ti/Au contact covering the SiN_x and an outer permitter of the exposed QC mesa is deposited via optical lithography, electron beam evaporation, and liftoff. Finally a thin Ti/Au surface plasmon metal layer is deposited onto the QC mesa. In later fabrication runs only a one step contact deposition is carried out.

At this point the samples are shipped to Caltech and our processing begins. The nominal optical design is of a J-point triangular lattice with a defect: $a/\lambda = 0.308$, $r/a = 0.32$, and $r_{def}/a = 0.28$ [47]. At $\lambda = 7.5\mu$m the lattice spacing is $a = 2.4\mu$m and hole diameter $d = 1.5\mu$m. A thick 1.1μm layer of SiNx hard mask is deposited via PECVD (see conditions in table 2.4). Next a sensitive e-beam resist is spun on the sample. A very thick film of high sensitivity e-beam resist Zeon ZEP-520A is achieved using a 3-layer spin process. The first two spins consist of a spin at 3500RPM for 60sec, bake for 7min at 180C, followed by a 3min cool down. The third spin is the same speed but with a 15min bake time. To promote adhesion of resist to the SiNx the samples were dipped in Buffered HF Improved (Transene) for 5sec followed by deionized water rinse, IPA rinse, and N_2 blow dry. Electron beam lithography was carried on a modified Hitachi S-4300 scanning electron microscope (SEM) using custom "homemade" beam writing hardware and software [50]. Optimized writing was done with a dose $D = 39\mu$Ccm^{-2} and speed below 300kHz. Resist was developed in Zeon ZED-N50 for 2.5min and rinsed in Zeon ZMD-D for 30sec. An SEM cross-sectional micrograph of PC hole pattern resist is shown in figure 2.12(a). The resist is hardened with a 2hr bake at 100C. A subsequent pattern transfer into the SiNx was done via C_4F_8/SF_6 based inductively coupled reactive ion etching (ICP-RIE). Process parameters are shown in Table 2.5. SEM micrographs of SiNx etch are shown in figure 2.5(b)(c). The e-beam resist is then removed by sonicating (level 2, 10min) in Trichloroethylene (TCE). The pattern is then transferred into the QC material via Ar/Cl_2 based ICP-RIE etching through the metal layer. An SEM micrograph of

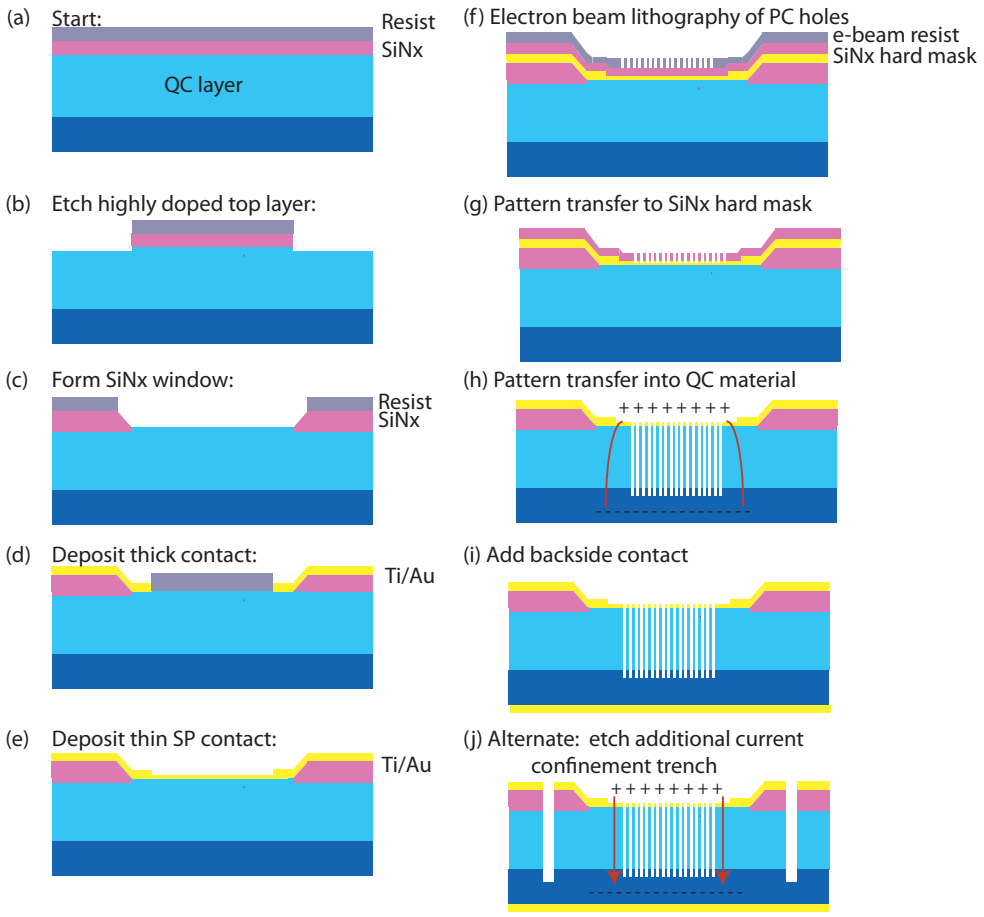

Figure 2.11: Fabrication flow for PC-QC laser cavities: (a) Start with QC epitaxy, deposit hard SiN_x mask and spin resist mask. (b) Lithographically pattern the resist and SiNx using RIE etching and etch the away the highly doped (current carrying) top layer. (c) PECVD deposit a SiNx insulator layer and open up window with RIE etching. (d) Deposit thick Ti/Au contact by resist liftoff technique. (e) Deposit thin SP Ti/Au contact layer. (f) Spin 3x layer of e-beam resist and pattern hexagonal lattice photonic crystal. (g) Transfer e-beam resist pattern into SiNx hard mask using ICP/RIE (C_4F_8/SF_6 chemistry). (h) Transfer pattern into QC material using ICP/RIE (Ar/Cl_2). (i) The sample backside is then mechanically polished and a Ti/Au backside contact is deposited. (j) An additional trench around the PC cavity is sometimes etched to increased current confinement.

Table 2.4: PECVD conditions for deposition of hard SiN_x mask

Parameter	Value
SiH_4/N_2	400sccm (396sccm)
NH_3	20sccm (19.8sccm)
N_2	600sccm (591sccm)
High Frequency	20W/13sec (20/1W)
Low Frequency	20W/7sec ($16/6-7$W)
P	650mTorr (650mT)
T	300C (300C)
t	93min

an extremely deep 5.25μm etch is shown in figure 2.5(d). A final SiNx etch with a reduced RF power is used to remove the remaining SiNx hard mask. One must be very careful with this etch as prolonged exposure of metal contact to plasma will damage the contact. Devices are then shipped back to France. The top side is protected with resist and the backside is mechanically polished down and a 10/100nm Ti/Au back contact is evaporated. A modification to the above process is the additional patterning of a current confining ring. Such patterning would occur in parallel to the definition of the PC patterns. A significant difference between the current process and the old process is the ability to etch straight through the top metal contact. In previous processing QC etching was done and then the top metal contact was evaporated. This placed a very stringent verticality requirement onto the PC holes, otherwise the side walls would gather metal, leading to electrical shorts and optical loss. figure 2.12 shows SEM micrographs of the etch process at various states. An exemplary extremely deep QC/InP etch can be seen. Furthermore figure 2.12 shows a comparison between previous fabrication that led to lasing in reference [10] and current fabrication is shown. It is important to note that the presence of the metal changes the thermal properties of the etch significantly, leading to different etch conditions.

2.3.2.2 Testing

The layout of the testing setup is shown in figure 2.13. QC laser devices are mounted to a copper block/Teflon assembly using indium paste. The copper block/Teflon assembly allows the backside to contact electrical ground and another copper piece, insulated by a Teflon spacer from ground, to be wire bonded to the bond pads on the top of the device. The assembly is then clipped onto the cold

Table 2.5: Summary of optimized ICP-RIE etch of SiNx hard mask and QC material. Numbers without parentheses are values asked for, numbers in parentheses are actual values.

SiNx Etch (ICP-RIE)		QC Etch (ICP-RIE)	
Parameter	Value	Parameter	Value
RF	4-6W (4-6/2W)	RF	375W (372/12W)
ICP	1000W (972/2W)	ICP	575W (561/2W)
D.C Bias	22-23V	D.C. Bias	$\sim$ 490V
(C_4F_8/SF_6	14.4/13.7sccm (14.4/11.5sccm)	Cl_2/Ar	8/13sccm (8/12.6sccm)
P_{ch}	15mTorr (14.6mT)	P_{ch}	3mTorr (2.8mTorr)
P_{He}	5Torr (0.7sccm)	P_{He}	-
T	20C (24C)	T	20C (29*C*)
t	$\sim$ 60min	t	6.5min

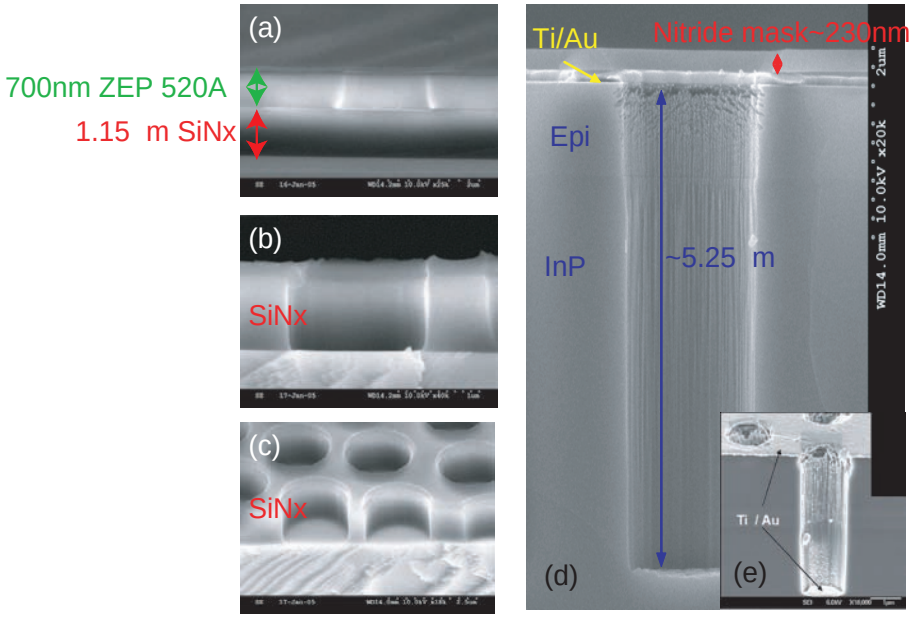

Figure 2.12: Forming of PC holes in already metal coated mesa: (a) Cross sectional SEM micrograph of double spun ZEP 520A electron beam resist pattern with a hexagonal PC pattern. (b) ICP/RIE etch (C_4F_8/SF_6 chemistry) transferring PC pattern into hard SiNx mask. (c) 30° angled SEM micrograph of etched SiNx mask. (d) ICP/RIE etch (Ar/Cl_2 chemistry) transferring PC pattern through QC layer into waveguide layer. Etch goes directly through Ti/Au contact. (e) Example of older generation etching: holes were first etched and then the contact pad deposited.

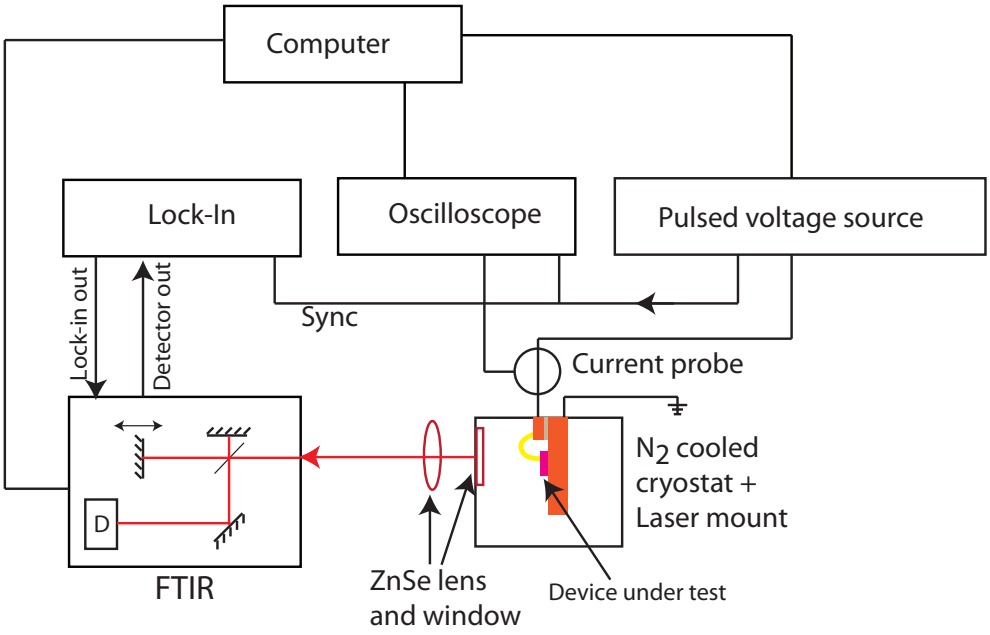

Figure 2.13: Schematic of QC laser test setup

finger of a liquid N_2 cooled cryostat. The devices are pumped using a pulsed voltage source and current is measured via an inductively coupled current probe, measured on a oscilloscope. Laser radiation and PL is directed through a Zinc Selenide (ZnSe) window in the cryostat, collimated with a ZnSe lens and directed into an open port of an FTIR. The laser radiation acts as the source of the FTIR. A synchronization signal from the pulse source is used to make lock-in measurements of laser spectra. Light voltage/current measurements are made on an independent MCT detector.

A set of two PC devices that lased is shown in figure 2.14(a). The PC pattern is placed within a 70μm SiN_x window. The laser is electrically pumped at 84kHz with $40-50$ns wide pulses. Lasing is achieved at $T = 78$K. Unfortunately not enough devices lased to allow for mode versus lattice constant mapping. Devices were extremely fragile and operating temperature could not be raised much. For non-lasing devices a common mode of failure was actual physical damage that could be imaged later. The most likely culprit is the quality of the contact metal deposition. The presence of pinholes or globs of metal eventually leads to shorting of the devices.

A comparison of the IV curves of PC structures with IV curves of ridge laser structures shows significant differences as can be seen in figure 2.15(a). Primarily, in the ridge configurations the IV curve shows a significant change in slope or resistance at alignment. It is important to note that the kink in the IV curve is not an indication of lasing, but just alignment of energy levels is the quantum

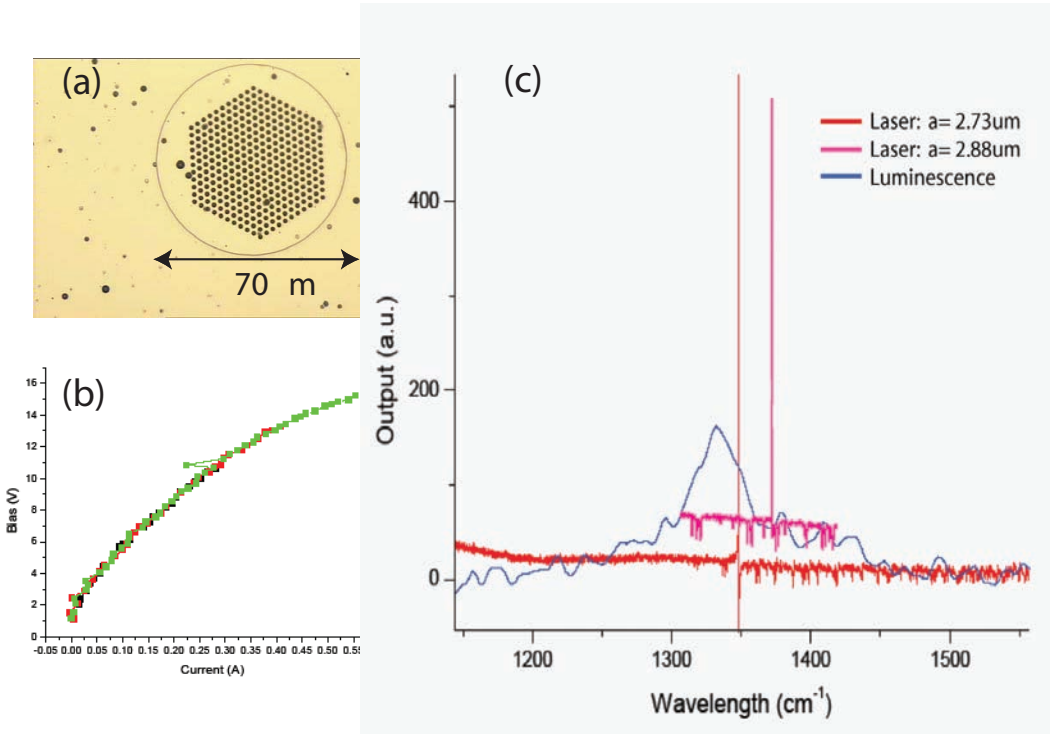

Figure 2.14: (a) Optical image of final QC PC lasers showing the SiNx window and photonic crystal pattern. (b) IV curves for device MR2230K-F11 and F13 with two different lattice constants a. Turn on behavior is very slow. (c) Spectra of the two lasing devices. PL spectra is shown for reference

cascade. The lack of such a kink in the case PC devices indicate a lack of current confinement in the laser structure region. We therefore etch a current confining ring around the SiN_x opening. The trench takes the form of a circle with one to several breaks to allow for continuity of the top metal contact. Such laser structures lase pulsed mode almost all the way up to $T = 280$K. Again not enough devices lased in order to conclusively determine whether lasing action occurs due to PC confinement modes or whispering gallery type modes in a microdisk inadvertently formed by the current confinement trench.

From simulations in section 2.2 we see that a microdisk cavity in itself could function as an excellent sensing laser. Simple microdisks were fabricated and tested as can be seen in figure 2.16. They lase multi mode, but with only 2-3 modes. A cursory attempt to make single mode microdisk lasers was undertaken by adding a Bragg grating to the periphery of the microdisk. SEM micrographs of such structures is shown in figure 2.17. The QC material etch quality is not very good and may be a reason for lack of lasing action.

Within this section many possibilities for both PC and microdisk sensing lasers have been dis-

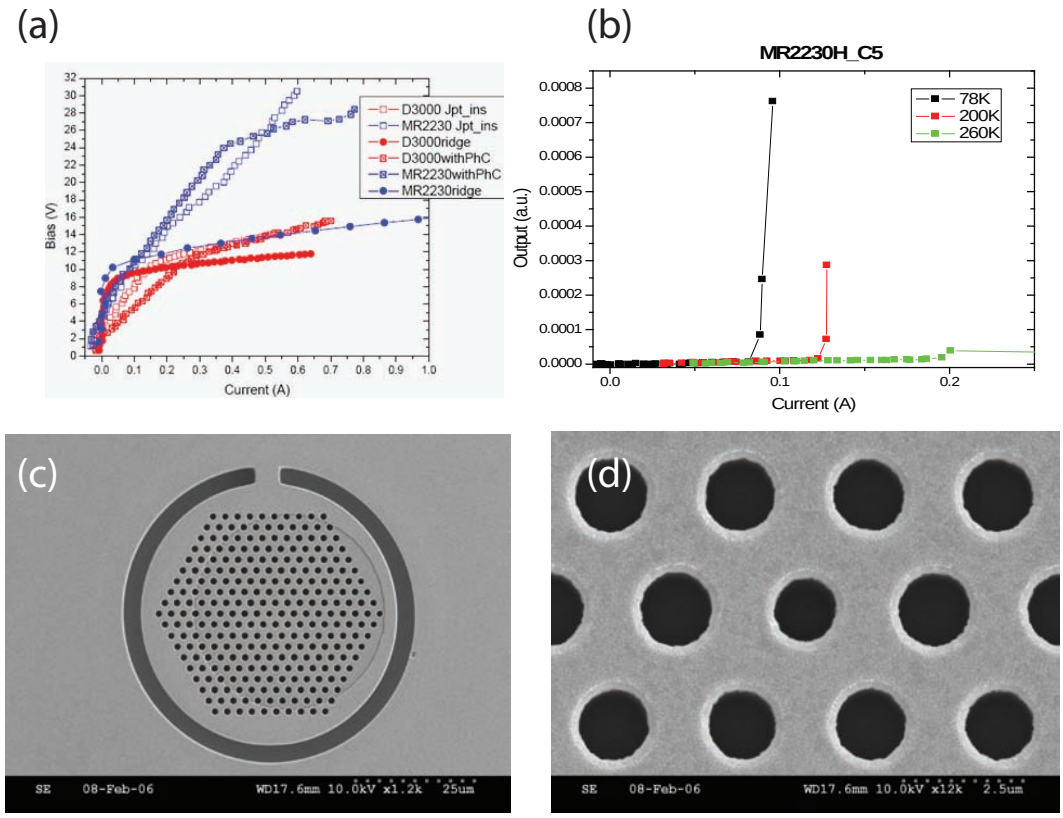

Figure 2.15: (a) Comparison of IV curves for ridge waveguide lasers and PC devices. (b) LI curves for PC devices surrounded by a current confining ring. (c) SEM micrograph of PC laser with current confining ring. (d) SEM micrograph zoom in of defect region of PC structure.

cussed. Further improvements either in material growth or fabrication techniques are needed to bring these devices to a level where they can experientially be used as sensing lasers. This endeavor is highly constricted by the scarcity of quantum cascade material available to our group at Caltech. Since the goal of the project is to use QC lasers for sensing we have opted to put further developments on hold and move to even simpler designs which will allow for proof-of-principle sensing experiments. The fabrication and design of such simpler ridge waveguide lasers are discussed in the next section.

2.3.3 Fabrication and Testing of Air-confined Ridge Waveguide Lasers

The fabrication and testing of QC air confined waveguide lasers was done at the University Paris-Sud by V. Moreau with the direction of Professor R. Colombelli (see reference [42]). Fabrication steps and testing are from the above reference. Air confined laser designs were developed at Caltech,

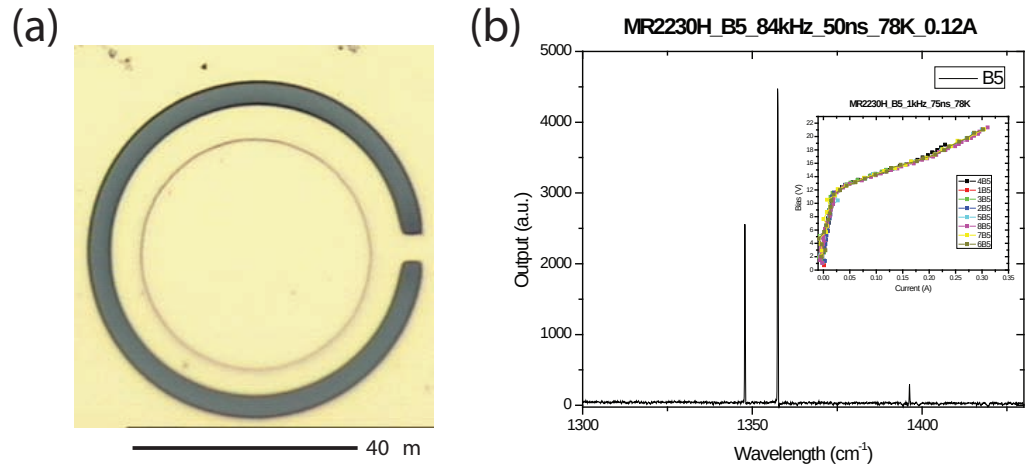

Figure 2.16: (a) Optical image of QC microdisk formed by current confinement trench. (b) Optical spectrum of lasing QC microdisk laser. Inset shows IV curve).

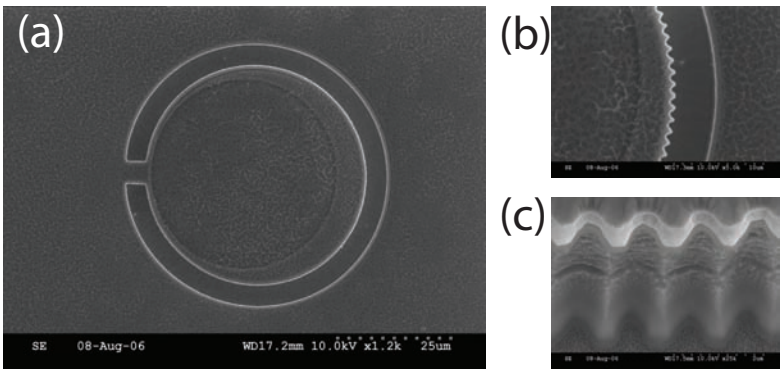

Figure 2.17: (a) SEM micrograph of microgear QC cavity. (b) Zoom in of microdisk periphery. (c) Zoom in of microdisk etch quality.

see section 2.2.

The laser heterostructure (sample MR2230) was grown by low pressure metal organic vapor phase epitaxy (MOVPE), using an $In_{0.5}3Ga_{0.47}As/Al_{0.48}In_{0.52}As$ lattice matched to a highly doped InP substrate. Further details of the growth process can be found in reference [6]. The active regions are based on a 2-phonon-resonance design (reference [51]), with the lasing transition designed for nominal emission at $\lambda = 7.5\mu$m. Fifty active-region/injector stages were grown, preceded by a 500nm thick InGaAs layer doped to $n = 5 \times 10^{16}$ cm^{-3} and followed by InGaAs contact facilitating layers. For this work, the laser structure has been processed in a Fabry-Perot ridge geometry with only narrow lateral contacts. An HBr-based wet chemical etch has been used to define the laser

resonators. A large portion of the device surface is left exposed, as shown in figure 2.18(c). The fabrication procedure is sketched in figures 2.18(a) and (b). Lasers with waveguide ridge widths of 26, 31, 36, and 41μm, and nominal air-gap opening widths of 16, 21, 26, and 31μm, were fabricated. The thin, highly doped top contact layer can be removed either by wet chemical etch, or by RIE. However, the top contact layer gets most probably removed during the surface cleaning of the sample with oxygen plasma followed by oxide removal using HCl/HF, making the final etch procedure described above often unnecessary. After mechanical polishing and back contact deposition (Ti/Au - 10/120nm), the samples are cleaved into laser bars, mounted with indium solder on copper blocks, wire bonded and loaded in a cryostat for device characterization.

Figure 2.18(d) shows the current-voltage (IV) characteristics of a typical device. Its sharp turnon is evidence that the current is efficiently injected, and that the contribution of the thin, top n+ layers to the lateral current spreading is not essential. In fact, the inherent lateral conductivity of the active region dominates the current spreading process, with measurements on test structures fabricated from the same wafer yielding an effective lateral current spreading extent of $20-25\mu$m [6]. We found that efficient current injection can be achieved (as determined by laser threshold) in laser ridges with widths as wide as 41μm (corresponding to an air gap of 31μm), provided that two lateral top contacts are used. If current is injected from one of the two top contacts only, the maximum device operating temperature drops (from RT to 250K). The light-current (LI) characteristics of a 36μm wide device is reported in figure 2.18(f). The device achieves lasing in pulsed-mode up to room temperature. The peak output power is $\sim$ 100mW at 78K, and $\sim$ 10mW at 300K. Finally, figure 2.18(e) reports typical laser emission spectra for different operating temperatures. At a temperature of 78K the emission is peaked at $\lambda = 7.3\mu$m, while at 300K the emission is detuned by 0.4μm, up to $\lambda = 7.7\mu$m. The devices exhibit clear Fabry-Perot fringes (figure 2.18(e)), which yield an effective index of refraction $n_{eff} = 3.41$ at $T = 78$K, and an $n_{eff} = 3.44$ at RT.

2.4 Microfluidic Integration

By mating QC lasers with a microfluidic delivery system one can envision a monolithically integrated sensor. In this section work towards such integration is presented. A sketch of such integration is shown in figure 2.19(a). Many potential biological and chemical analytes are found in multi-component mixtures. Absorption spectroscopy is plagued by the need to separate the spectral signatures of the analyte of interest or physically separate the analyte from the mixture. Our sen-

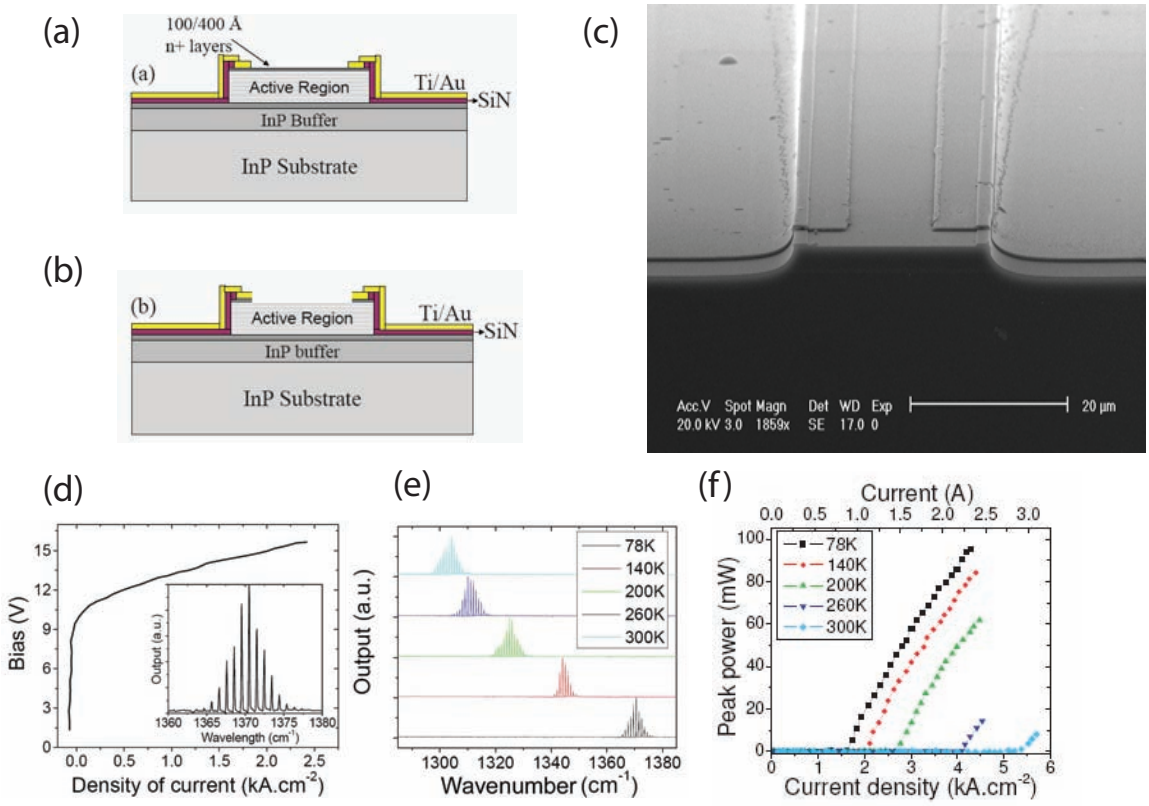

Figure 2.18: (a) Schematic layout of the fabricated devices. The contacts are deposited laterally on the edge of the ridge waveguide. Most of the ridge surface is left exposed to the air. The sidewalls in the real-devices are slanted, not vertical, since a wet chemical etch ($HBr:HNO_3:H_2O$) has been used. (b) A wet etch, or an aggressive oxygen plasma followed by a dip in HCl can remove the thin top n+ layer. (c) SEM image of a typical final device. (d) Current-voltage (IV) characteristics at a temperature of 78K for a typical device (100ns pulse width at 5kHz repetition rate). The device dimensions are 1500μm by 36μm. Inset: Fabry-Perot spectrum of a typical device at 78K. (e) Emission spectra at different temperatures for a typical device (50ns pulse width at 84 kHz repetition rate). The spectra were acquired with an FTIR operated in rapid-scan mode and with a resolution of 0.125 cm^{-1}. The signal was detected with a DTGS (deuterated triglycine sulfate) detector. (f) Light-current (LI) characteristics of a typical device at different temperatures (100ns pulse width at 1 kHz repetition rate). The power was measured with a fast MCT (Mercury-Cadmium-Telluride) detector that had been calibrated with a thermopile.

sitive laser designs share the benefit of other evanescent techniques, such as fiber based and total internal reflection based sensors, in that the sensing field is localized very close to a surface. By modifying the surface chemistry of the laser surface for specific binding of the analytes [52] sensitively can be increased in two ways. First, as shown in figure 2.19(b) with planar microdisks as an example, only particles drawn to the surface and therefore the near-field will be detected. Secondly, while the initial mixture could have a low analyte density, surface specific binding will encourage aggregation at the surface. For experiments that study properties such as conformational changes with modification of their aqueous environment this aggregation will be of great benefit. Work towards integration has taken two approaches. First is the integration of planar PC and microdisk lasers. Second is the integration with ridge waveguide lasers.

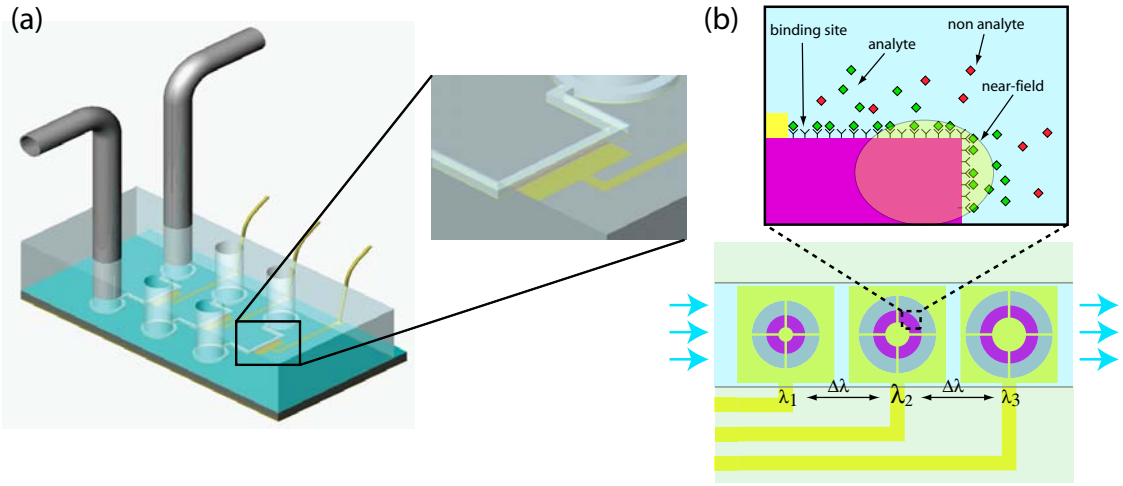

Figure 2.19: (a) Monolithic integration of PDMS microfluidic chip and planar QC laser chips. (b) Schematic of lithographically tuned microdisk lasers with a blow up showing specific binding of an analyte in the near field.

We have begun integrating planar QC microlasers by fabricating polymer based microfluidic chips. Several engineering challenges involving integration of microfluidic technology and surface sensitive QC lasers have been overcome. The first step in introducing fluids to a QC laser chip is to electrically and chemically isolate the fluid from the laser structure. We have developed a conformal deposition technique of SiN_x using plasma enhanced chemical vapor deposition capable of uniform 50nm films on 5μm vertical semiconductor walls. Microfluidic polydimethylsiloxane (PDMS) chips were fabricated using soft lithography techniques [53]. The microfluidic chips are bonded to a QC non lasing photonic crystal cavity chip with high fidelity adhesion as shown in figure 2.19(b) for illustration purposes. As shown in the inset of figure 2.19(b) several cycles of

channel filling with red colored water and then replacing it with blue colored water were carried out to mimic the introduction and emptying of channels of an analyte of interest, or the several steps needed for surface chemistry preparation and analyte delivery. Another engineering challenge to overcome is the native infrared absorption of the microfluidic chip itself. PDMS, while transparent in the visible has absorption in mid-infrared with minimum $\alpha = 71\text{cm}^{-1}$ at 7.5μm as measured by transmission FTIR (see figure 2.21(b)). The absorption is so strong that the optical properties of the laser will be difficult to observe directly through the PDMS chip. Fortunately microfluidic devices are not limited to polymer materials and mid-infrared compatible materials can be used.

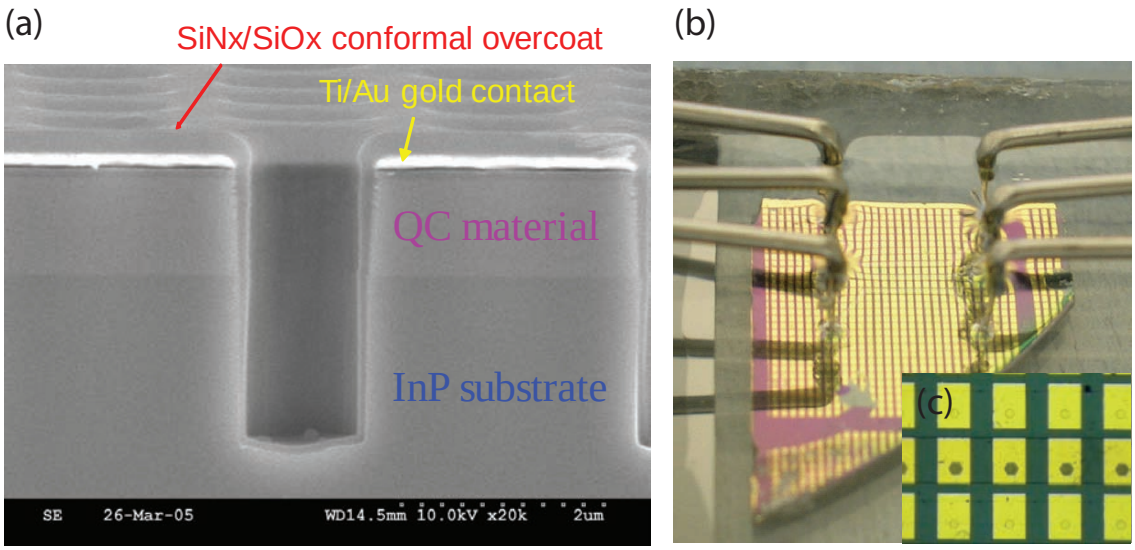

Figure 2.20: (a) SiN_x encapsulation of PC "test tubes." (b) Monolithic integration of PDMS microfluidic chip and planar QC laser chip. (c) Blow up shows flow of red colored water flowing through the sealed channel.

The air-confined microdisk design has several advantages over its ridge waveguide counterpart. The first advantage of the microdisk design is the huge savings in expensive laser material real estate. The microdisks designed are $4-7.5\mu$m in radius which is extremely small when compared to a length of hundreds of microns of a cleaved facet ridge laser or several millimeters of a conventional DFB laser. If each laser takes up an average real estate of 50μm by 50μm, including associated contacts and contact runs to the edge of chip, a density $d_{laser} = 400\text{mm}^{-2}$ can be achieved. Lasers with different diameters and therefore different wavelengths can be densely packed onto a single chip creating a multispectral array of single mode lasers. Another advantage of the microdisk lasers is that they emit vertically and do not extend to the very edge of the chip like cleaved facet lasers.

This leaves room for a continuous perimeter around the edge of the chip for sealing of a microfluidic device. Microfluidic chips can therefore be used to flow the same analyte over an array of lasers with different wavelengths. Monitoring of the laser's optical properties (intensity and wavelength) and electrical properties (current-voltage characteristics) will enable the mapping of the absorption spectra of an analyte, creating a chip based spectrometer. As a reminder, non-PDMS microfluidics would have to be designed.

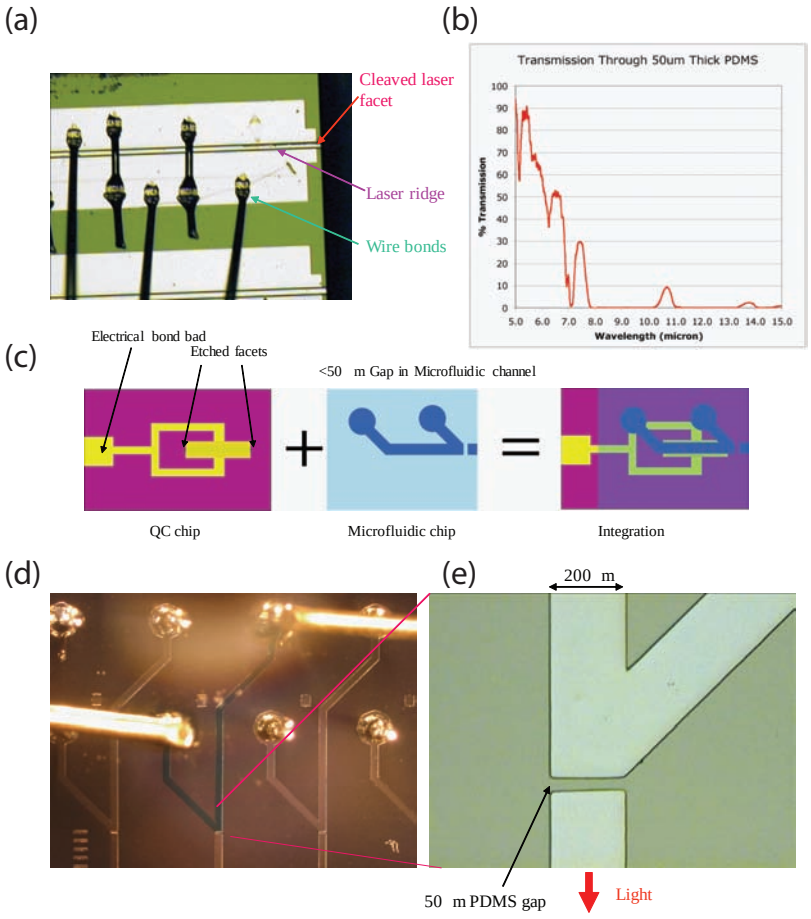

Figure 2.21: (a) Optical image of wire bonded cleaved facet air confined ridge laser (b) Absorption spectrum of PDMS. (c) Integration diagram. (d) Microfluidic chip designed for etched facet (planar) ridge waveguide laser. (e) Zoom in of thin region that would allow for light to escape.

Work has also been carried out toward the integration of air confined ridge lasers. The lasers currently fabricated are based on cleaved facets (see figure 2.21(a)), but the fabrication of etched facets should be possible. In that case one can then design an microfluidic chip to fully enclose them as indicated in a schematic in figure 2.21(c). PDMS chips were designed and fabricated with

the PDMS membrane facing the facets only 50μm PDMS. Such a thin membrane would allow for easily detecting the laser output.

2.5 Proof of Principle: Sensing of Isopropyl and Ethyl Alcohol

2.5.1 Introduction

I traveled to University Paris-Sud with the fluid delivery apparatus to carry out the fluid measurements with V. Moreau in Professor R. Colombelli's lab. The following section is in parts from reference [54]. When an absorbing material, such as a liquid, is deposited on a surface sensitive laser, the total propagation losses become frequency dependent, leading to a different transparency condition and lasing wavelength. It can also lead to an increase in the threshold current. Since the details of the frequency-dependent losses depend on the absorption features of the analyte deposited on the surface, these devices can be used as sensors. Figure 2.22(a) shows the principle of surface sensing employing air-guided QC lasers. A 2D finite elements simulation of the optical mode is superimposed onto the front facet of the laser ridge. It indicates that the mode is essentially located under the air. This characteristic yields an evanescent field, whose decay length is $\sim$ 500nm as deduced from the 1D simulation of figure 2.22(b), and from experimental measurements [55].

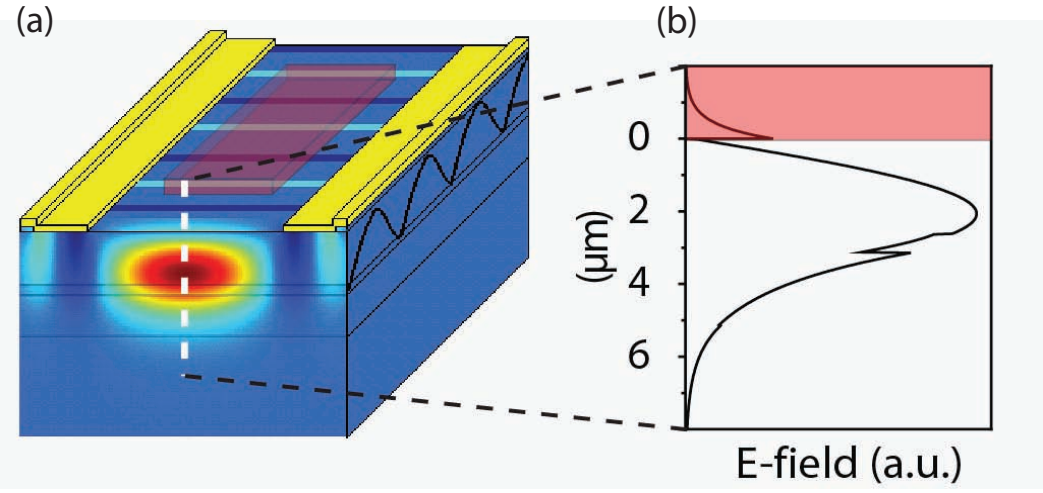

Figure 2.22: Principle of surface sensing employing an air-guided QC laser. (a) 2D finite element simulation of the laser mode (the magnitude of the electric field is shown) superimposed onto a schematic view of the device. (b) 1D section of the laser mode at the center of the ridge. The orange region is the air cladding above the device where the evanescent field penetrates, making the device sensitive to an external perturbation.

In this section, we show that indeed this class of devices is sensitive to an analyte or a liquid deposited on its surface, and that they are, in principle, suited to surface detection applications. The demonstration is corroborated by a theoretical model which is able to correctly predict the experimental results. In Section 2.5.2 the laser devices are detailed, as well as the setup used for the sensing demonstration. Sensing of both photoresist and common laboratory solvents is demonstrated in section 2.5.3. Finally a model is used to describe and understand the data in section 2.5.4.

2.5.2 Laser Devices and Test Setup

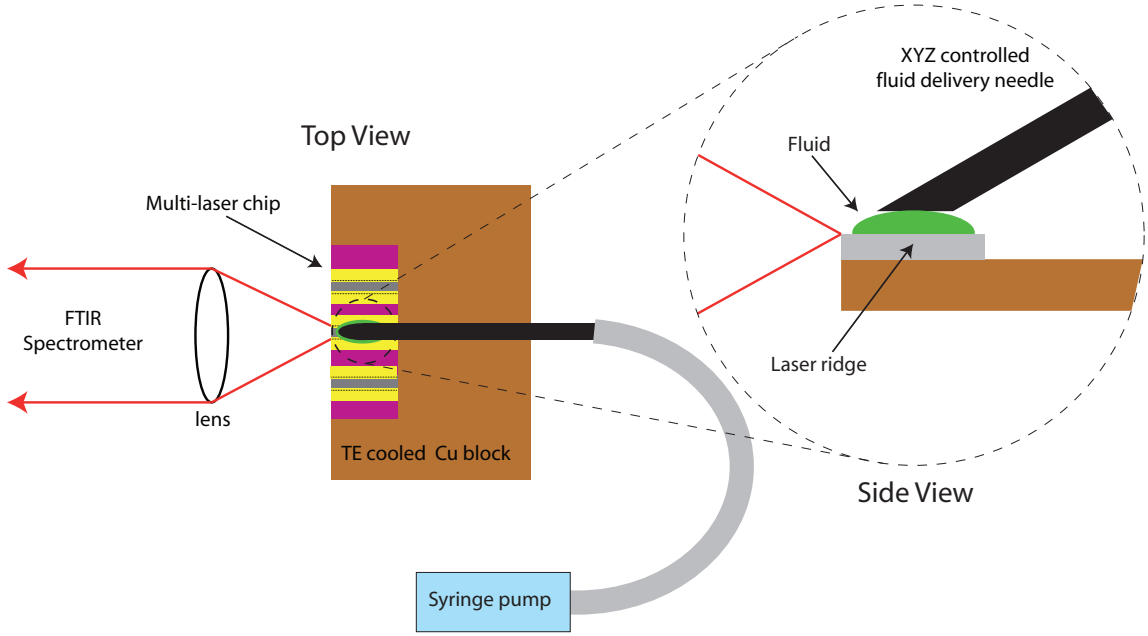

Figure 2.23: Sketch of the experimental setup used for the measurements. The laser devices are soldered with indium on a copper block and mounted onto a Peltier cooler. (a) Side view. (b) Top view. The emitted light is collected from the laser facet and fed into a FTIR spectrometer operated in rapid-scan mode, with a typical resolution of 0.125cm^{-1}. A liquid nitrogen cooled MCT detector was used.

Lasers described in Sec. 2.3.3 were mounted with indium solder on copper blocks, wire-bonded and characterized on a Peltier cooler. Laser spectra, light-current (LI) characteristics, as well as absorption spectra of test liquids (ethanol and isopropanol) were all taken using an FTIR. Shipley resist S1818, isopropanol (IPA) and ethanol have been employed to provide a proof-of-principle of the operation of the devices as sensors. A scheme of our setup for fluid delivery is shown in figure 2.24. To control the stability of a drop of liquid on the device top surface, we used a bevel shaped

needle and a push syringe connected to a syringe pump. The pump is operated at a speed that compensates for the solvent evaporation keeping a constant volume of solvent on the sample. Two CCD cameras are used for real-time control of the fluid delivery on the samples. Optical images of the drop and delivery needle over a ridge waveguide laser are shown in figure 2.25.

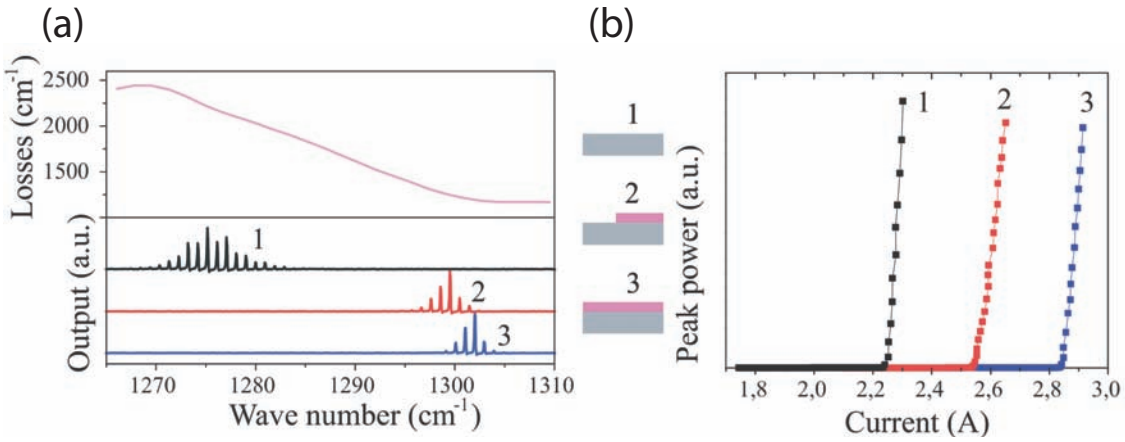

Figure 2.24: (a) Laser tuning upon S1818 photoresist deposition on the device top surface. Black curve: emission spectrum of the laser device before resist deposition. Blue curve: emission spectrum with the resist deposited on the top surface. Red curve: emission spectrum with the resist deposited on half the top surface. Purple curve: calibrated absorption spectrum of Shipley photoresist S1818, obtained via FTIR spectroscopy. The lasers were typically operated with 50ns wide pulses at a repetition rate of 84kHz. (b) Light-current-voltage (LIV) curve of the device without and with resist. The current threshold of the unperturbed device (black curve) is approximately 27% lower than the threshold when the resist is deposited on the surface (blue curve). When the resist is deposited on half the top surface (red curve) the threshold approximately 13% higher than the unperturbed case. The lasers were operated with 50ns wide pulses at 84kHz repetition rate.

2.5.3 Sensing

In order to demonstrate the surface sensitivity of the devices, Shipley photoresist (S1818) was used as a test absorbing analyte. We chose photoresist for the following reasons: first, it is well known that resist exhibits strong absorption features at mid-infrared wavelengths (see figure 2.24). Secondly it is relatively straightforward to deposit it with precision on top of the lasers using photolithographic techniques. The resist was spun onto laser devices already mounted on a copper block in order to have them previously tested. Selective sample exposure to UV light and development allows one to completely remove the resist from the copper block and from the sample facets, so the resist covers the laser top surface only. Care was taken in order to completely remove the resist from the laser facets. Figure 2.24 shows the results obtained from a 41μm wide laser ridge. A

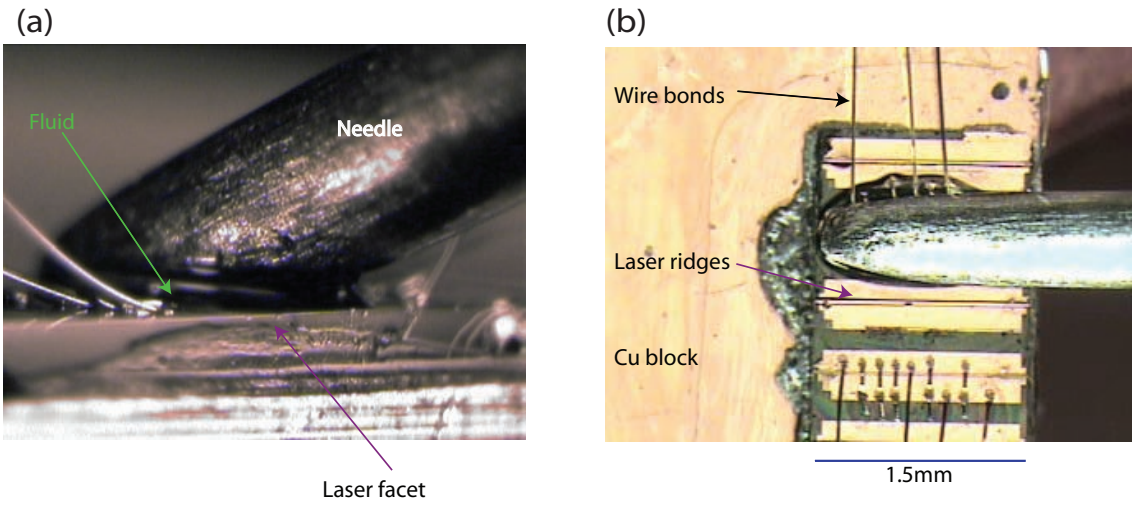

Figure 2.25: (a) Side view, i.e., cleaved edge view, of fluid delivery needle. (b) Top view showing ridge laser mesas.

global frequency blueshift of the laser spectral envelope of 27cm^{-1} (figure 2.24(a)), and an increase of nearly 27% in the threshold current have been observed (figure 2.24(b)). The absorption curve of the resist used for the test (Shipley S1818), as obtained with FTIR spectroscopy, is reported in figure 2.24(a). It presents a linear behavior with a negative differential absorption around the emission frequency of the laser. We expect therefore that the transparency condition will be reached at shorter wavelengths when the resist is deposited on the device top surface, since the analyte losses decrease with an increase in frequency. This prediction is correctly confirmed by the experiment. Furthermore, the resist deposition on the device top surface increases the total propagation losses, and the expected increase of I_{th} has been observed experimentally. In addition, when only half of the device surface is covered with resist the I_{th} increase is only 13%, showing that it scales linearly with the volume of absorbing material probed. The laser spectral envelope shift is in this case 25cm^{-1}. As a final check, the photoresist was removed with acetone and the devices were retested: emission frequency and I_{th} were the same as the values obtained prior to resist deposition.

Next, the variations of the emission frequency and the current threshold of the lasers were monitored to see if one can discriminate between two test chemicals. We chose to test the devices with isopropanol (IPA), ethanol and a mixture of both (50% IPA, 50% ethanol). The reason for this choice is the reasonably strong absorption exhibited by both the analytes in the 7.5μm-8μm spectral range of interest (see figure 2.5.4). Upon fluid deposition (with the technique described in figure 2.24), we observe a global frequency shift of the laser envelope of Fabry-Perot modes accompanied

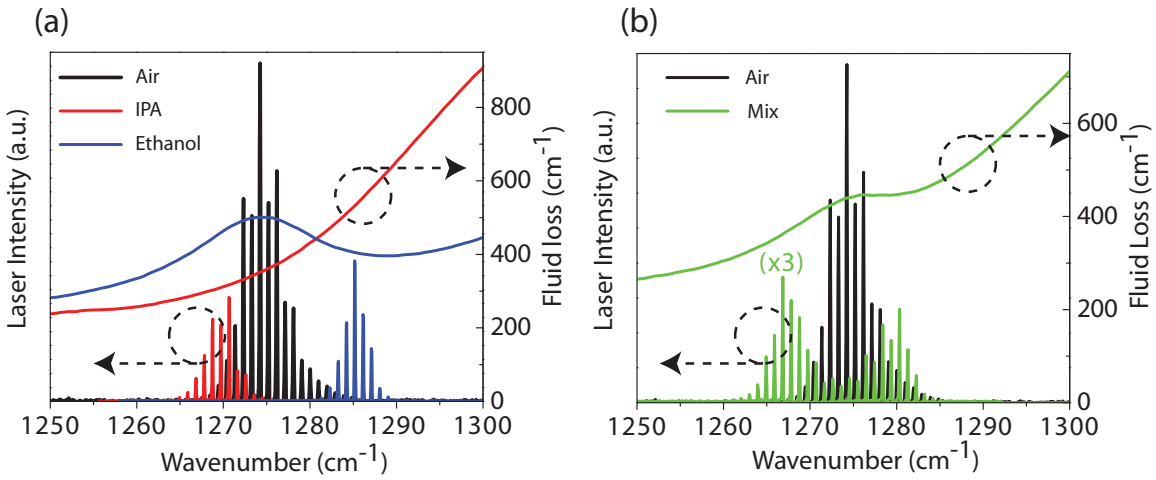

Figure 2.26: (a) Laser tuning of a 41μm wide air-guided QC laser upon ethanol (blue spectrum) and IPA (red spectrum) deposition. The black spectrum represents the unperturbed laser emission. The red (blue) curves represent the measured absorption of IPA and ethanol, respectively. The measurements were taken at 18C. The lasers were operated at 84kHz, with 50ns wide pulses. The signal was fed into an FTIR spectrometer and detected with an MCT detector. (b) Laser tuning with a 50%/50% mixed solution of IPA and ethanol (green spectrum). The green curve represents the measured absorption of the solution. Inset: frequency shift of the Fabry-Perot mode spacing upon fluid deposition. Black curve: without fluid. Green curve: with fluid.

by a small change of the mode spacing, as well as an increase of the laser threshold current. Figure 2.5.4 reports the spectral characteristics of a 41μm wide air-guided QC laser upon deposition of IPA and ethanol, respectively. The black curves represent the laser emission when no liquid is present. When IPA (ethanol) is deposited on the top surface, the envelope of the laser emission tunes from 1275cm^{-1} to 1270(1285)cm^{-1}, respectively. The measured absorption spectra of the two solvents are reported in figure 2.5.4(a) (red and blue curves). A comparison with the spectra demonstrates that the laser tunes its emission frequency in order to minimize the total loss, loss that is modified by the presence of the fluid on the top surface. It must be noted that ethanol shows a nearly symmetric absorption peak at a frequency of 1275cm^{-1}. A blueshift as well as a redshift can therefore be expected. However, free-carrier absorption must be taken into account. Since its magnitude scales approximately as λ^2, a blueshift to higher frequencies minimizes the losses, and it can explain what we indeed observe experimentally.

These results show that the spectral changes of the devices upon liquid deposition allow one to discriminate pure IPA from pure ethanol. One can wonder if a dilution of the two liquids can also be detected with the same system. Upon deposition of a 50%/50% mixed solution of IPA and

ethanol, an intermediate spectral behavior was in fact observed as shown in figure 2.5.4(b). We can approximately estimate the volume of liquid which can interact with the device near field. The typical device has an air-gap opening of 24μm. For a 1.5mm long laser, and considering that the evanescent field extends for 0.5μm above the sample surface, we obtain a volume $V = 0.18$pL. This value represents an estimate for the volume of liquid which is, in principle, sufficient for sensing with the proposed technique. A slightly better value of 10pL is estimated for the devices proposed in reference [56].

2.5.4 Analysis

In order to explain the experimental results, we introduce a theoretical model that allows one to write a simple expression for the total losses in the presence of an absorbing material (or liquid) in the device near field. By imposing the transparency condition (i.e., total losses equal to gain), we can obtain the laser emission frequency shift in the presence of the absorber on the device surface. A full theoretical model is developed is section 2.2.3.3. The laser material gain is modeled as a Lorentzian function centered at ν_g, with a full width at half maximum (FWHM) of 130cm^{-1} (10% of the central frequency). The total propagation losses per unit length of the laser are described as the sum of two contributions: waveguide (α_{wg}) and mirror (α_m) losses. The frequency dependence of the waveguide losses is assumed to be dominated by free-carrier absorption, and it is taken into account by adding a dependence proportional to ν^{-2} and to α_{wg} calculated at a fixed frequency ν_0. This is in general a good approximation. The presence of the liquid in the near field of the laser is taken into account via its complex index of refraction $n_a = n_0 + ik_a$ through first-order perturbation theory of Maxwell's equations. The index real part n_0 induces a minor shift of the laser frequency (see inset of figure 2.5.4(b)), while its imaginary part k_a induces, to first order, an increase in laser threshold. It can be shown in fact that the waveguide loss perturbation is proportional to the product $\Gamma_e k_a$, and therefore to $\Gamma_e \alpha_a$ (where α_a is the analyte absorption and Γ_e is the percentage of energy of the evanescent mode). Furthermore, a frequency-dependent loss will modify the transparency condition and it will produce a shift of the laser frequency as well. The shift can be actually much larger than the very small one induced by the real part only of the index of refraction. It is exactly this phenomenon that can successfully explain the experimental results.

Within this model, the total losses at a frequency ν, when an absorber is present in the laser near

Table 2.6: Parameter summary of laser structure for modeling spectra shifts due to application of solvent.

FWHM (cm^{-1})	ν_g (cm^{-1})	ν_0 (cm^{-1})	$\alpha_{wg}(\nu_0)$ (cm^{-1})	n_0	n_g	Γ_e (%)	R	L (cm)
130	1275	1300	9.03	1.4	3.25	0.192	0.28	0.15

field, can be expressed as follows (see section 2.2.3.3):

$$\alpha_{total}(\nu) = \alpha_m + \alpha_{wg}(\nu_0)(\frac{\nu_0}{\nu})^2 + \frac{n_g}{n_0}\Gamma_e\alpha_a(\nu), \tag{2.8}$$

where n_g is the modal group index. We introduced in the model the real absorbing curves of the solvents used for the experiment. The values for $\alpha_{wg}(\nu_0)$, Γ_e and n_g are obtained numerically with 2D finite elements simulations, while ν_g is assumed to be the emission frequency of the unperturbed laser. Table 2.6 summarizes the parameters employed in the simulation.

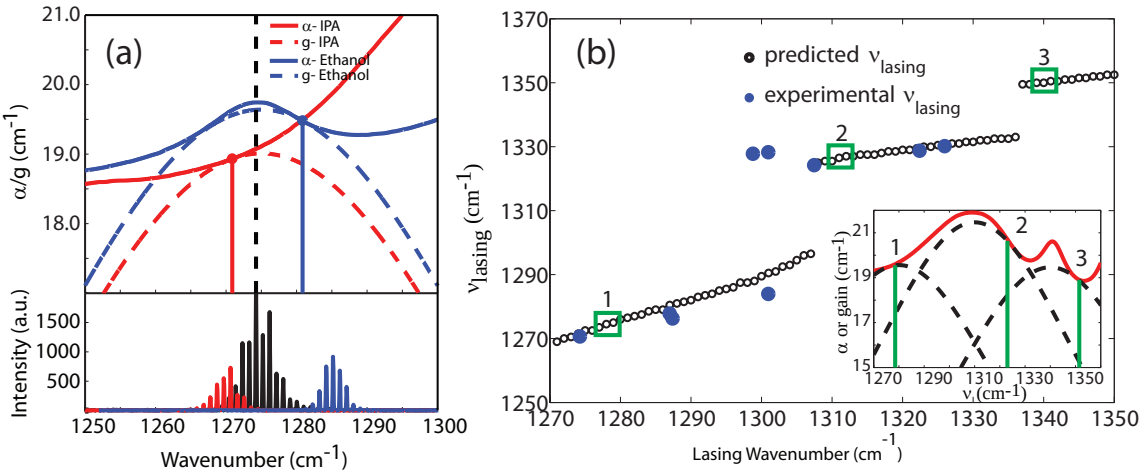

Figure 2.27: (a) Absorption model (b) Experimental (blue circle) vs. predicted (black circle) lasing frequencies for IPA as a function of initial frequency. Inset shows lasing condition for three characteristic initial frequencies.

The lasing threshold condition, gain equals loss, is then used to relate the loss introduced by the absorber to the lasing frequency and to its threshold current density. The theoretical results obtained by applying the model to the tested laser devices are shown in figure 2.27(a), together with a summary of the experimental results. The bottom part of panel (a) reports the emission spectra of the laser devices in the unperturbed case (black curve), and upon IPA (red curve) and ethanol (blue

curve) deposition, respectively. A global shift of the spectral envelope is clearly observable. The top part of panel (a) reports instead a visual representation of the lasing threshold condition in the presence of IPA (red curves) or ethanol (blue curves). The full lines represent the total losses in the presence of the analyte, as obtained from equation 2.8. The dashed lines represent the material gain at transparency: the tangential condition identifies the predicted laser frequencies (vertical full lines), which are found in good agreement with the experimental findings.

The experiments have been performed on several laser devices, each having a different initial emission frequency thanks to the inherent variability of processing, semiconductor wafer nonuniformity, etc. All the results, in the case of IPA detection, are reported in figure 2.27(b): ν_g is the initial, unperturbed laser emission frequency, and ν_{lasing} is the emission frequency when IPA is present in the device near-field. The black circles represent the prediction of the theoretical model, while the blue circles correspond to the experimental results. The agreement between theory and experiment is good, and it shows that the model indeed allows one to predict the laser behavior upon fluid deposition, and to discriminate, in this case, IPA from ethanol. Furthermore, the inset of figure 2.27(b) reports a visual representation of the lasing threshold condition for three characteristic initial laser frequencies, marked by the green rectangles in the main panel. It provides a direct, intuitive explanation for the presence of "jumps" in the predicted as well as in the experimental curves, and it further confirms that the proposed theoretical model can successfully predict the behavior of these surface sensors.

As for the current threshold, the model predicts an increase of 10.7% of I_{th} when IPA is deposited, and of 12.37% when ethanol is deposited, while the experiment yields and increase of I_{th} by 10.6% in both cases. The agreement between theory and experiment is fair. The small discrepancy between the predicted and experimental result for ethanol could originate from the confinement factor (Γ), which is modified by the presence of the fluid on the device top surface. We employed $\Gamma = 73.9\%$ for the unperturbed laser, and $\Gamma = 74.5\%$ in the presence of both ethanol and IPA. A better approximation would take into account their slightly different indices of refraction, yielding different confinement factors.

2.6 Conclusions

In this work we have simulated, fabricated, and tested surface sensitive QC lasers. We've developed microfluidic integration technology and have been able to show a proof-of-concept mid-infrared

QC laser based sensing of common laboratory solvents. Our proof of concept experiment matched up well with prediction. Overcoming drawbacks such as difficulty in integration, multimode lasing, and inability to easily wavelength tune such structures, will lead us towards PC and microdisk lasers already designed. Improvements in fabrication, design, and material availability would bring a fully integrated sensitive and portable sensor closer to reality.

Chapter 3

Design of Sub-wavelength Hybrid Surface Plasmon Waveguide Mode Microdisks

3.1 Motivation

In wavelength-scale lasers, the very small number of optical modes and small volume of the gain material allows one to probe the subtle and often interesting properties of lasing action [57, 58, 59, 60, 61, 62, 63]. Semiconductor microdisk lasers, in particular, have been actively studied due to their simple geometry and amenability to planar chip-scale integration with microelectronics [64, 65, 66, 67]. More recently there has been great interest in using surface plasmon (SP) modes at a semiconductor-metal interface for guiding as well as high intensity and sub-wavelength optical confinement [68]. There has been significant work on the incorporation of SP waveguides that double as contacts in mid-infrared quantum cascade lasers [69]. In the near-infrared there has been recent interest in increasing SP propagation lengths using SP-dielectric waveguide (WG) mode hybridization [70] and using the tight SP confinement for nanoscale metal coated lasers [71]. The Q and Q/V limits of SP based whispering gallery mode cavities has been studied both through simulation and experiments [72], showing that such cavities support SP modes with Qs greater than 1000 if surface roughness is controlled. With the miniaturization of electrically and optically pumped semiconductor lasers to the nano-scale, one encounters several design challenges that must be addressed, such as thermal management, proximity of metal contacts to the optical cavity, surface states, and demanding tolerance levels in fabrication. In this section we propose that metal contacts can be intimately introduced into a sub-wavelength microdisk semiconductor cavity with benefits. Mainly, high confinement and reasonable optical losses in close proximity to a very good thermal

heat sink. Since in very small structures the radiation loss is extremely high, one should treat loss due to metal, heat, and radiation on equal footing. Depending on the geometry, either one could be the main source of loss. We will explore the modes that exist in a microdisk cavity with varying degrees of metal coverage. As well as explore thermal properties of such structures.

Optical simulations will be divided into two sections. First, simulations will determine how small of an optical whispering gallery mode cavity we can make and still achieve lasing. Second, simulations will show how metal can be intimately incorporated into the cavity with benefit. The latter will be the focus of subsequent experimental work. To investigate the purposeful integration of a metal contact into the optical cavity of a sub-wavelength microdisk laser, we begin by designing a semiconductor microdisk cavity with no material or metal loss. We then incorporate a metal contact and follow the wavelength tuning and loss behaviour. We show that whispering gallery SP modes and WG modes hybridize into low-loss modes. A schematic of the model geometry is shown in figure 3.1. Finally a simple joule heating model will be used to simulate the temperature profile dependence on both disk pedestal and top contact.

3.1.1 Optical Simulations

3.1.1.1 Introduction

When designing optical cavities one must consider the potential sources of optical loss. The decay an optical field in a cavity can be parametrized by

$$U = U_0 e^{-\frac{\omega}{Q}t}. \tag{3.1}$$

Losses are therefore be typically measured by the magnitude of the parameter Q, the quality factor of an optical resonator. Qs associated with individual loss mechanisms can be added like resistors in parallel to get total loss

$$Q_{total}^{-1} = \sum_i Q_i^{-1}. \tag{3.2}$$

This means that the optical Q is really limited by its smallest component. Though semiconductor optical cavities have many sources of loss, we will begin by limiting ourselves to radiation loss to determine the scale of microdisks we can use. Available to us is high gain GaInAsP strained multi-quantum well active material from Bell Labs [12, 73]. Material epitaxy is shown in Table 4.1.

We therefore begin by modeling a 250nm thick disk with refractive index $n = 3.4$. Optical mode simulations are carried out in COMSOL Femlab according to reference [44].

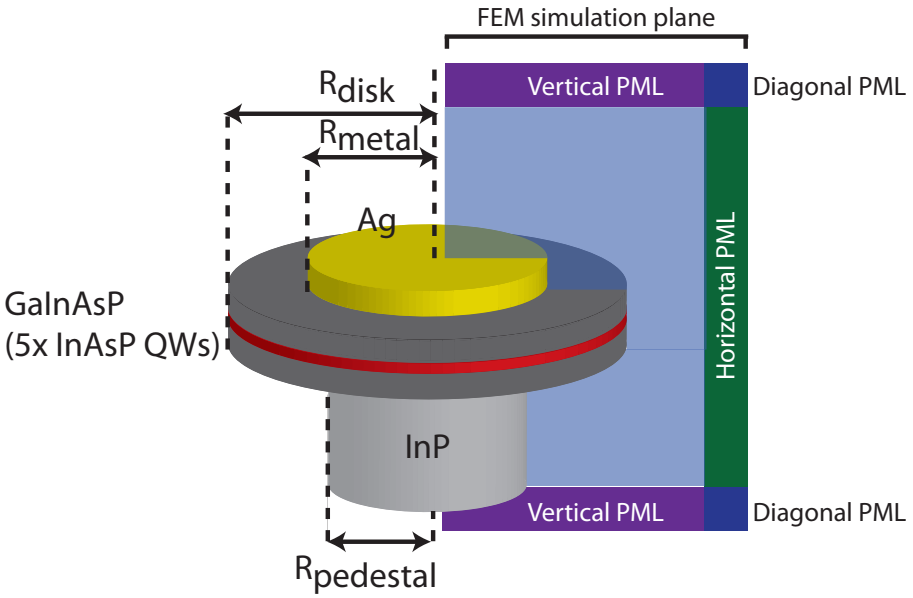

Figure 3.1: Schematic of geometry simulated. Orientation of simulation plane is illustrated.

A schematic of the full simulated structure is shown in figure 3.1. Simulations increase in complexity, first starting with just a disk and then adding the metal top contact. The simulation plane is a 2D slice of the structure as shown. The 3D simulation is then carried out in cylindrical coordinates. The simulation plane is surrounded by three perfectly matched layers boundaries. These layers are dielectric constant matched layers with strong imaginary component of their dielectric constant that absorbs light in the horizontal, vertical, and diagonal direction respectively. These layers prevent reflection of light back into the simulation plane and allow for simulation of Q. The simulation plane must start slightly away from $R = 0$ as the simulations in cylindrical coordinates will diverge for $R = 0$. Modes of a microdisk are classified according to: their polarization- transverse electric (TE) or transverse magnetic (TM), radial number (ρ), vertical number (v), and azimuthal number (m). Polarization is determined by looking for the dominant electric field component and the proper boundary conditions at the top, bottom, and radial face of the disk. For example a TE mode has a dominant E_r component with zero field at the outer radial boundary of the disk. TM modes have a dominant E_z component and a discontinuity at the top and bottom surfaces of a microdisk. The radial and vertical numbers are simply the number of lobes in the radial and vertical directions. The

azimuthal m number represents the number of lobes along the perimeter of disk and the momentum of the mode. Each simulation is carried out for a given geometry and given momentum, i.e., m number. Simulation eigenvalues are the propagation vector squared (k_0^2). Q and wavelength are extracted as follows:

$$\lambda_0 = \frac{2\pi}{\Re(k_0)}, \tag{3.3}$$

$$Q = \frac{\Re(k_0)}{2\Im(k_0)}. \tag{3.4}$$

3.1.1.2 Disk Simulation: Radiation Q

We begin with just a microdisk. The idea is to first establish the minimum disk size for a whispering gallery mode that still maintains a reasonable Q to function as a laser cavity. The radius R_d of the microdisk is varied systematically from $R_d = 400$nm to $R_d = 1\mu$m and the model is solved for optical modes. Q for both TE and TM modes is plotted in figure 3.2(a). As R_d is reduced, m is reduced appropriately to maintain the same free-space wavelength $\lambda_0 = 1.3\mu$m.

A linear decrease in Q on a semilog scale can be observed for both TE and TM modes. Dominant field components are shown in figure 3.2(c-d): E_r for TE and E_z for TM. The effective index of the modes can be estimated using an expression for the propagation constant $\beta = m/R_d$. The effective index for both TE and TM modes is shown in figure 3.2(c). The lower radiation Q of the TM mode corresponds to the lower effective index of the modes. We can now choose a radius below which we can not go with a simple disk geometry due purely to radiation loss. A Q of 1000 can be maintained for a disk that is as small as $R = 550$nm. We continue with a disk of $R_d = 0.65\mu$m that has a $Q \sim 10^4$.

3.1.1.3 Incorporate metal

We now incorporate metal into the design. Silver with an imaginary refractive index $n_{Ag} = 0.11 - i9.5$ at $\lambda = 1.3\mu$m is chosen as the metal contact due to its low loss [74]. Two azimuthal number $m = 6$ resonant modes are plotted as a function of metal radius. The data is plotted in normalized units of radial fraction (R_m/R_d). As R_m/R_d increases the modes slightly approach each other and then exhibit an anti-crossing behavior in resonant wavelength as shown in Fig 3.3(a). Concurrently, the quality factor (Q) of the same two optical modes is shown. At one extreme, where R_m/R_d is very small, the disk supports two high-Q modes, one (mode I) a transverse electric (TE) WG

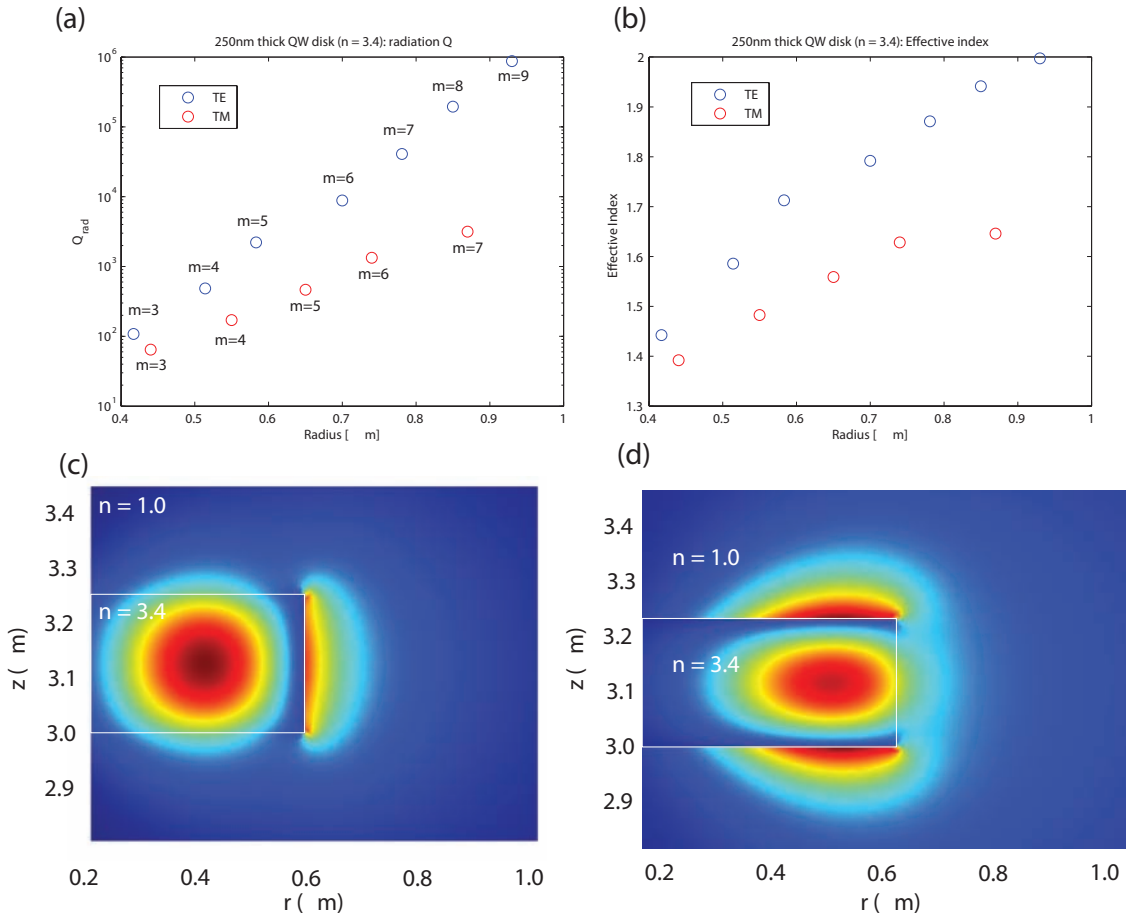

Figure 3.2: (a) Radiation Q of TE and TM modes (ρ = 1, v= 1) mode as a function of the radius of an ideal InP microdisk.(b) Corresponding mode index of TE and TM modes. (c) Dominant E_r component of a TE polarized mode. (d) Dominant E_z component of a TM polarized mode.

mode and the other (mode II) a transverse magnetic (TM) WG mode. At the other extreme when $R_m/R_d \sim 1$ the modes change in polarization into a TM SP mode and a TE WG mode respectively. Dominant electric field components for both cases are plotted in Fig 3.3(b)(c). As expected due to an increase mode overlap with the lossy metal, the Qs of both modes reduce as R_m/R_d increases, but remain above 1000 for significant metal coverage. In the region of hybridization a more complex Q behavior for mode II is observed. As metal coverage increases to $R_m/R_d = 0.55$ Q decreases to a minimum which is equal to the Q of mode I. It then recovers to a maximum at $R_m/R_d = 0.7$ before asymptoting to a Q value that is an order of magnitude larger than mode I.

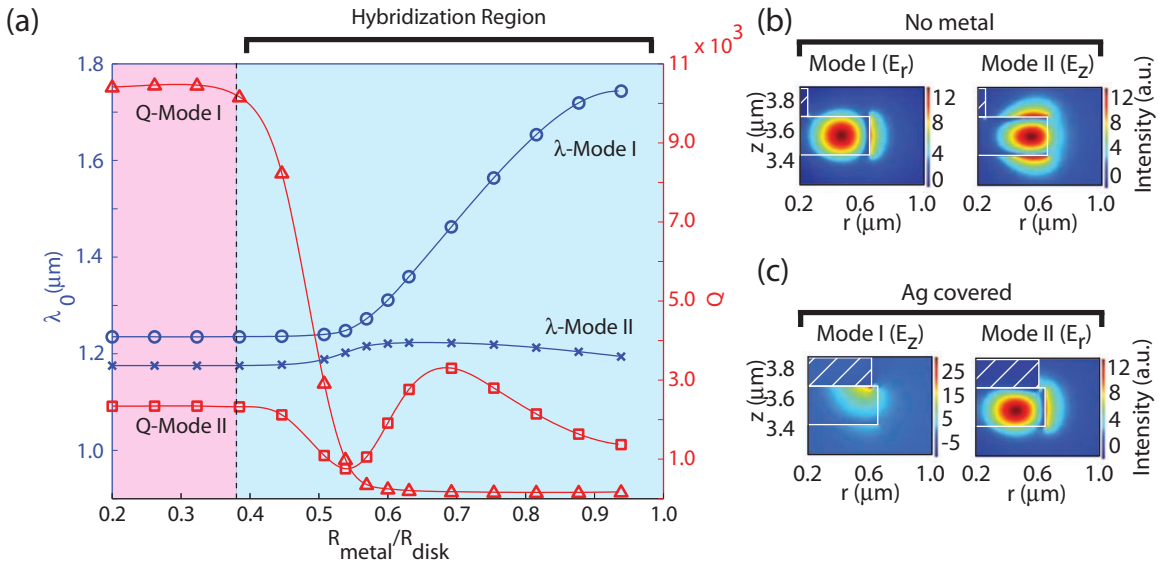

Figure 3.3: (a) A 250nm thick semiconductor disk with $R = 0.65\mu$m and a top silver contact is simulated with varying radial silver coverage. Wavelength (λ_0) and Q for two anti-crossing modes is plotted as a function of silver radius R_m/R_d. The dotted line highlights the transition from modes that are unperturbed by the metal contact and the hybridization region. (b) Plots of dominant electric field components for both modes without silver. (c) Plots of dominant electric field components with metal. Metal is denoted by white hatch marks.

Mode II is further simulated by adding an InP pedestal ($n = 3.2$) and adjusting $R_d = 0.7\mu$m so the resonant wavelength is $\lambda = 1.3\mu$m. The pedestal radius R_p is then increased incrementally while keeping an optimal $R_m/R_d = 0.7$ as shown in Fig 3.4(a). As R_p increases Q surprisingly increases to a maximum of $Q = 4000$ when $R_p/R_d = 0.8$. The radial electric field (E_R) component at optimal Q is shown in Fig 3.4(b). As R_p is further increased the Q plummets as the mode looses optical confinement. From these simulations a microdisk laser with significant metal coverage and very little undercut can be designed. It is interesting to note that the presence of the pedestal actually

improves the Q of the mode. Not only is this advantageous in Q this would be very advantageous in terms of thermal management, allowing for heat to be removed more quickly from the active material.

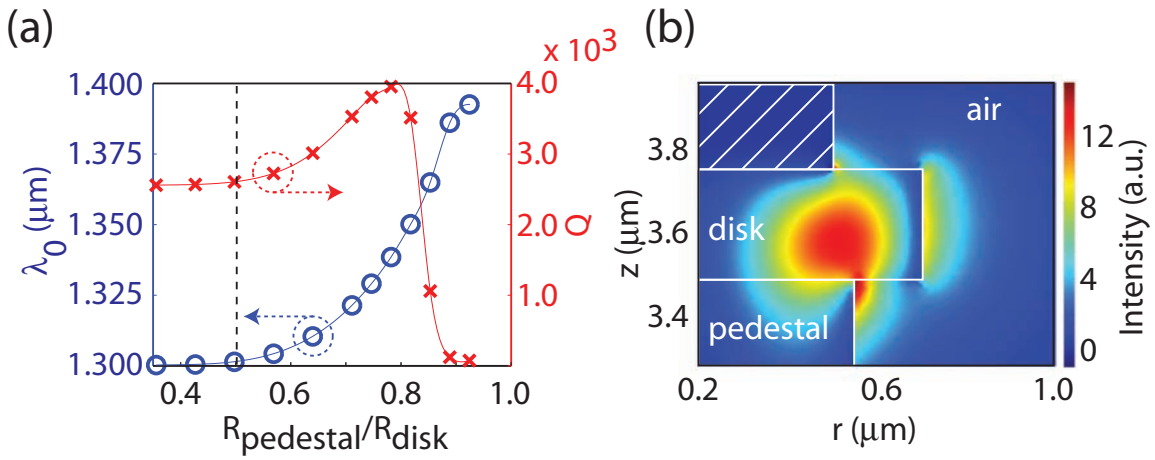

Figure 3.4: (a) Mode II is further simulated by adding in an InP ($n = 3.2$) pedestal. The disk radius is tuned so $\lambda_0 = 1.3\mu$m for no pedestal and an optimal $R_m/R_d = 0.7$ is chosen. Q and λ_0 are plotted as a function of increasing pedestal radius R_p in units of fractional pedestal radius R_p/R_d. The dotted line highlights the R_p/R_d at which the modes begin to be significantly effected by the pedestal. (b) Mode profile of the radial electric field (E_R) with optimal maximum Q with $R_p/R_d = 0.8$.

3.2 Thermal Design

In semiconductor lasers one of the major obstacles to laser performance is temperature. Heating of the laser material leads to modification of almost all parameters one uses to model laser thresholds: gain, carrier density, optical loss, etc. Due to the complex dependence on such parameters in some cases the effect of temperature on threshold current is just lumped into a simple exponential dependence: $I_{th} = I_0 e^{T/T_0}$ where T_0 is a characteristic temperature [25]. In the optical simulations in section 3.1.1.3 no distinction was yet made as to whether the laser material was optically pumped or electrically pumped. While the material we will use to experimentally verify anti-crossing mode behavior, the goal of this project would be to move things we learn regarding the laser behavior to electrically pumped material. This would enrich the physics of the structure as well as add another handle, current, on the behavior. Furthermore, it will make such a device more useful in commercial applications.

In order to account for thermal management in our design of small microdisk lasers we use a

simple joule-heating model. We use a laser epitaxial structure similar to the one we use experimentally, but with a diode structure incorporated to allow for electrical pumping. In this model a current is pumped into the top contact, through the microdisk device, and into the substrate. Resistive heating generates heat, and the heat diffusion equation with boundary conditions is solved to generate a temperature profile. Both the top of the silver contact and the bottom of the InP substrate are maintained at $T = 300K$. Each material layer is assigned an electrical conductivity, a thermal conductivity, density, and heat capacity. Thermal parameters for the semiconductor layers used are from ref. [7]. The electrical conductivities are estimated from carrier densities and mobilities from references [75, 76, 77]. The electrical conductivity of the QW and separate confinement regions is adjusted to induce a temperature profile that allows for qualitative observations. Epitaxy and model parameters are found in appendix B.

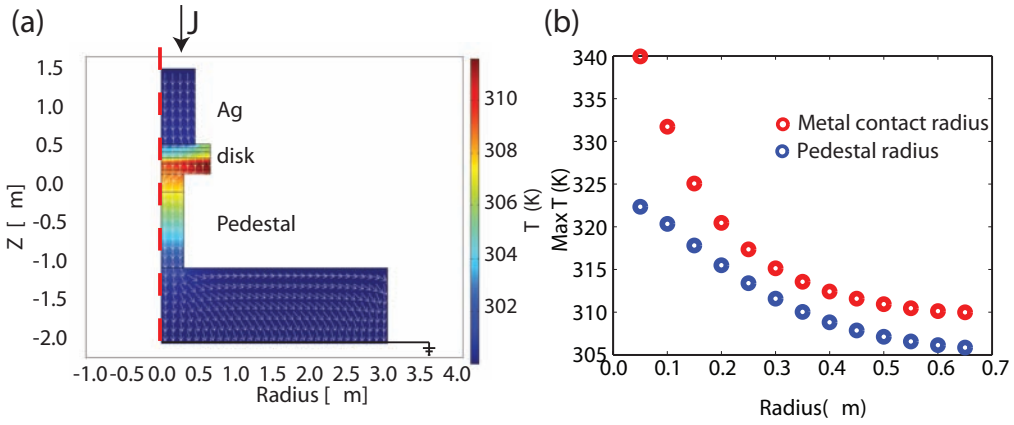

Figure 3.5: (a) Joule-heating thermal model of microdisk pedestal and metal contact. (b) Maximum temperature as a function of pedestal radius and contact radius.

A typical simulation is shown in figure 3.5 of a disk with radius $R_d = 650$nm. The simulation plane is revolved by 2π to form a 3D structure. The hottest area of the disk is towards the disk edge, where the optical mode generally is. Keeping the total current constant, the metal contact is varied from $R_m = 50 - 650$nm while the pedestal is kept constant at $R_p = 300$nm. The complement set of simulations is also done, where the pedestal is varied from $R_p = 50 - 650$nm, and the metal contact is kept constant $R_m = 450$nm. As is intuitive, the maximum temperature decreases with increase of either pedestal or metal radius. The rate at which it decreases is faster for the metal contact. This is consistent with the higher thermal conductivity of the silver contact. This qualitative thermal analysis gives credence to the idea that if metal could be incorporated into the optical cavity

without being the main source of loss it would be advantageous in improving laser characteristics by reducing the temperature. It is interesting to note that the Q increase in the modes simulated in figure 3.4 would be consistent with better thermal characteristics.

3.3 Conclusions

Microdisk with a radius of as small as $R_d = 0.55$ can be used to create optical cavities with a minimum Q of 1000. Furthermore a combination of metal coverage and pedestal can be used to fabricate a thermally more advantageous structure. Q of over 1000 can be maintained with even full metal coverage with slightly larger disks. A characteristic anti-crossing behavior in modes is shown as a function of radial metal coverage. In the next chapter we will fabricated optically pumped laser structures simulated here.

Chapter 4

Hybrid Mode Lasers–Fabrication Techniques

The fabrication of optical devices in active III–V semiconductors systems is a challenging process. When subwavelength scales are imposed and metal is incorporated the challenges become numerous. Submicron length scales demand high resolution, high-precision lithography. The incorporation of metal complicates the process further by changing thermal properties of the samples and adds chemical incompatibilities. Our ultimate goal in fabrication is to make an electrically contacted active optical cavity with precision control of metal coverage ans structure. This chapter focuses on fabrication technologies required to make high-quality InP based microdisks with metal contacts: fully covered, partially receded, and air bridged. This chapter is divided into three sections: fabrication of high quality GaInAsP microdisks is described in section 4.1, a Ti liftoff based process to create fully metal covered and air bridged microdisks is described in 4.2, and finally partially receded microdisk fabrication is described in section 4.3. Included in this chapter are fabrication techniques that did not yield fruit, but are nevertheless included, as they could be incorporated into others. My intention is that this chapter include details that may seem mundane, but will provide a foundation to future fabrication efforts.

4.1 GaInAsP Microdisk Lasers

We begin by fabricating GaInAsP microdisk lasers. While the growth of GaInAsP strained quantum well is very common for industrial applications, custom small growth runs can be very expensive and take several runs to develop. We work with a very small quantity of material, less than one 2" wafer with PL centered at $\lambda = 1.3\mu$m grown Bell Labs [12, 73]. Epitaxy layer information is

Table 4.1: Epitaxy for $\lambda = 1.3\mu$m membrane lasers. $1.12Q$ stands for quaternary GaInAsP layers, lattice matched to InP, with photoluminescence peak at 1.12μm ($Ga_{0.15}In_{0.85}As_{0.32}P_{0.68}$). The QW well layers are $InAs_{0.48}P_{0.52}$ and the barrier layers are $Ga_{0.24}In_{0.76}As_{0.32}P_{0.68}$. Total membrane thickness after undercutting sacrificial InP layer is 252nm.

Layer	Materials	Strain (rel. to InP)	Thickness (Å)	Doping (cm^{-2})
Separate confinement	$1.12Q$	unstrained	810	undoped
Half-barrier	GaInAsP	0.65% tens.	60	undoped
Active	5 wells	1.5% compressive	60	undoped
region	4 barriers	0.65% tensile	120	undoped
Separate confinement	$1.12Q$	unstrained	810	undoped
Sacrificial buffer layer	InP	unstrained	15,000	undoped
Etch stop	InGaAs	unstrained	200	undoped
Substrate	InP	unstrained	N/A	n/a

shown in table 4.1. From here on I will refer to this material as 5-QW material with epitaxial growth number $C1280$. A similar growth with only a single QW is referred to as 1-QW material with growth number $C1311$. Due to material scarcity we often carry out initial process development on either Si or InP wafers.

When wafers of active materials come in, in some cases indium residue used for thermal contact during the growth process remains on the backside. In order to insure sample flatness during processing and avoiding contaminating everything with indium it must first be removed. As the indium removing etch also can remove the active layers, the top surface must be protected. Shipley MEGAPOSIT SPR 220 resist is spun at 200RPM for 60sec on the top surface yielding an extremely thick layer of resist. Thick resist layers must be allowed to sit before bake for $\sim$ 1hr. The resist is then hot plate baked at 115C for 10min. It is important to allow for the wait time and hot plate bake as this allows the solvent to escape from the resist without creating significant bubbling in the resist. If the resist bubbles, the process must be redone, as it will lead to cracking and epitaxy damage in subsequent steps. The coated sample is then dipped in a 60ml weak piranha etch 1:1:5 H_2SO_4:H_2O_2:H_2O for approximately 30sec. The sample is than thoroughly rinsed with water and the resist is removed with acetone.

The process begins with deposition of a 350nm layer of Silicon Nitride (SiNx) via plasma enhanced chemical vapor deposition (PECVD). Deposition parameters are tabulated in Table 4.2. Samples are then spun with ZEON ZEP520A at 2500RPM for 60sec and oven baked at 180C for

Table 4.2: PECVD of SiNx: Process conditions. Deposition is carried out in 20sec cycles of low and high frequency power to reduce stress build up during growth. Deposition rate is $\sim$ 13.5nm/min

Parameter	Value Requested	Actual Value
SiH_4/N_2	400sccm	(396sccm)
NH_3	20sccm	(19.8sccm)
N_2	600sccm	(591sccm)
High Frequency	20W/13sec	(20/1W)
Low Frequency	20W/7sec)	$(16/6-7W)$
P	650mTorr	(650mT)
T	300C	(300C)
t	26min	

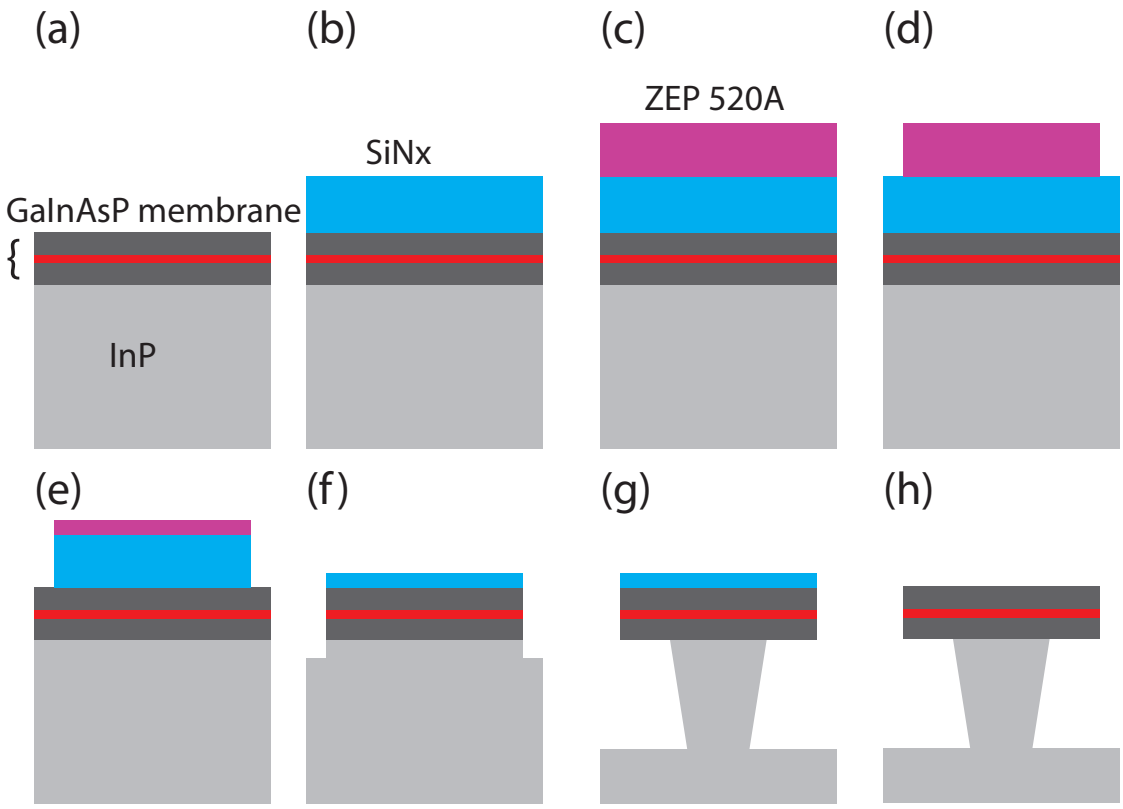

Figure 4.1: Fabrication flow for GaInAsP membrane microdisks. (a) Starting 250nm thick GaInAsP with 5 strained quantum wells. (b) Deposit 350nm of SiNx. (c) Spin electron beam resist. (d) Electron beam lithography. (e) SiNx etch. (f) GaInAsP etch. (g) Undercut. (h) Remove SiNx.

20min, yielding a layer that is $\sim$ 450nm thick in preparation for electron beam lithography. A very brief $3-5$sec dip in Buffered HF Improved (Transene) was carried out to aid in adherence of the resist. In our lab, electron beam lithography is done on a modified Hitachi S4300 scanning electron microscope. The scan coils are controlled by a separate computer via a National Instruments data acquisition card. Using software developed several years ago [50], a voltage with a range of $\pm$10V, corresponding to the field of view at a given magnification, is a applied to the scan coils in a raster fashion. In this section, lithography is done at 15KeV accelerating voltage with a magnification of 1000x, corresponding to a field of view of $\sim 77\mu$m yielding a minimum beam step size of 1.2nm. To hasten the beam writing process only every 12th pixel is written yielding a beam step size of 14nm. The first step of every electron beam lithography process is the optimization of exposure dose. A dose test from $20-36\mu$Ccm^{-2} in steps of 1μCcm^{-2} is carried out on a SiNx coated Si sample. Lithography is developed for $2:30$min in ZEON ZED-N50 and rinsed in ZEON ZMD-D. A set of SEM micrographs exhibiting over exposed, well exposed, and underexposed disks is shown in figure 4.2. Overexposure yields a significantly undercut lithography good for liftoff processes. The perfectly exposed lithography yields vertical side walls. Finally, underexposure leads to overcut side walls and resist residue on the SiNx surface. It must be noted that due to proximity effects, beam writing on Si is not simply transferable to InP based materials, though it does give a good starting point for further optimization. Optimized beam writing conditions on C1280 material is a dose of 26.8μCcm^{-2} with beam current of $\sim$ 12pA as measured at the Faraday Cup. Beam writing is kept under 100kHz.

While one can control the profile of the side walls by either overexposing or underexposing the lithography, the resist can also be heated above its glass transition temperature of 105C in order to reflow the edges. A series of reflow conditions is shown in figure 4.3. When reflowing the resist one must strike a balance. Unreflown resist can be slightly rough and susceptible to mask erosion as the vertical edge gets damaged. Overreflown resist has too thin of a profile leading again to uneven etching along the edges. Perfectly reflown resist gives a profile that is worn down in an even fashion during the subsequent dry etch, as well as have had undergone enough of a change in shape for surface tension to have smoothed out some of the imperfections in the lithography. Reflow conditions can depend on the surface on which the resist is spun. For SiNx microdisk etching optimal reflow conditions are 7.5min at 145C.

Once the resist mask is optimized, the hard SiNx mask is etched using inductively coupled plasma reactive ion etching (ICP/RIE) with C_4F_8/SF_6 gas chemistry. The mechanism of ICP/RIE

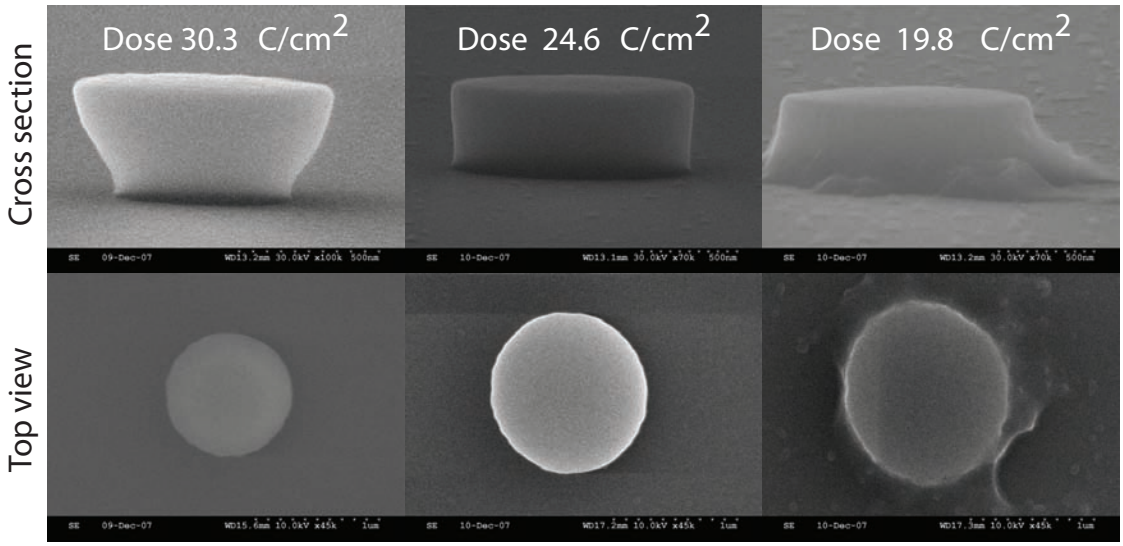

Figure 4.2: ZEP 520A spun at 2500RPM, substrate: SiNx on Si, Beam write speed $<$ 100kHz, Magnification 1000x, Resolution: 15nm

Table 4.3: ICP/RIE – SiNx etch conditions. Etch rate $\sim$ 35nm/min. SiNx etch is very sensitive. Conditions can slightly change based on chamber conditions. Chamber is always conditioned for $5-10$min. RF power is adjusted to maintain a DC bias of 30V.

Parameter	Value Requested	Actual Value
RF	4-6W	(4-6/2W)
ICP	1000W	(969/3W)
DC Bias		30V
C_4F_8/SF_6	17/11.5sccm	(16.8/11.5sccm)
P_{ch}	15mTorr	(14.4mT)
P_{He}	15Torr	(4.5sccm)
T	20C	$(24-25$C)
t	2min	

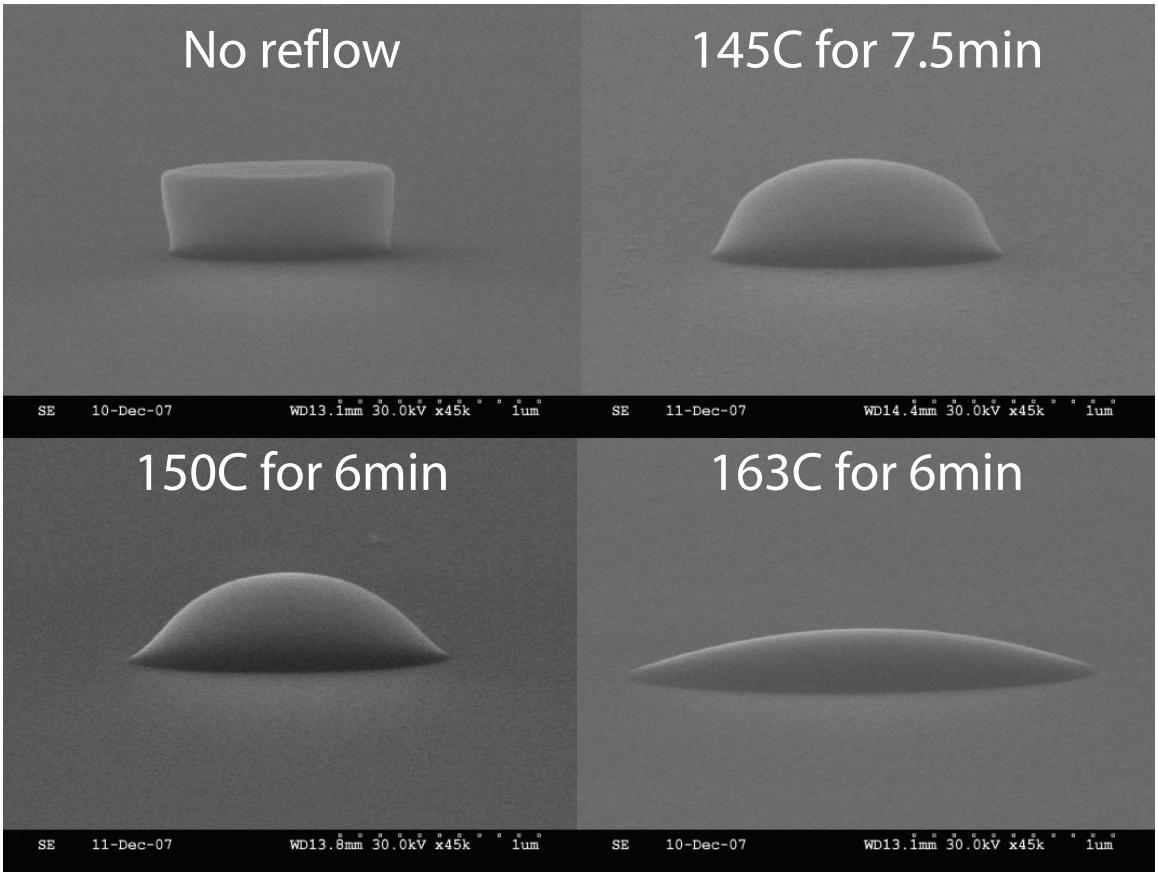

Figure 4.3: Results of different reflow conditions. Substrate: SiNx on Si, resist: ZEP 520A spun at 2500RPM for 60sec. Bake at 180C for 20min. Develop: 2:30/0:30min ZED-N50/ZMD-D. Dose: 26.8μm. Magnification: 1000x. Resolution: 15nm.

Table 4.4: ICP/RIE – GaInAsP/InP etch conditions

Parameter	Value Requested	Actual Value
RF	150W	(148/7W)
ICP	400W	(384/2W)
DC Bias		$\sim$ 302V
Cl_2/Ar	5/15sccm	(4.6/14.7sccm)
P_{ch}	3mTorr	(2.5mTorr)
P_{He}	-	-
T	20C	(25)
t	2min	

etching can be very crudely divided into two components. First, RF power is applied to a large inductor surrounding the top of the chamber stripping electrons from the gas mixture. Electrons are grounded to the chamber walls and an ion plasma is formed. A second RF source applies power to the electrode on which the sample sits on and the ions are driven into the surface. This gives two handles on the etch: ionization of the plasma, i.e., ICP power, and the kinetic energy of the ions hitting the sample i.e. RF power. SiNx etching gas mixture also serves as a handle on the etch quality. The C_4F_8 deposits a thin polymer layer allowing for the SF_6 to etch at the surface. As the C_4F_8 concentration is increased, the polymer protects the side walls allowing only the bottom surface (where most of the kinetic energy is directed) to etch. This yields a very smooth etch. Too high of a concentration leads to a significant decrease in etch rate and unstable plasma. Too low of a concentration leads to a very rough etch which would transfer into the GaInAsP material during subsequent etching. Helium backing is used to cool the wafer from below. A SiNx etch on C1280 material is shown in Fig 4.4. The resist mask is then removed by sonicating the sample in trichloroethylene for 10min on level one.

The mask is then transferred from SiNx into the GaInAsP disk using Cl_2/Ar ICP/RIE etch. The Cl_2 is the chemical component and the Ar mill is kinetic. ICP/RIE etch parameters are tabulated in table 4.4. Typically InP based materials are etched at an elevated table temperature. It is worthwhile to note that we are able to etch extremely smooth side walls $\sim 1.5\mu$m deep at room temperature, relaying only on the ICP power and RF power for heating. Roughly 170nm of SiNx hard mask remains. An SEM micrograph of the GaInAsP/InP etch is shown in figure 4.4(b). The devices are then undercut by removing the sacrificial InP layer in cold $T = 4$C 4:1 solution of HCL:H_2O for 15sec. SEM micrographs of the undercut devices and a zoom in showing the quality of the GaInAsP

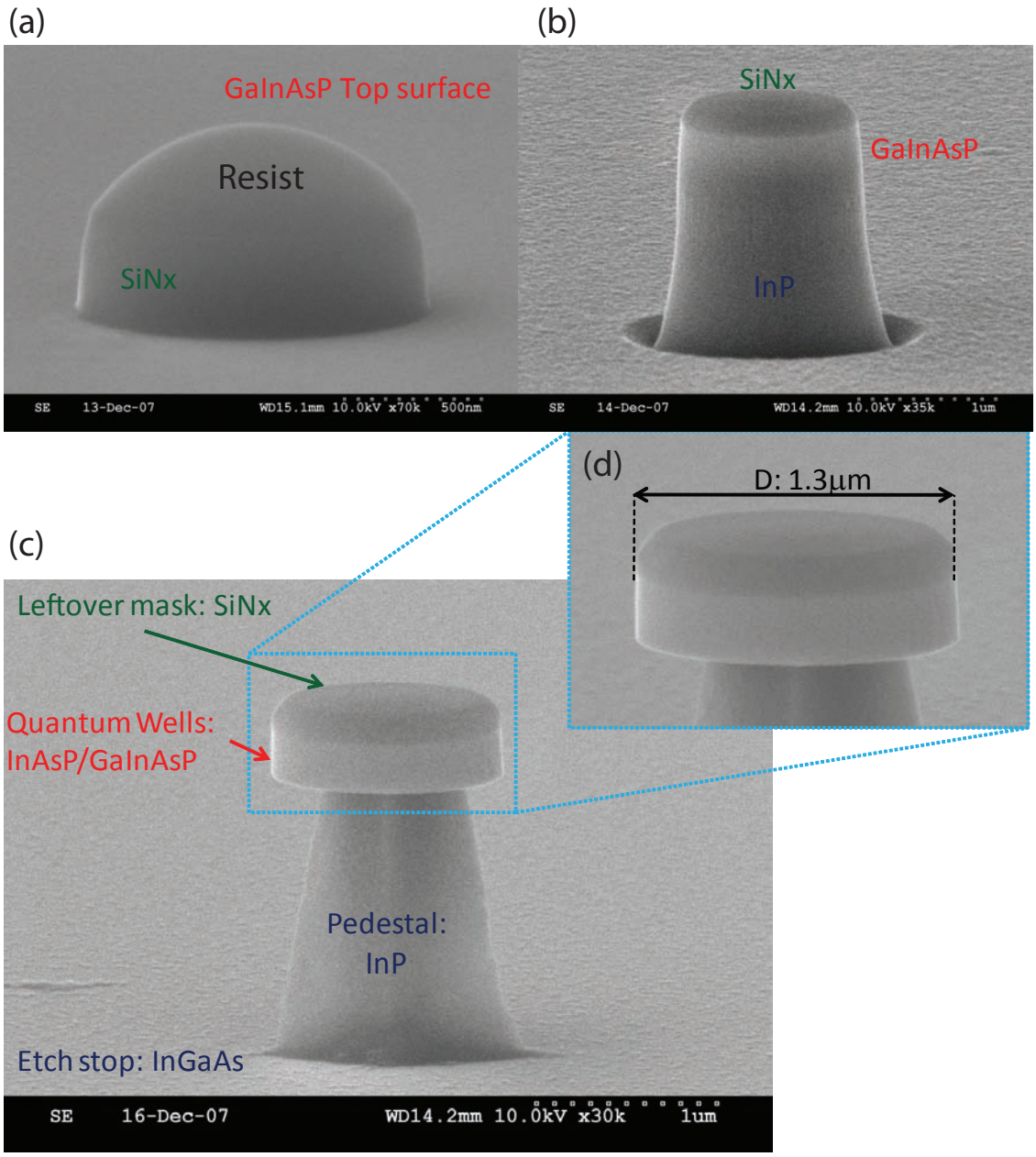

Figure 4.4: (a) SiNx etch via C_4F_8/SF_6 based ICP/RIE. (b) GaInAsP/InP etch via Cl_2/Ar ICP/RIE. (c) Undercut of InP sacrificial layer using HCL based wet etching. (d) Close up of exceptionally smooth GaInAsP microdisk.

etched surface are shown in figure 4.4(c)(d). This etch is extremely fast and a bit unpredictable in time. It is possible that an oxide forms on the disk surface preventing etching, but once the oxide is removed the etch rate is extremely fast. In general, several samples are needed for a successful undercut. Finally the SiNx can be removed by either an ICP/RIE SiNx etch with low DC bias (DC$\sim$ 20V) or in this case removed with 10:1 HF:H_2O (Hydrofluoric starting concentration is 49%.) A final set of SEM micrographs shows another set of devices with extremely thin supports before and after SiNx removal via HF are shown in figure 4.5. A small ring of residue appears to be left along the top circumference of this disk. The may possibly be removed with a dry SiNx removal etch.

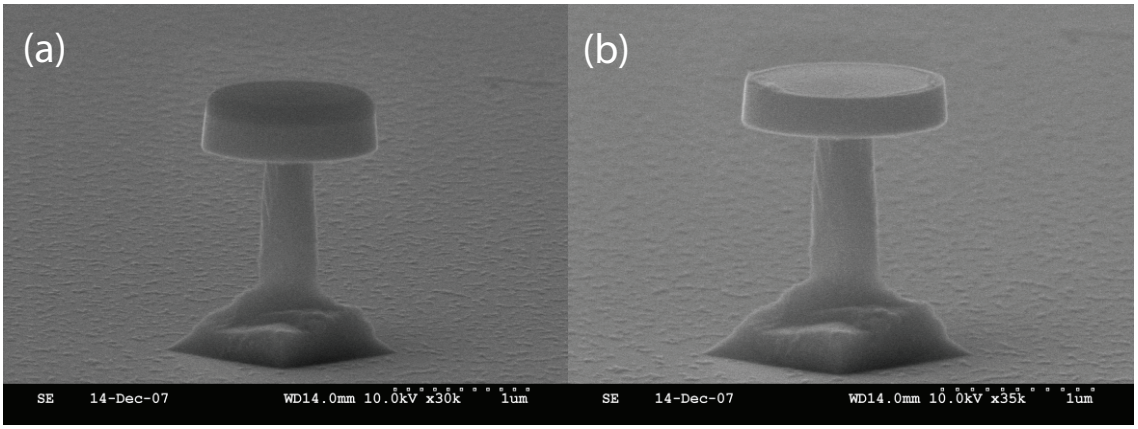

Figure 4.5: GaInAsP compressively strained 5-QW microdisk before (a) and after (b) hydrofluoric acid based SiNx removal.

4.2 Metal Coated Microdisk Cavities

Now that we are able to make high quality GaInAsP based microdisks we move to developing fabrication techniques for full and partial metal coverage as well as well as air bridging technique. Several techniques that have yielded only partial results are included for the possibility of future development.

The first approach emulates an approach we took to the fabrication of quantum cascade (QC) lasers of etching straight through the metal contact. Both InP as well as C1280 samples are coated with Ti/Au 10nm/90nm contact via electron beam evaporation after which a 350nm SiNx hard mask was deposited. This process is similar to the one in section 4.1 so I will just highlight the

differences. Electron beam lithography dose was increased to $37.7\mu\text{Ccm}^{-2}$, develop/rinse times were 3min/30sec, and reflow time was 6min at 163C. The nitride etch gas chemistry C_4F_8/SF_6 was 15.5/12sccm and etch time was $t = 18$min. The longer etch time can be attributed to the cooling provided by the metal contact. The SiNx etch roughens the surface of the Au when it finally penetrates as can be seen in figure 4.6(a). When the pattern is transferred into the GaInAsP material this roughness is transferred. When optimizing this etch there is a balance in both RF and ICP power applied. Too much power and the Au actually smears along the side walls. This would obviously induce optical loss. Not enough power and a "grass"-like texture forms at the bottom surface. This is typical of an InP etch that has not gotten warm enough. A power compromise etch is shown in figure 4.6(b) where RF/ICP are 100/400W and the etch time $t = 2.5$min. The devices are then undercut in HCL solution in several minute-long increments at 10C. This undercut is noticeably slower than in section 4.1. A device post undercut is shown in 4.6(c). These devices are not optically smooth, but we decided to try and recede the metal. For that purpose we used a cyanide based etchant (Au etch TFAC from Transene). 28.3 grams were dissolved in 473ml of deionized water. The solution was warmed to 60C and sample was etched for a total of 45sec in increments of $10-15$sec. Each time the sample was rinsed for 30sec in DI water and SEMed. The final result is a disk with metal recession of ~ 300nm. Unfortunately the Au etch is quite rough.

Since neither disk etch nor metal disk etch looks extremely promising, we take a different approach. As it may also be useful to test mode hybridization in a passive microdisk, we begin by working on a 250nm thick low pressure chemical vapour deposition (LPCVD) SiNx membrane on Si. Similar to the previous approach we deposit the contact layer. This time around we deposit a Ge/Ag/Au/Ti 10/100/140/10nm for two reasons. The first is the Silver is a low loss surface plasmon metal [74]. The second was a short paper detailing extremely smooth Ge/Ag films [78]. It is worthwhile to note that for these thicknesses the Ag film is not exceptionally smooth as compared to reference [78]. Electron beam resist is then spun onto the sample as usual, but this time a liftoff mask consisting of holes is beam written. Beam write dose was $D = 45\mu\text{Ccm}^{-2}$ and develop time was 2.5min/30sec. Titanium was then evaporated (without rotating sample during evaporation) to a thickness of 225nm. Liftoff was carried out using trichloroethylene soak for 15min, 5min in acetone (spray at sample), and a final 1min in isopropyl alcohol. It should be noted that its not uncommon to see resist cracking after the evaporation process. These cracks most likely appear after the deposition, perhaps during the cool down of the samples as they do not transfer to the sample below. The metal along with the LPCVD SiNx disk was etched using an Ar ICP/RIE mill (conditions in

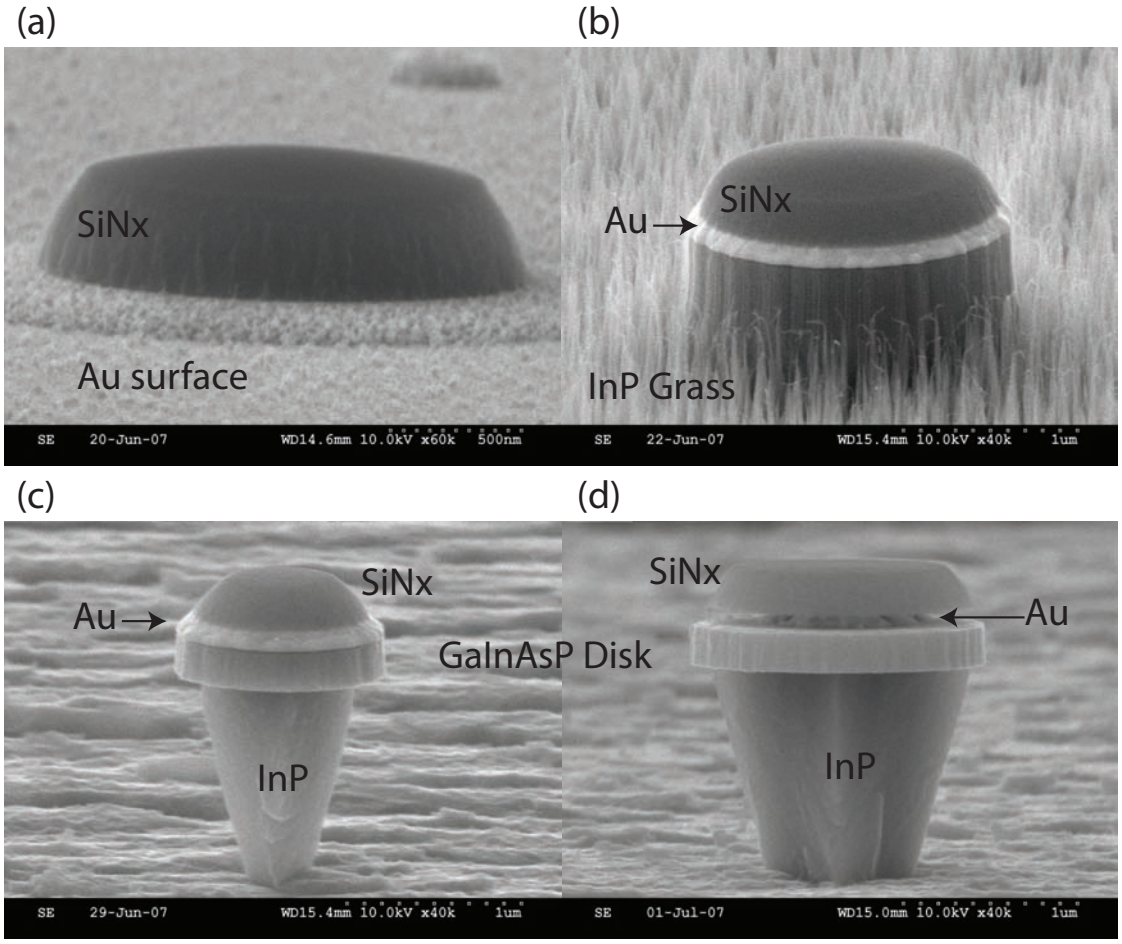

Figure 4.6: (a) SEM micrograph of SiNx mask etch. Etch partially goes into Au contact layers. (b) SEM micrograph of GaInAsP/InP ICP/RIE etch. InP "grass" is seen on the bottom surface. (c) SEM micrograph of undercut disk. (d) SEM micrograph of Au receding etch.

Table 4.5: ICP/RIE - Meta; Argon (Ar) mill

Parameter	Value Requested	Actual Value
RF	250W	(248/6W)
ICP	350W	(336/2W)
DC Bias		$\sim$ 430V
Ar	20sccm	(19.6sccm)
P_{ch}	3mTorr	(2.5mTorr)
P_{He}	-	-
T	20C	(25)
t	5min	

table 4.5) as the C_4F_8/SF_6 ICP/RIE completely destroyed the contact. The disks were then undercut using potassium hydroxide (KOH) solution heated to 75C for a total of 30sec. Each fabrication step is shown in figure 4.8.

In order to recede the metal we attempt to use a KI:I_2 based etchant (TFA Au etch, Transene). Undiluted rate is quote as 25nm/sec so the solution is diluted to 50% and the sample is etched for 7sec at room temperature. A very nice recession of 210nm is achieved. While it's not clear why, unfortunately this metal recession can not be achieved once the disk is undercut. Before and after SEM micrographs are shown in figure 4.9

A similar Ti liftoff process was carried out on a single QW sample (C1311 material). The contact was etched via the same Ar mill for a total of $t = 13$min. The typical Ar/Cl_2 based ICP/RIE etch could not be used as it destroyed the metal contact. The results of both process steps are shown in figure 4.10. While these devices do not look very promising in terms of optical smoothness, they do give us a chance to explore air bridging technology.

We have developed an air bridge technique using a Cytop (Asahi Glass Co.) polymer planarization layer. This technique is similar to the one used in reference [71]. Cytop is a chemical and temperature resistant perfluoropolymer with excellent optical properties. In this process we use it as a planarization layer. The idea is to cover and planarize microdisks with an existing metal contact and back etch the polymer layer until just the contact is showing. Then an air bride contact can be deposited on top of the polymer. Either a wide area contact or a patterned contact can be fabricated.

In order to planarize already fabricated disks a very thick $\sim 2\mu$m layer of Cytop must be spun onto the samples. We do this using a 3-spin method. Each spin consists of 10sec spin at 500 RPM to spread the polymer, and 20sec at 4000 RPM followed by a 10min hot plate bake at 100C. Three

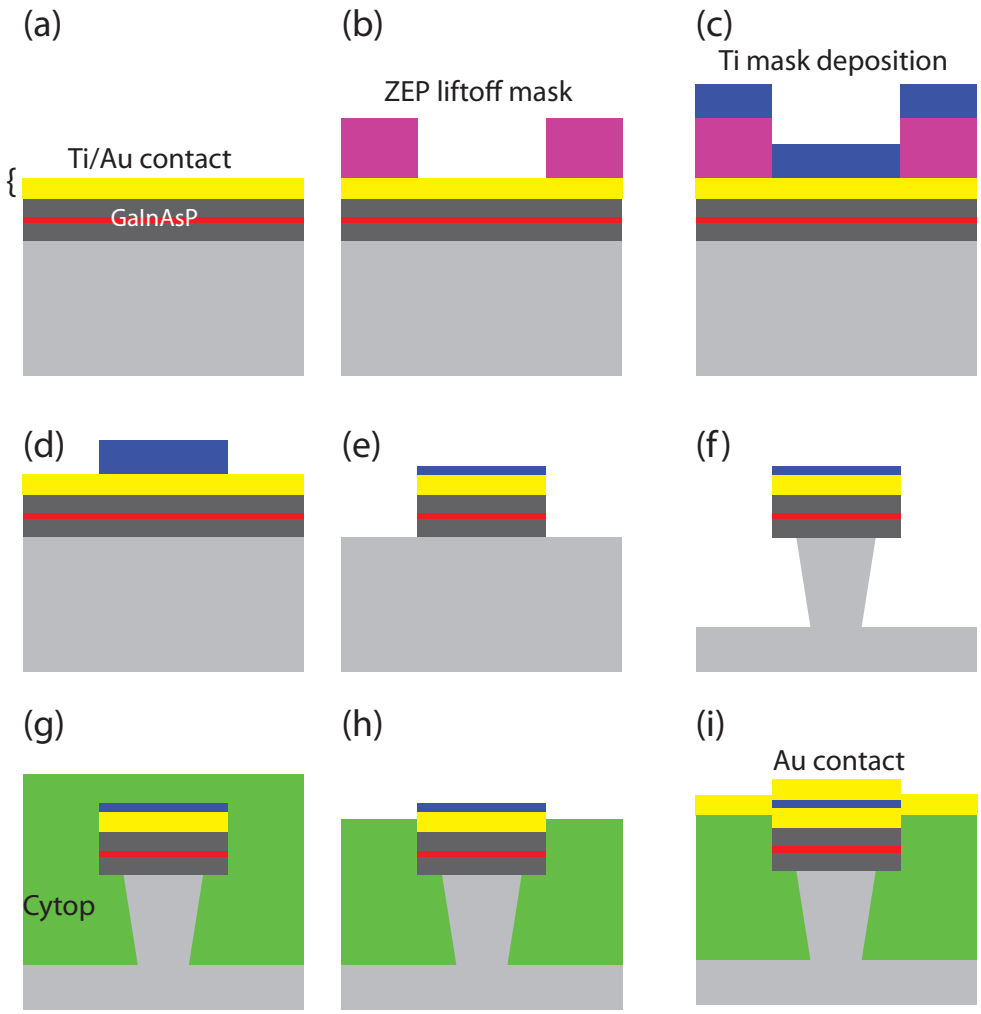

Figure 4.7: Fabrication flow for GaInAsP membrane microdisks using a Titanium liftoff mask: (a) GaInAsP is covered with a Ti/Au contact layer. (b) Electron beam resist is spun on and a liftoff pattern is created via electron beam lithography. (c) A Ti layer is then deposited via electron beam lithography. (d) Ti mask is formed via liftoff. (e) The GaInAsP microdisk is etched using an Ar mill. (f) The disk is then undercut via cold HCL solution. (g) In order to create an air bridge, a polymer (Cytop) is used to planarize the sample. (h) The polymer is etched back using an O_2 plasma etch. (i) A final Au layer is deposited via e-beam evaporation to create the bridge.

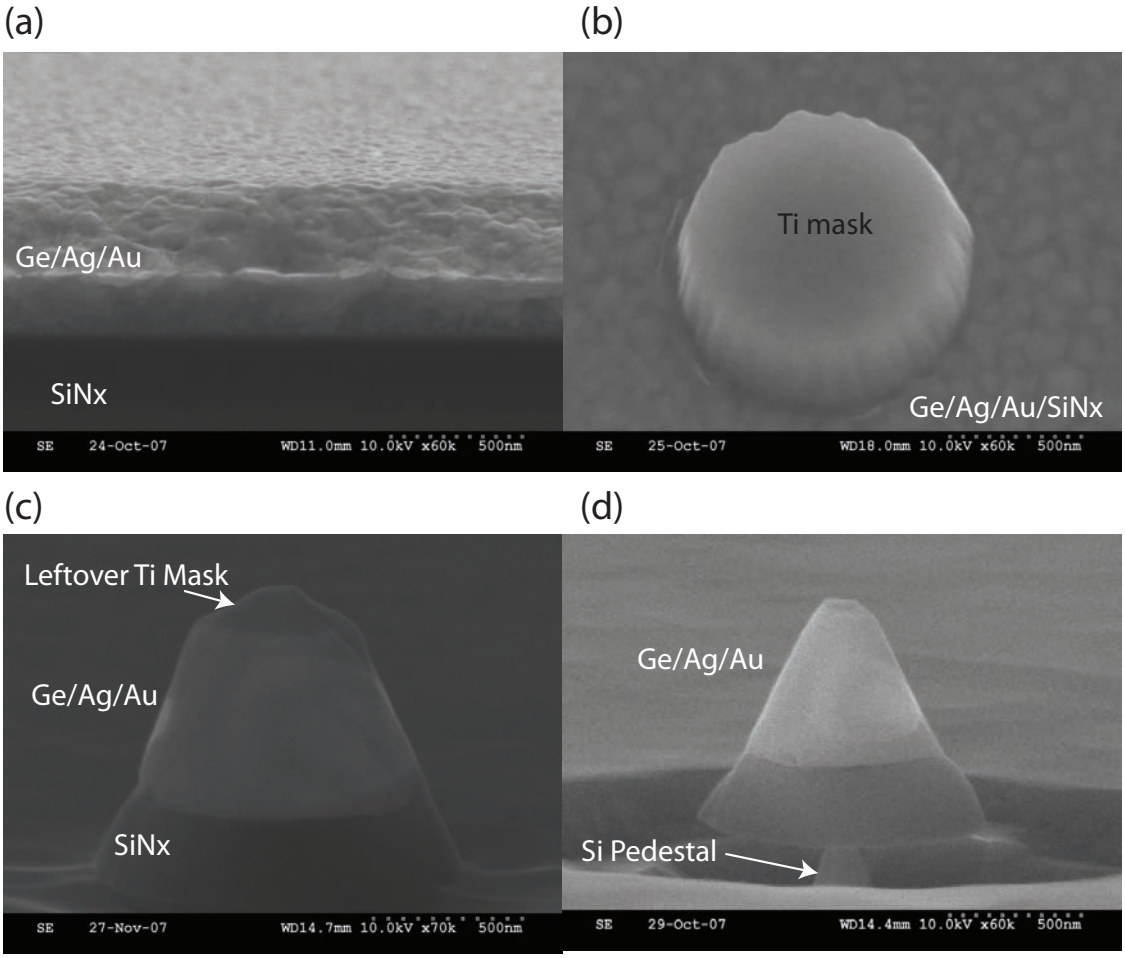

Figure 4.8: (a) Angled top view SEM micrograph Ge/Ag/Au contact layer on a slab of 250nm thick LPCVD SiNx on Si. Notch in the foreground is due to cleave. (b) SEM micrograph of Ti liftoff mask. (c) SEM micrograph Ar mill into Ge/Ag/Au contact. (c) Undercut of Si using KOH. Since Ag mill barely got through, only the region around the disk is getting undercut.

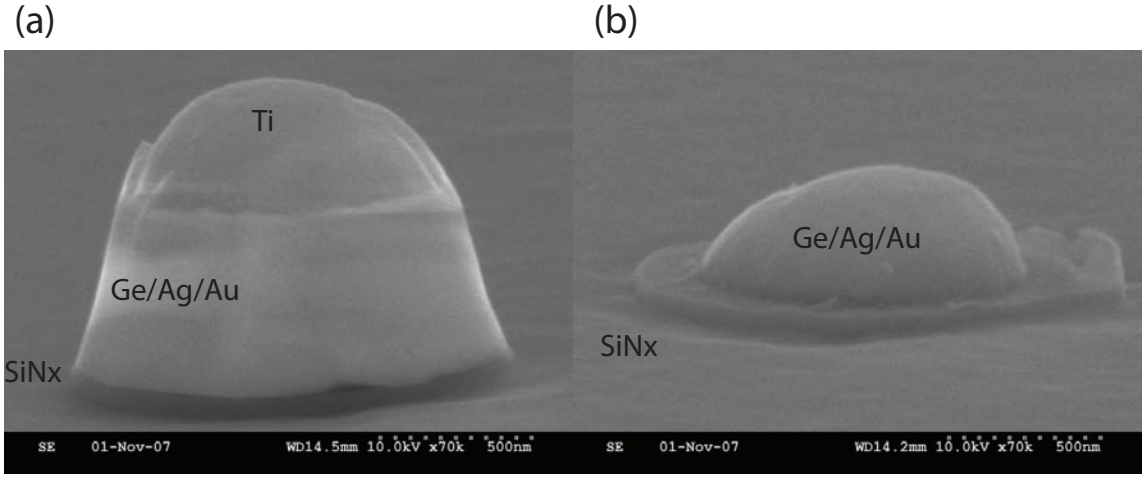

Figure 4.9: (a) Ar mill of Ge/Ag/Au contact. (b) Receded Ge/Ag/Au contact after KI:I_2 etch

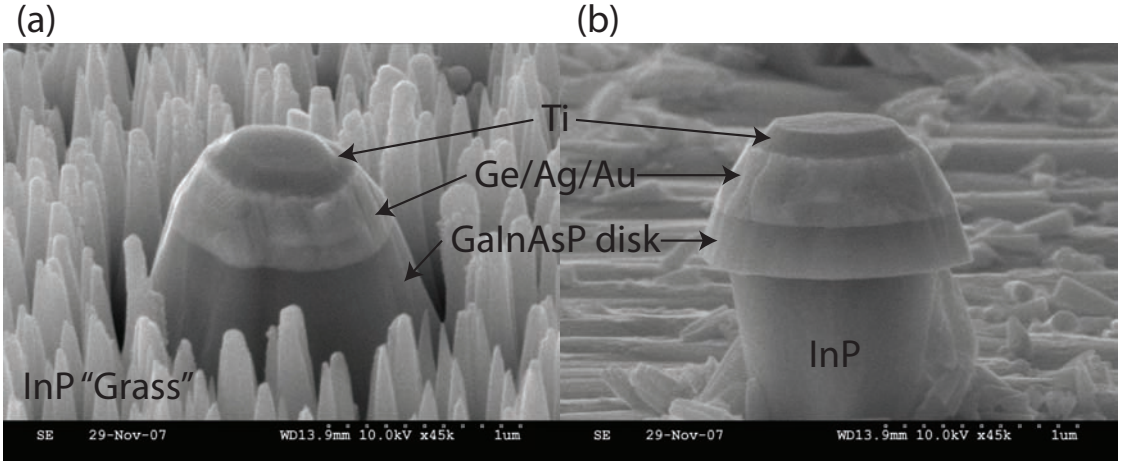

Figure 4.10: (a) Ar mill of Ge/Ag/Au contact on 1-QW material. (b) HCL based undercut.

Table 4.6: ICP/RIE – Oxygen Cytop etch

Parameter	Value Requested	Actual Value
RF	2W	(26/4W)
ICP	200W	(183/2W)
DC Bias		$\sim$ 114V
O_2	40sccm	(39.8sccm)
P_{ch}	20mTorr	(19.5mTorr)
P_{He}	-	-
T	20C	(23)
t	1min 15sec	

spin steps deposit 480, 840, and 910nm of Cytop. If there is any residue on sample's back it must be cleaned using CT-Solve (Asahi Glass Co.) otherwise it will be very difficult to remove later. The complete layer is then hard baked for 1hr and 15min at 200C in an oven.

In order to then expose the contacts on the very top of the disks, an oxygen ICP/RIE process was used (see table 4.6.) Cytop was etched away incrementally in two step with SEM imaging between. Using 30KeV imaging enabled us to look through some of the Cytop to see how close the surface was to the top of the disks. An SEM micrograph of the exposed tops of the contacts is shown in figure 4.11(a). At this point a Ti/Au 10nm/250nm is deposited via electron beam evaporation creating the air bridge contact as seen in figure 4.11(b).

In order to look at the final structure a cross section is created via focused ion beam (FIB) milling. A 500pA beam is used to created a regular cross section (stair case trench) and a 100pA beam is used for a cleaning cross section. The zoomed in SEM micrograph in figure 4.11(d) shows the details of the final structure: a small QW metal coated microdisk, buried in Cytop planarization layer, with an air bridge contact. The Cytop appears to have been partially removed by the FIB process. One could also envision this process with a polymer than can be dissolved away.

The use of the FIB as a cross-section tool also raised the possibility of using ion beam or electron beam assisted deposition of Platinum to create a receded metal contact. Several attempts were made using electron beam assisted deposition of Pt. at 30KeV with a beam current of 9.5nA. Electron beam assisted deposition was chosen over Ga-ion assisted deposition as very good center placement without semiconductor damage is necessary. By focusing the beam to 35x magnification and deposition Pt. for 2min "dunce cap" as high as 1.5μm can be formed. An example is shown in figure 4.12. As can be seen the Pt deposition looks extremely smooth. Further work would be

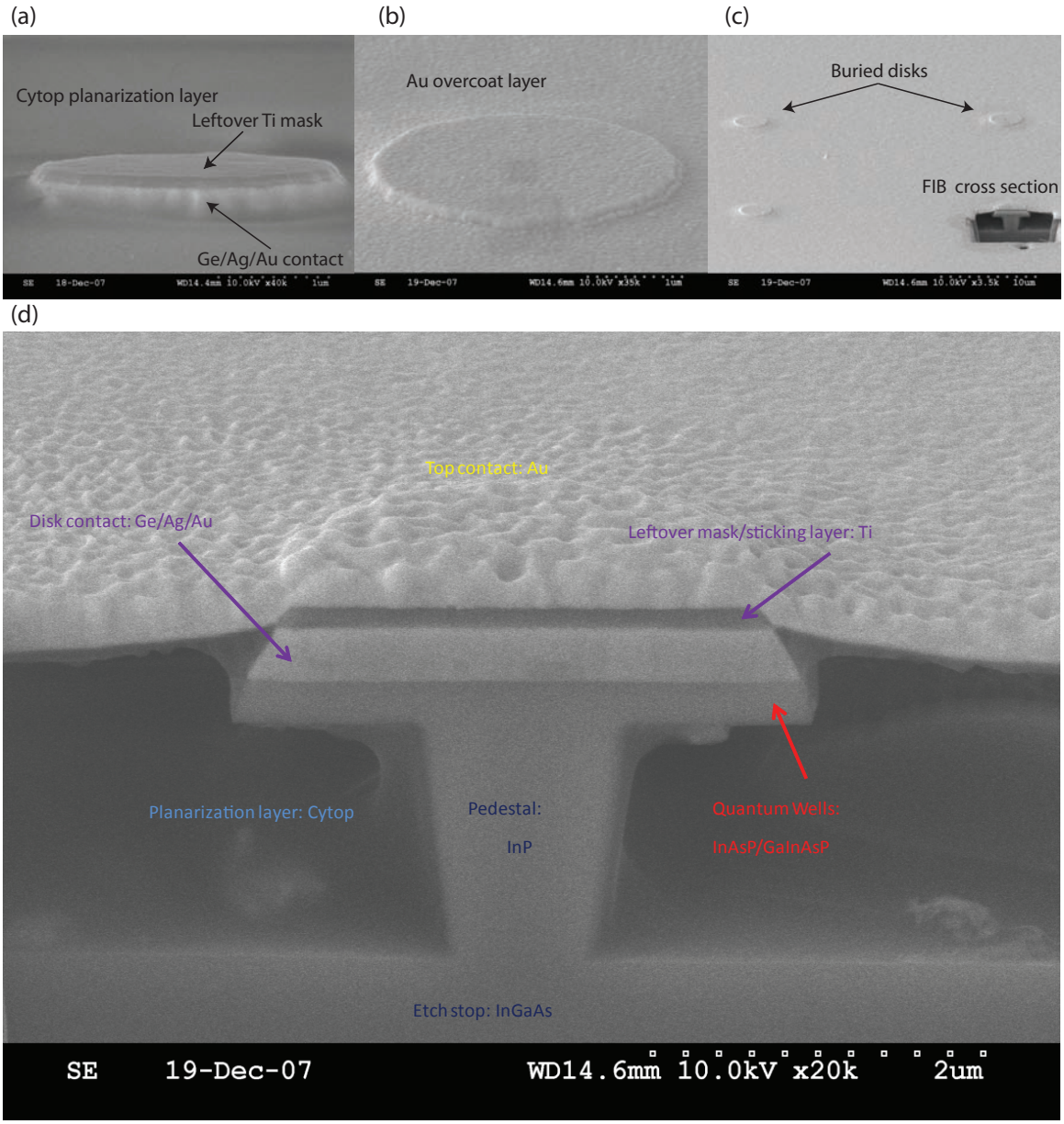

Figure 4.11: (a) Ge/Ag/Au with leftover Ti layer is buried in Cytop. Cytop is etched back using O_2 plasma so the very top is exposed. (b) A thick Au contact is then evaporated on top of the contact. (c) Focused Ion Beam (FIB) is used to show the structure below the surface. (d) A detailed view of the air bridge contacted 1-QW microdisk device.

needed to optimize the process. Currently a very thin layer of Pt seems to coat the disk. Interestingly the etch stop layers several microns below the disk appears to have significant Pt growth.

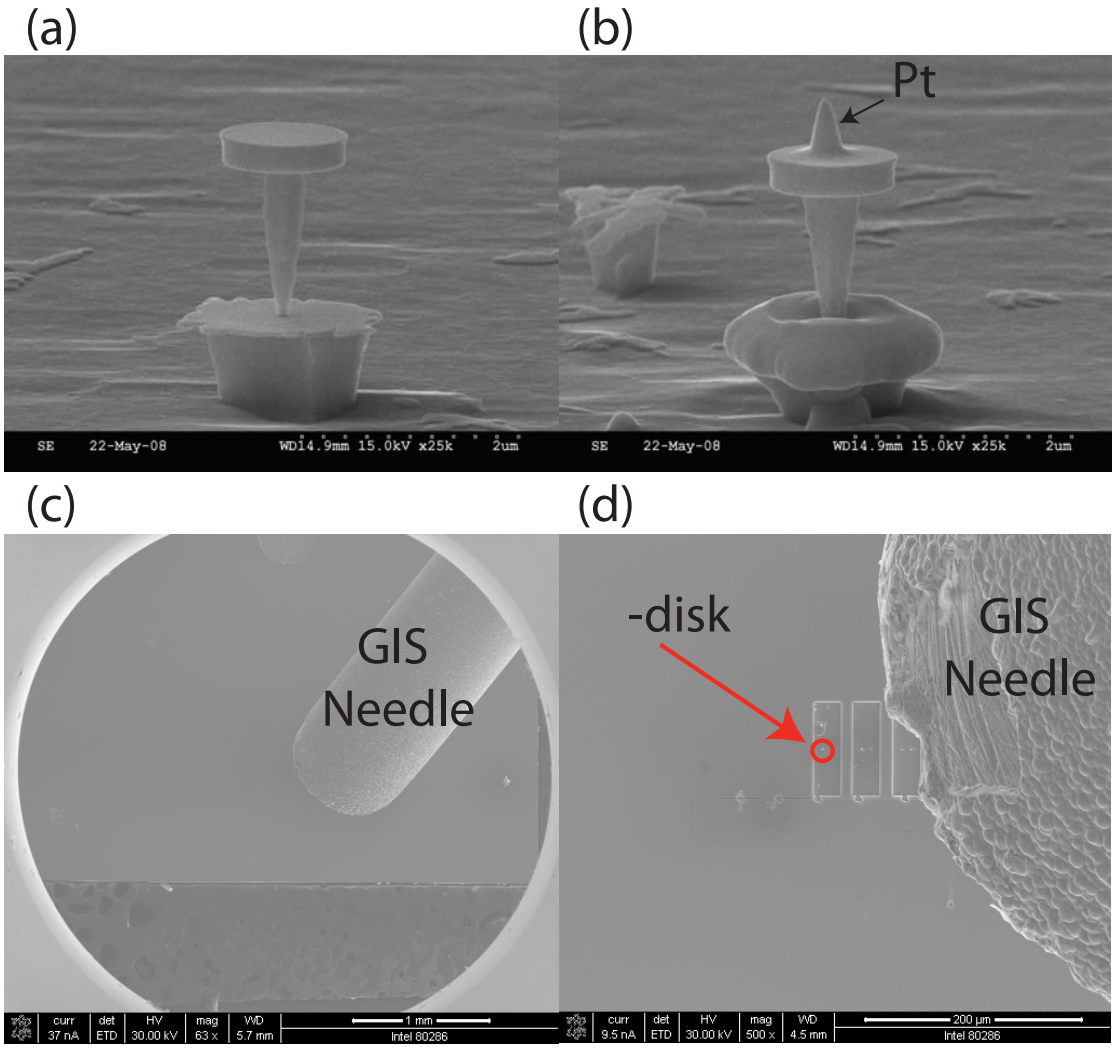

Figure 4.12: (a) Microdisk before Pt deposition (b) Microdisk after Pt Dunce cap deposition. (c) Zoom in of GIS needle. (d) Zoom out of GIS Needle.

4.3 Receded Metal Disks

In all of our attempts to make receded metal microdisks we have run into difficulties of properly receding the metal. The other obvious approach is to carry out dual aligned lithography, i.e., one lithographic step to define the metal contacts and a second aligned lithography to define microdisks. A significant effort was made to upgrade our SEM based lithography system to allow for aligned

beam writes. A new DAQ card was installed in our beam writing computer to accept the SEM's detector signal. Preexisting code was updated to reflect updated DAQ commands. The system is now able to acquire images by controlling the scan coils and accessing the detector signal. Using preexisting code, markers can be detected and coordinate transformation including displacement and rotation can be applied. Using this software, alignment can be achieved within $\sim 1\mu$m. Since we are shooting for sub-λ microdisks, better alignment must be achieved.

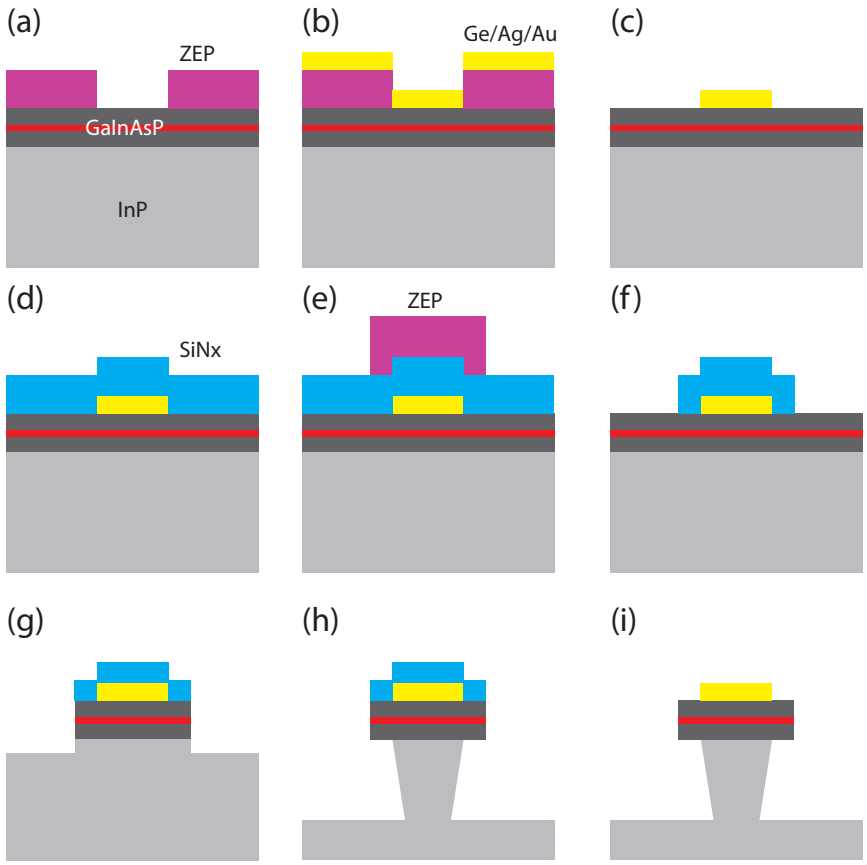

Figure 4.13: Fabrication flow of hybrid mode disks. (a) Liftoff mask is created via e-beam lithography. (b) Ge/Ag/Au is deposited via e-beam evaporation. (c) Liftoff. (d) Deposition of SiNx hard mask. (e) Microdisk e-beam lithography. (f) SiNx hard mask is etched. (g) GaInAsP microdisks are etched. (h) Microdisks are undercut via cold HCL solution. (i) SiNx is removed via plasma etching.

In order to carry out lithography with significantly better secondary alignment we switched to using the Leica 5000+ (Vistec) beam writer in the newly built Kavli Nanoscience Institute facility. There are several significant improvements associated with going to the beam writer, primarily a high-precision stage with interferometrically measured position and high-speed scan coils allowing for up to 50MHz write speeds. The accelerating voltage, 100KeV, of the beam writer is significantly

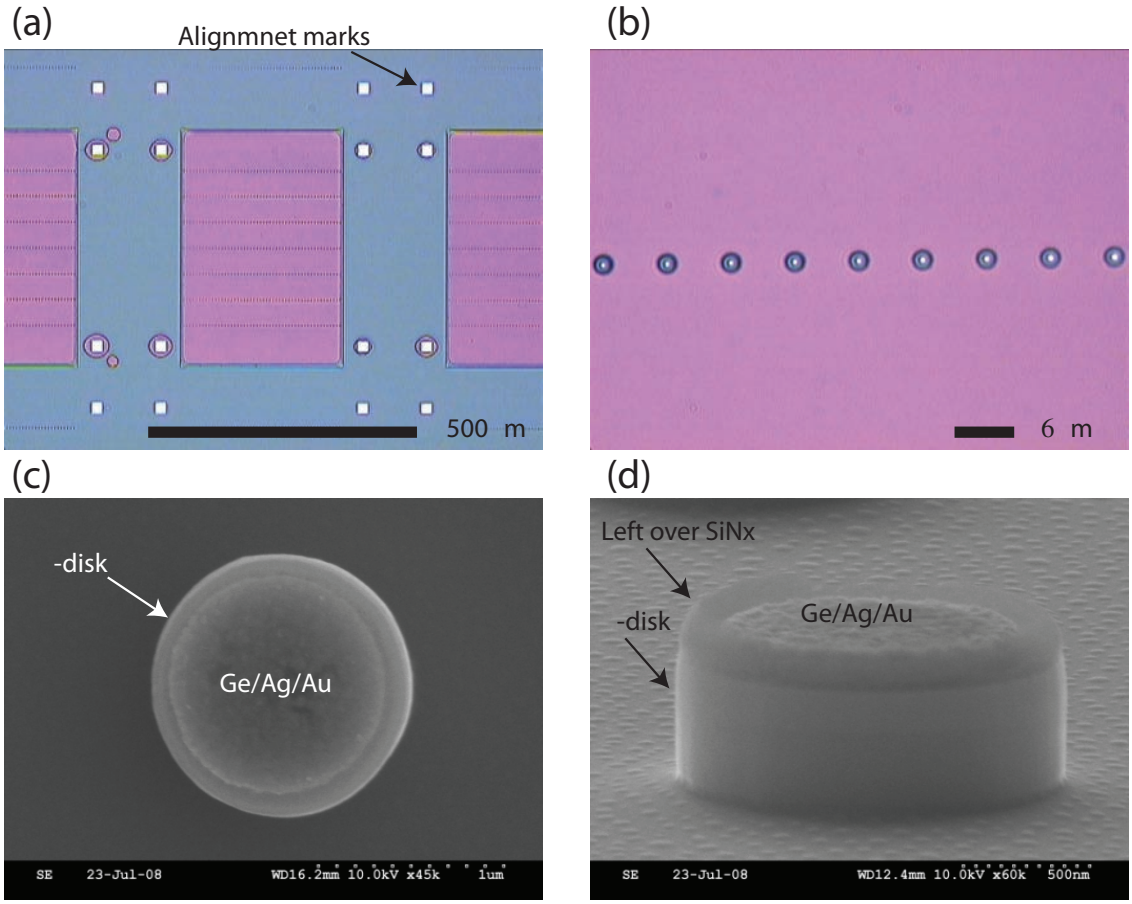

Figure 4.14: (a) Optical image of aligned electron beam lithography. Mask for 6x50 array of disks aligned on top of an array of systematically varied metal contacts (b) Zoom in showing fantastic alignment. (c) Top view of centered and aligned metal contact on top of a microdisk on practice material (d) Angled view of centered and aligned metal contact on top of a microdisk.

higher than the SEM, that is the only drawback of the beam writer. In the case of lithography on GaAs, and especially InP based materials, the high accelerating voltage leads to significant proximity effects. In the case of beam writing disks this can generally be mitigated by precise dose calibration. As will be seen later when more complex patterns are desired, a significant proximity correction routines or a lower acceleration voltage might have to be used.

Fabricated samples have multiple copies (dies) of the same layout, allowing for several tries at each processing step. Each die consists of 6 rows, each with different disk radius, and 50 columns with varying metal coverage for each disk size. A nominal disk radius of $R_d = 0.7\mu$m is chosen and varied from -15% to 15% across the rows. The metal radius is varied from 20% to 100%. As before, the process begins with the spin of ZEP 520A on C1280 material and a liftoff mask for metal is beam

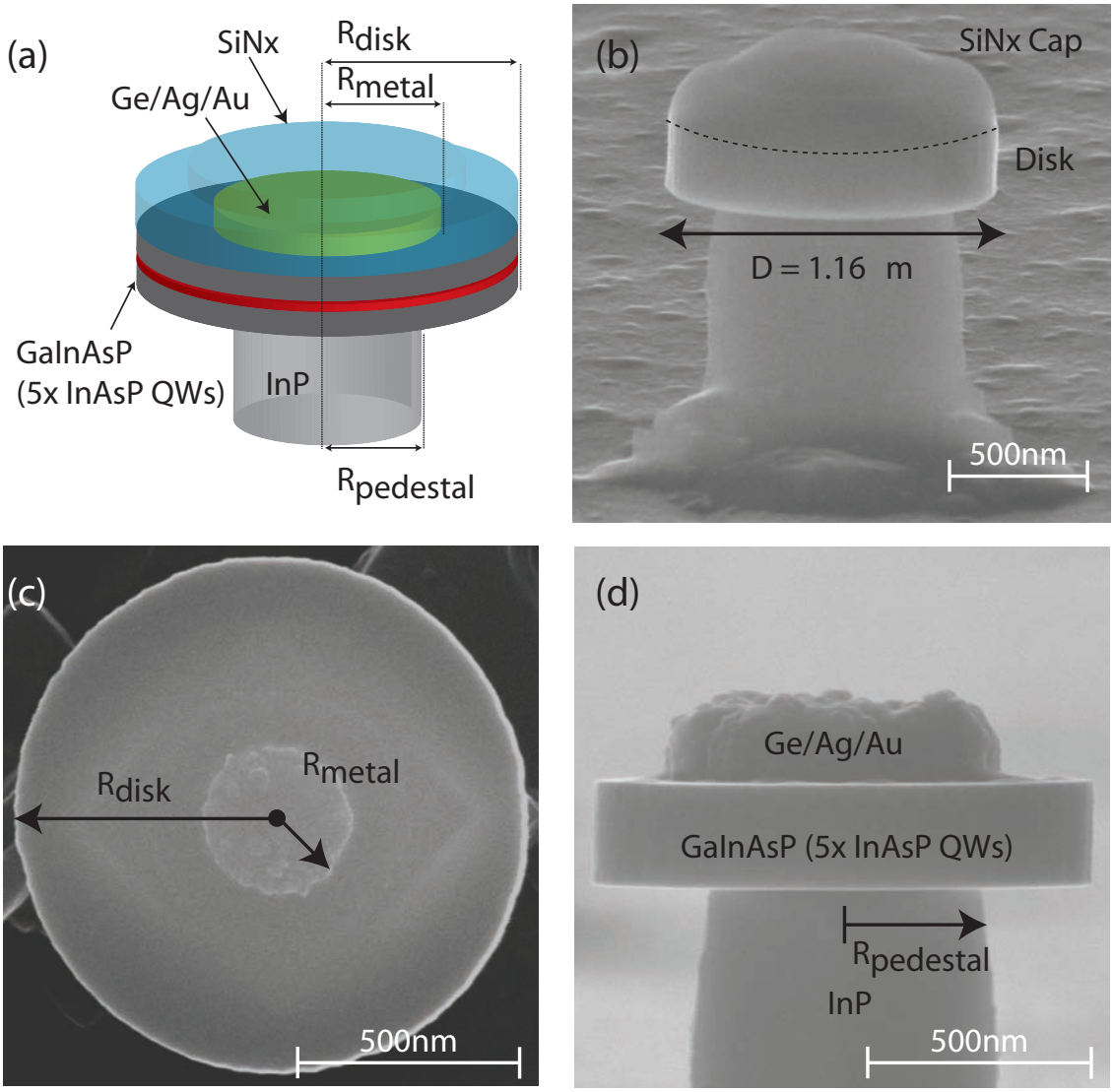

Figure 4.15: (a) Schematic of fabricated and simulated microdisks. (b) Scanning electron (SEM) micrograph of diameter $D = 1.16\mu$m fabricated microdisk with a Ge/Ag/Au $10/80/10$nm contact buried under a 150nm conformal layer of silicon nitride (SiNx). Dashed line delineates boundary between GaInAsP disk and SiNx cap. (c) SEM micrograph of top view of a microdisk after SiNx has been removed. (d) SEM micrograph cross-sectional view of a microdisk after SiNx cap has been removed.

written. Along with the metal contact pattern each die has four 20μm by 20μm square alignment marks. Dose calibration runs yielded an optimal dose of $D = 215\mu\text{Ccm}^{-2}$ at 100KeV using a 1.1nA beam. The sample is developed as usual and the Ge/Ag/Au 10/80/10nm contact layer is deposited via electron beam evaporation. Liftoff was carried out using trichloroethylene/acetone/isopropyl alcohol treatment. A 350nm SiNx hard mask is deposited via PECVD and ZEP 520A is again spun on the sample. A liftoff process without TCE is more gentle and prevent tearing of metal. A second beam write is then carried out at with dose of $88.5\mu\text{Ccm}^{-2}$ using the same 1.1nA beam. This beam write is carried out using "direct write" functions which allows for precise alignment of the disk pattern to the metal pattern. In order for this alignment to work the sample is first aligned on the stage holder within 1.5° relative to the stage axis, this can be either done by using a sample holder with a rotation stage or by hand. Once the layout is user defined as a square lattice with a unit cell of 4 alignment and metal contact pattern through software, the beam writer looks for the bottom left alignment mark in each cell and calculates a global transformation correcting for sample rotation and each individual cell location. The beam write then proceeds to each cell where all 4 alignment marks are detected. Then position, scale, rotation, and keystone corrections are carried out before the die is beam written. It should be noted that since the beam writer must detect a 100nm thick metal square buried under SiNx and resist the contrast parameter for the defined makers needs to be increased from 90% to 96% and in some cases the photomultiplier voltage (SEM detector) must be tweaked to get a good enough image to properly identify alignment marks. An optical image of a developed sample is shown in figure 4.14(a). The exposure around the alignment marks shows where the beam writer has detected them. The mask is reflown for 8min at 145C and as before the SiNx is etched via ICP/RIE for 7.5min. The ZEP is removed and the GaInAsP is etched via ICP/RIE for 1min and 35sec. As before the disks are then undercut in an HCL solution at 4C for a total of 45sec in two increments. SEM micrographs of one of many final devices are shown in figure 4.15(b).

After the data was collected, as is subsequently reported in chapter 5, the SiNx cap layer was removed allowing for SEM imaging and measurement of radius and centricity of the metal contacts (see figure 4.15(c) as well as pedestal radius (figure 4.15(d).) A summary of the geometrical parameter space achieved is shown in figure 4.16. A systematic variation of $25\% - 100\%$ metal coverage was achieved in disks with average diameter $D = 1.2\mu$m. A mild decreasing trend in disk diameter can be observed and is possibly related to the presence of the metal contacts during the disk lithography and etch. A more significant reduction of pedestal size trend is also seen. Such a

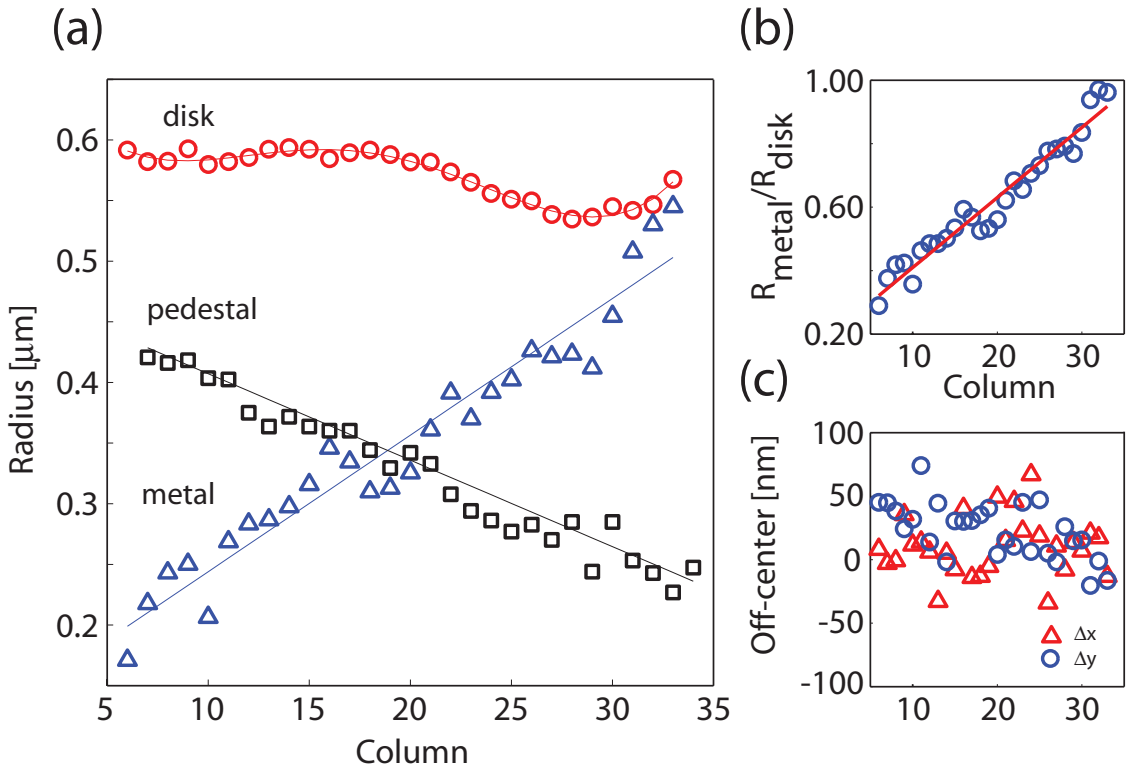

Figure 4.16: Geometric parameter space of devices fabricated and measured. (a) Disk radius, metal radius, and pedestal radius are plotted as a function of lithography column number. Linear fits for pedestal and metal radius as well as a 4th-order fit for the disk radius are also plotted. Fits are subsequently used to model the devices. (b) Plot of metal radial fraction (R_m/R_d) as a function of column number. (c) Plot of degree of centricity of Ge/Au/Ag $10/80/10$nm contact on top of disk in both x ($\sigma_x = 23.4$nm), y ($\sigma_y = 21.7$nm) directions as a function of column number.

trend can be attributed to the orientation of the sample in the undercut bath.

Chapter 5

Hybrid-mode Lasers–Testing and Analysis

Once fabricated, microdisks with metal contacts are tested optically. The experimental setup is described in section 5.1. Testing is divided into distinct modes. First disks are probed for hybridization behavior as described in section 5.2 and compared with simulations in section 5.3. Next, devices are tested for laser action as described in section 5.4 and both threshold and line width data is analyzed in section 5.5. It is important to note that devices are first tested. Only then is the nitride removed and the devices are imaged using the SEM to get accurate geometric parameters such as metal radius (R_m), disk radius (R_d), and pedestal radius (R_p). This is done for fear that metal damage due to nitride removal, as well as possible carbon deposition due to SEM imaging or other effects, would either damage or otherwise affect the microdisks. Data is therefore plotted as a function of parameters measured post measurements. Testing of these devices was carried out in collaboration with T. Alegre.

5.1 Experimental Setup

The test setup for probing hybridization and lasing is shown in figure 5.1. The test setup allows for both free-space and dimpled fiber taper based pump and probe. Testing is divided into two distinct modes. The first is the mapping out of resonant modes using dimpled fiber taper collection. A detailed description of dimpled fiber testing and fabrication is found in reference [79]. The second is the probing of the devices for lasing action with free-space collection. In both cases the devices were free-space pumped. The test setup will first be discussed in general and then mode specific details will be provided.

The sample containing several dies of 350 disks (7 rows, 50 columns) is placed in a liquid helium flow cryostat. The ability to cool the sample was not used in these measurements but could be in future experiments. The cryostat sits on a large XYZ mount (Parker) where Z is in the axis of the pump/collect microscope objective. Inside the cryostat the sample sits on a stack of X and Z slip-stick piezo stages (Attocube). A dimpled fiber taper that is fed through a port in the cryostat is mounted on a Y stage (where Y is the direction along the taper) as well as a fine XYZ piezo stage. The fiber can be tip/tilted using a custom-made mount so it is parallel to the sample surface. This sample positioning configuration allows for both free-space pump and photoluminescence collection using the large XYZ stage as well as fine positioning using the cryostat-internal stages. As well as fiber taper based probing and light collection using the fine cryostat-internal stages. The PL setup was originally built by Srinivasan and Painter. The details of the cryostat setup can be found in reference [80]. The setup had to be re-setup and aligned after the lab was moved from Steele to Watson Labs. An additional fiber taper tip-tilt stage was machined to allow for easier leveling of the fiber taper relative to the sample stage.

The microdisks are pumped using a home built external cavity diode laser (ECDL) using an 830nm diode. In most measurements the laser diode is electrically pumped using a pulsed voltage source (HP8114A). Temperature is regulated with a temperature controller (ILX lightwave). The laser is fiber coupled and the light is piped across the table where it is coupled back into free-space. The beam is steered through a 50/50 beam splitter. Half of the pump beam is sent to a power meter (Newport) and the other half directed down into the backside of 20x (NA$=$ 0.24) long working distance infinity corrected objective lense. The sample and the pump spot can be imaged by a CCD camera and a lens tube with a fiber bundle light source. Either imaging or data collection can be carried out at one time, depending on the position of a flip mirror.

Photoluminescence is collected either free-space through the objective or through the evanescently coupled fiber taper. If light is collected free-space, it is collected by the objective and is then routed using free-space optics either to a spectrometer (Jobin-Yvon) or coupled into a multi-mode fiber and sent to an optical spectrum analyzer (OSA.) If light is collected via evanescent coupling with the dimpled fiber taper, it is then either detected on the OSA or free-space coupled to the spectrometer. The method of light collection is chosen and optimized for particular measurements.

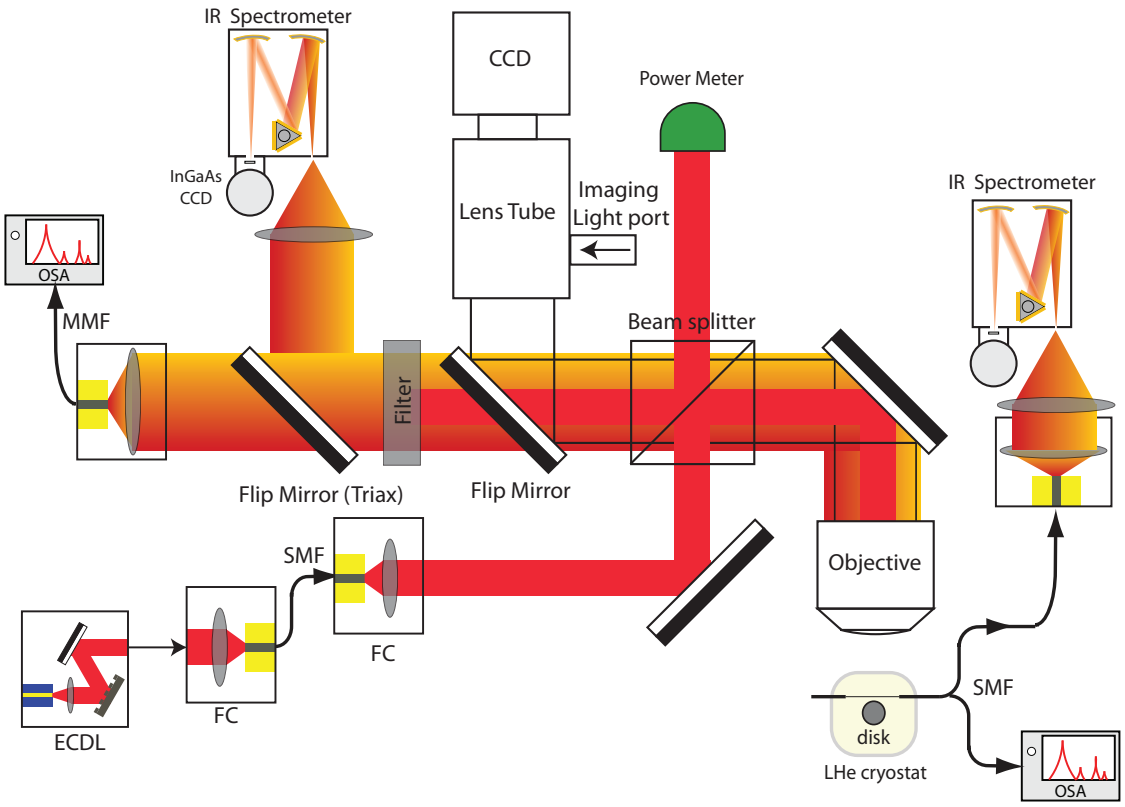

Figure 5.1: Photoluminescence test setup. Schematic shows a combination of configurations allowing for both free-space and fiber taper collection.

5.2 Anticrossing: experimental

Since the goal of this experiment is to both observe hybridization and observe lasing in small hybridized disks we first locate the smallest disk size (i.e., row) where the modes fall within the gain bandwidth of the material. For starters, we focus the pump beam onto the surface and collect free-space through the objective lense. Light is coupled into a multimode fiber and sent to the OSA. This allows for quick and efficient PL collection. Then we choose a column with small metal radius and test each row. We choose column 4 as it should have very little metal if any but is not at too close to the edge of the pattern for lithography edge effects to be present. PL data is plotted as a function of row number, i.e., disk size in figure 5.3 for two different pump powers as measured on the Newport detector. We see three sets of modes tuning across the background PL. As can be predicted, as disk size decreases, mode with the same m-number decrease in wavelength. Since in semiconductor lasers the peak of the gain spectrum is red of the peak of the PL, we choose row 6. It is the row with the smallest size disks which are most likely to be centered in the gain spectrum of

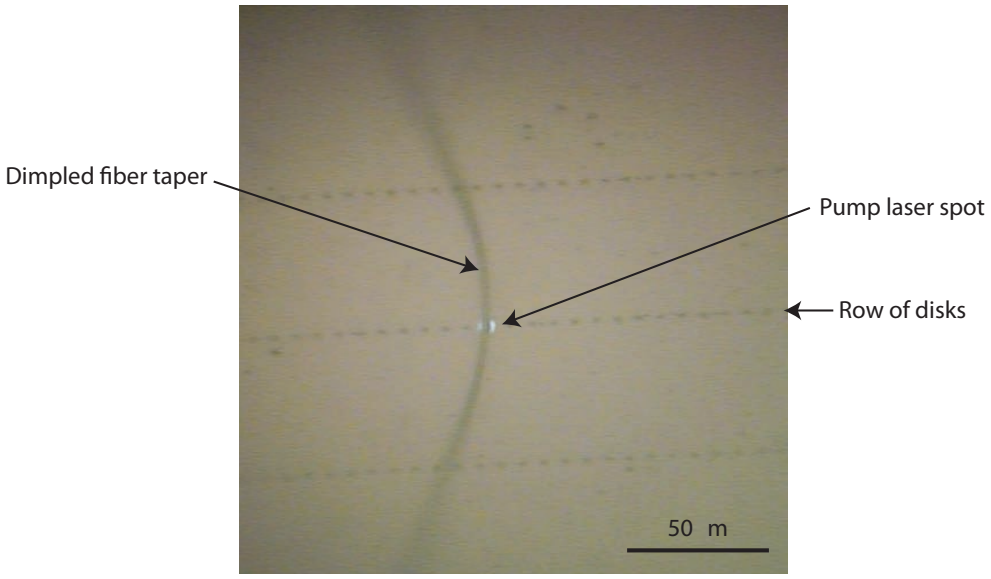

Figure 5.2: Optical image of a dimpled fiber taper coupled and optically pumped partially metal coated microdisk.

the laser material. From subsequent SEM measurements of the geometry the radius is $R_d \sim 1.2\mu$m.

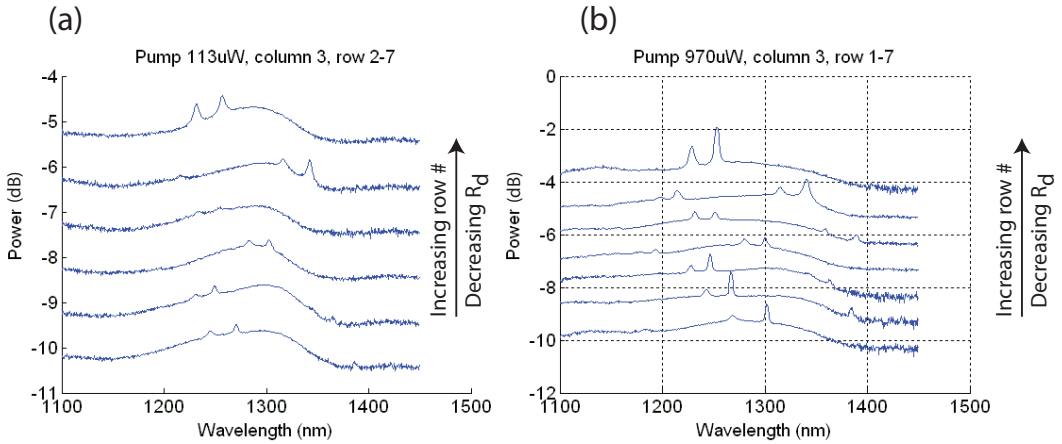

Figure 5.3: Normalized fee space collected spectra from column 3 plotted on a log scale as function of row, i.e., disk size. (a) Low power. (b) High power.

In order to observe resonant modes well into the hybridization region it is clear from figure 5.3 that background PL must be suppressed if there is to be any chance of seeing low Q modes. In order to do this, instead of collecting free-space, the spectra is collected by evanescent coupling of the disk modes to a the dimpled fiber taper probe. A dimpled fiber taper coupled to a microdisk with the pump laser beam on can be seen in figure 5.2. The ability to collect light from the disks via

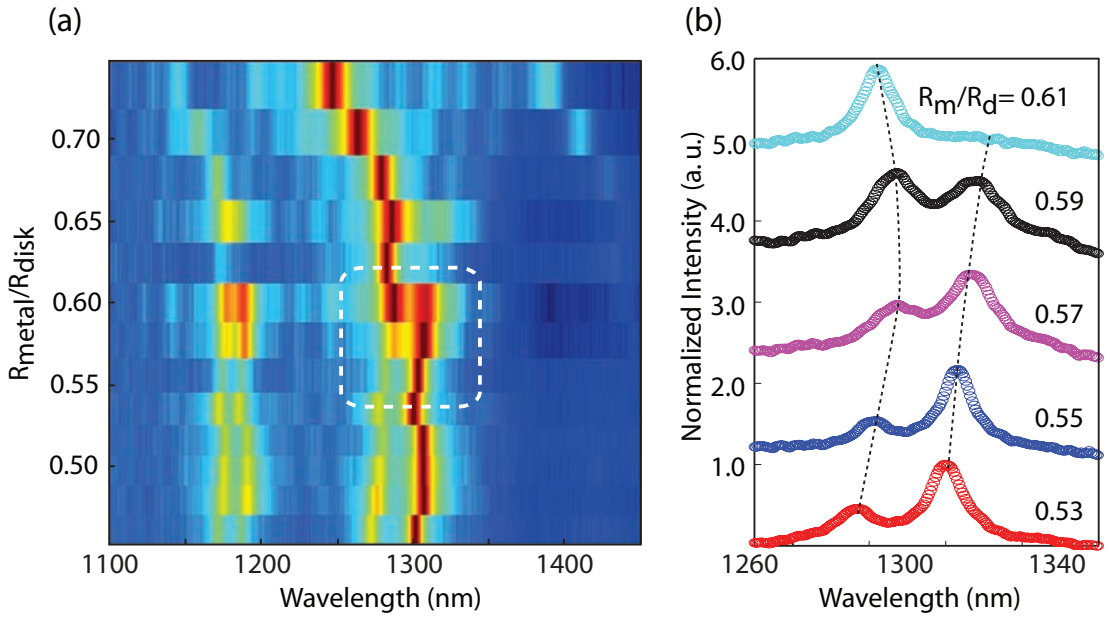

Figure 5.4: (a) Fiber taper collected normalized spectra on a log scale as a function of R_m/R_d. Free-space pumping condition: pump power $P_{pump} = 1$mW, pulse width $\Delta T = 500$ns, period $T = 1\mu$s. (b) Zoom in of anticrossing region. Dashed lines are guides to the eye

a dimpled fiber taper is very advantageous as it filters out background PL. Only light in resonant cavity modes will couple effectively to the taper. Testing is carried out by gently approaching the disk edge from the top and side until the fiber makes contact. While one can couple effectively to modes with the fiber just nearly touching, touching the disk provides a significantly increased stability and reduction in noise due to fiber vibration over long integration times.

Spectra are collected for every single column across row 6. Free-space pumping condition used are: pump power $P_{pump} = 1$mW, pulse width $\Delta T = 500$ns, period $T = 1\mu$s. Log normalized fiber collected spectra as a function of R_m/R_d are plotted in figure 5.4(a). Two sets of modes can be seen one around $\lambda \sim 1.3$ and the other around $\lambda \sim 1.2$. In the longer wavelength set, the more intense mode is the longer wavelength mode. As the anticrossing region is approached, the lower wavelength modes becomes more intense, while the longer wavelength mode moves even longer and looses intensity very quickly. The spectra exhibit an anti-crossing characteristic in wavelength consistent with simulations.

The line width of both long wavelength modes is plotted in figure 5.5(a). The blue mode of the pair decreases in line width, consistent with an increase in Q, and the red mode of the pair quickly increases, that is consistent with a decrease in Q. Direct comparison to simulation of Q

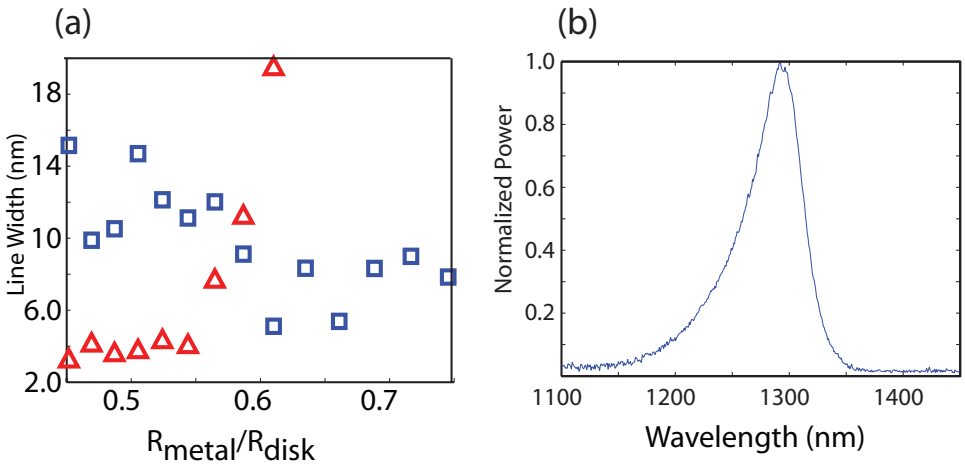

Figure 5.5: (a) Line width fits of mode pair at $\lambda_0 \sim 1300$nm. Triangles denote the longer wavelength modes (red), square denote the longer wavelength modes (blue). (b) free-space collected, continuous wave pump, photoluminescence (PL) of unpatterned laser material, $P_{pump} = 282\mu$W.

is complicated by several other sources of spectral broadening of the modes: variable pumping due to change in metal coverage and spectral shift away from the gain spectrum. Nevertheless, a qualitative comparison is possible. A normalized photoluminescence spectrum is shown in figure 5.5(b) for reference.

5.3 Anticrossing: analysis

In order to compare observed anti-crossing behavior with simulations, a set of more experimentally faithful microdisks including SiNx, pedestal, and substrate were carried out. Geometry parameters were measured after the SiNx was removed. A summary of geometric parameter space achieved is shown in figure 4.16(a). A systematic variation of $25\% - 100\%$ metal coverage was achieved in disks with average diameter $D = 1.2\mu$m. A mild decreasing trend in disk diameter can be observed and is possibly related to the presence of the metal contacts during the disk lithography and etch. A more significant reduction of pedestal size trend is also seen. Such a trend can be attributed to the orientation of the sample in the undercut bath. Both $m = 6$ and $m = 7$ mode pairs are simulated and shown in figure 5.6(b). The wavelength behavior of the modes qualitatively matches the experimental data. The waist of the hybridization is predicted for the longer wavelength set of modes to be at $R_m/R_d = 0.45$ at $\lambda_0 = 1295$nm. The difference in R_m/R_d may be possibly attributed to damage of the Ge/Ag/Au contact during the SiNx removal, deviation of dielectric constants of the

metal contact and active material from values from literature, as well as imprecision in modeling the SiNx conformal layer. From the simulations it is determined that the second set of modes observed at shorter wavelengths that also exhibit anti-crossing behavior are modes with higher azimuthal number $m = 7$.

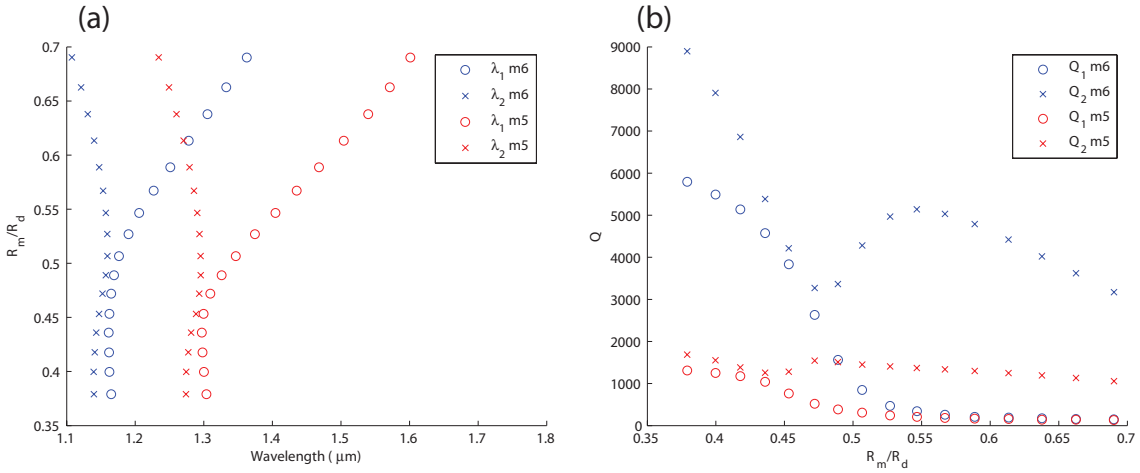

Figure 5.6: FEM simulations of full structure including 150nm of leftover SiNx and using fits from figure 4.16: (a) R_m/R_d vs. wavelength (b) Q vs. R_m/R_a.

If one looks carefully at these full structure simulations the Q behavior reveals a problem. Mode I, that in initial simulations was purely TE with a Q higher than that of its TM counterpart mode II, now appears to have a lower Q. This is inconsistent with the data, as the long wavelength mode has a higher intensity before the anticrossing, at which point the situation reverses and the shorter wavelength mode becomes more intense. What is occurring here is the polarization character of these modes is flipped. In initial simulations, as is typical, the TE mode is higher Q and longer wavelength than the corresponding TM mode of the same m number. As the disk is shrunk, one possibility is that this vertically asymmetric dielectric structure, including the pedestal and SiNx, allows for the TM mode to be the longer wavelength modes. This is due to the decreasing confinement. The mode is pushed out of the disk and in the case of the TM mode into the SiNx and pedestal increasing it's effective index relative to the TE mode that is pushed out radially into the air. To confirm that this may be the case, one can gradually increase the index of the disk and observe both Q and wavelength. As can be seen in figure 5.7 when the refractive index is increased to between 3.6 and 3.7 the modes become properly ordered.

In an attempt to try to separate the effect of the SiNx from the pedestal another set of simulations

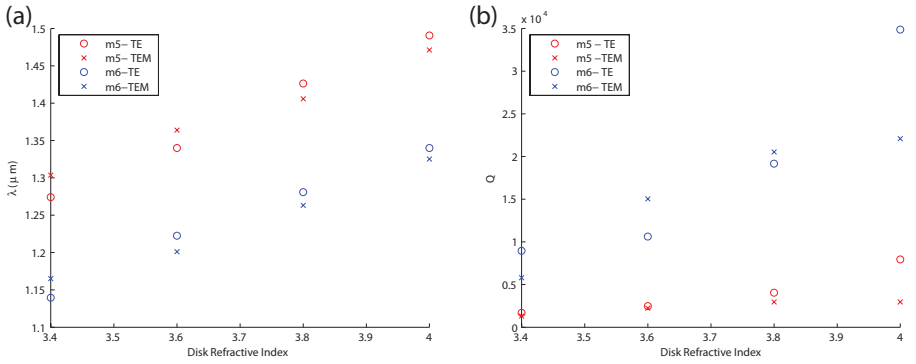

Figure 5.7: Simulations including pedestal, SiNx, and Ag ($R_d = 0.583\mu$m, $R_m = 0.221\mu$m, $Rp = 0.414mu$m): (a) Wavelength vs disk index of refraction (b) Q vs disk index of refraction

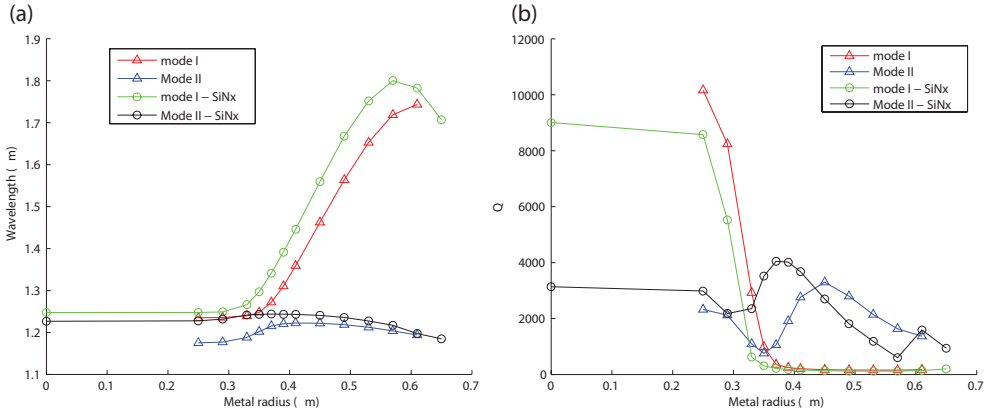

Figure 5.8: Comparison of original simulations (figure 3.3)with constant $R_d = 0.65\mu$m with and without SiNx. (a) Wavelength vs. R_m/R_d (b) Q vs R_m/R_d

was carried out. The original simulations from figure 3.3 with constant $R_d = 0.65\mu$m were repeated with the SiNx overcoat. Plotted together, simulation with SiNx shows that for at least for $R_d = 0.65\mu$m disks the modes are only slightly affected by the SiNx and the remain ordered in the same way. A simulation set that is perfectly matched to the data would most likely need to include a model for the refractive index of the active material and pedestal as a function of wavelength. We will leave this analysis to a later date.

5.4 Lasing: experimental

Disks were tested for lasing characteristics to see how far into the hybridization region lasing can be achieved. The devices were optically pumped free-space and light was collected free-space to

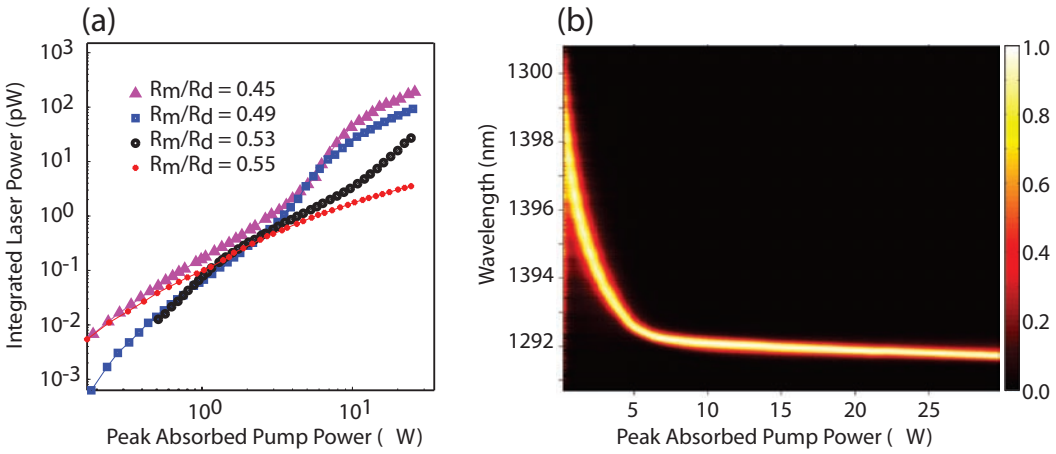

Figure 5.9: (a) Light-light curves of several devices of increasing R_m/R_d are plotted on a log-log scale. Disks with $R_m/R_d < 0.53$ exhibit a clear "S" shape indicating lasing. Disk with $R_m/R_d = 0.53$ is a borderline case, and finally the disk $R_m/R_d = 0.55$ does not lase at all. (b) Normalized spectra for a device with $R_m/R_d = 0.42$ are plotted as a function peak absorbed pump power.

a spectrometer. To minimize thermal effects on line width and threshold the disks were pumped with low duty cycle pulses ($\Delta T = 20$ns,$T = 4\mu$s). Lasing action was achieved in several weakly hybridized sub-wavelength microdisks. Threshold curves for a series of disks are shown in 5.9(a) with increasing R_m/R_d. Peak absorbed pump power was estimated based on a pump spot size of diameter $D = 2\mu m$, pump absorption efficiency of $\eta = 10\%$, and accounting for the pump duty cycle. Output power is integrated over the laser spectra. Disks with $R_m/R_d < 0.53$ exhibit a clear "S" shaped logarithmic light-light (LL) curves indicating lasing. The disk with $R_m/R_d = 0.53$ exhibits weak lasing behavior. The best lasing device is a microdisk with $R_m/R_d = 0.42$ with a threshold peak absorbed pump power of $P = 5\mu$W. It is more difficult to plot threshold power vs. R_m/R_d as its hard to truly calibrate the pump power due to the metal contacts. Spectra as a function of peak absorbed pump power are plotted in figure 5.9(b). An $\sim$ 8nm blue shift is seen in the center wavelength from PL to lasing, most likely attributed to free carrier loss, as the shift stabilizes with gain clamping [81, 82].

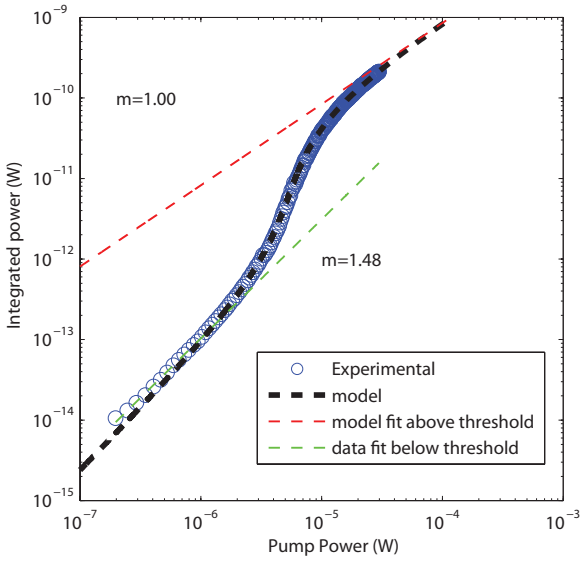

Figure 5.10: Log-log plot of data from a laser device with $R_m/R_d = 0.42$. Rate equation model including non-linear surface recombination term is fit to the data.

5.5 Lasing: analysis

5.5.1 Threshold behavior

Due to the small size of these optical cavities and the limited number of modes seen below threshold, one would expect that the fraction of spontaneous emission going into the lasing mode (β) may be quite large for these lasers. Laser rate equation analysis can be found in many sources, for example a text by Coldren and Corzine [25], a text by Agrawal and Dutta [83], as well as papers by Yamamoto [84]. When it comes to the definition of spontaneous emission included in the rate equation for cavity photon number, there is a bit of an inconsistency between Yamamoto and Agrawal. Yamamoto constrains the rate of spontaneous emission into the lasing mode to be the differential gain when the mean photon number in the cavity is one, while Agrawal does not. For the purpose of our simple analysis, we will not include modification of the spontaneous emission rate by the cavity geometry and the rate of spontaneous emission emitted into the lasing mode will be treated independently of differential gain. Further modeling may be needed to capture the complete physics of the system. Hopefully such a simple analysis will give us a feeling for the importance of recombination processes in small semiconductor lasers where the surface-to-volume ratio is very high. In figure 5.10 the threshold curve of device number 10 with $R_m/R_d = 0.42$ is plotted. Typically such a light-light (LL) curve can be fit by using a simple rate equation model at steady state. The rate

of change of the carrier number (N) is equal the injected carriers ($N_{injected}$), minus a recombination rate including spontaneous emission and nonradiative recombination (γ_e), minus the carriers that take part in stimulated emission:

$$\frac{dN}{dt} = N_{injected} - \gamma_e N - GP. \tag{5.1}$$

The rate of change of the photon number (P) is linear with laser gain (G) minus cavity loss (γ), plus spontaneous emission into the lasing mode.

$$\frac{dP}{dt} = (G - \gamma) + R_{sp} \tag{5.2}$$

Gain is modeled as linear gain:

$$G = \Gamma v_g (a/V)(N - N_0). \tag{5.3}$$

In the expressions above $a = 2.5 \times 10^{-16}\text{cm}^2$ is the gain coefficient and $N_0/V = 1 \times 10^{18}\text{cm}^{-3}$ is the transparency value of the carrier density for a typical buried heterostructure laser at $\lambda = 1.3\mu$m from reference [83]. From FEM simulations, a mode volume of one cubic wavelength in the material is used. The group velocity, $v_g = c/n_g$, uses the simulated effective index $n_g = 1.8$. Cavity loss is $\gamma = v_g \alpha_{cavity}$ where $\alpha_{cavity} = \omega/(Qv_g)$. Q of 1.4×10^3 is also from FEM simulations. Γ is the overlap with the active region and is estimated to be the combined thickness of the five QW layers divided by the total epitaxy thickness. The rate of spontaneous emission going into the cavity mode is

$$R_{sp} = \beta \eta_{sp} \gamma_e N, \tag{5.4}$$

where $\eta_{sp} = Bn/\gamma_e$ is the fraction or recombination that leads to photon emission and γ_e is the total carrier recombination rate:

$$\gamma_e = (A + Bn + Cn^2) = \frac{1}{\tau}. \tag{5.5}$$

The total recombination rate includes three mechanisms for recombination. Recombination due to trap states ($A = 1 \times 10^8\text{s}^{-1}$) which is linear with carrier number. Radiative recombination due to spontaneous emission goes as N^2 ($B = 1 \times 10^{-10}\text{cm}^3\text{s}^{-1}$):an electron and a hole. As well as an Auger recombination term ($C = 3 \times 10^{-29}\text{cm}^6\text{s}^{-1}$ that goes as N^3: a combination of electrons and

holes. Recombination coefficients are from reference [83]. The rate of spontaneous emission into the cavity mode is therefore:

$$R_{sp} = \beta BnN. \tag{5.6}$$

The observed below threshold slope of the light-light curve of $m = 1.45$ (figure 5.10) can not be simply fit from the above rate equation model. As was shown in reference [85] for slightly larger microdisks, due to the very large surface to volume ratio in these tiny cavities, as well as the proximity of the optical modes to the periphery of the disk, there can be a significant surface recombination term that must be included to properly fit the below threshold data. It can be seen from the rate equations below threshold, where N and P are small, that if a surface recombination term $A_{sr}N^x$ is added to the total recombination rate, the slope of the threshold curve is $m = 2/(x+1)$. Our data is fit using a surface recombination term with $x = 0.35$. The spontaneous emission is assumed to be evenly split among four modes ($\beta = 0.25$) and the A_{sr} term is varied to get a proper fit to the data. The coupling of pump light into the cavity and outcoupling from the cavity are treated as free parameters as the fee space coupling efficiencies are not calibrated. From A_{sr} one can calculate a surface recombination velocity taking into account the surface area of the QW layers exposed at the periphery and the pumped volume. A surface recombination velocity $v_{sr} = 1.3 \times 10^3$cm/s is extracted from the fit. This is a reasonable number as compared to InP based active materials [25].

It is important to note surface recombination plays a significant role in small cavities where the surface area to volume is significantly increased. When analyzing data in order to fit a β parameter it is important to realize that an increase in surface recombination would flatten the "S" shape threshold curve just as a high β laser would. The physical mechanism for a super linear surface recombination term is not fully understood. In the case of reference [85] the active material is comprised of quantum dots and such processes could be associated with carrier localization [86]. It is interesting to see that such behaviour occurs in QW lasers. This remains to be understood.

5.5.2 Line width

The line width behaviour of this device is also interesting. Data is shown in figure 5.11. As integrated output power is increases, the line width narrows. The line width then increases briefly, before narrowing again more quickly. Laser noise and line width phenomena have been of great interest for as long as lasers and masers have been around. Seminal work by Schawlow and Townes

predicted laser line width below threshold to be lorenzian and inversely proportional to laser power [87] maintaining a constant $\Delta\nu P_0$ [59]. Above threshold it was predicted by Lax that [88, 89] the product $\Delta\nu P_0$ is reduced by a half. This above threshold line width is commonly referred to as the modified Schawlow-Townes line width. With the development of semiconductor lasers, a correction term $(1+\alpha^2)$, "line width enhancement factor", was introduced by Henry [90] and Vahala and Yariv [63]. Where α is the amplitude-phase coupling of the laser oscillator or the ratio between fluctuations in the imaginary part of the semiconductor refractive index to the fluctuations in the real part of the refractive index $\alpha = \Delta n_{real}/\Delta n_{imag}$. Physically, the fluctuation in the imaginary part of the refractive index due to spontaneous emission related carrier fluctuations, lead to frequency fluctuations in the output spectrum through the real part of the refractive index. As β increases, the amount of spontaneous emission could lead to more significant line width broadening around threshold, though this point is debated in the literature. Soon after, α was measured for a buried optical guide laser [91]. Measurements of laser line width in small $D = 2.2\mu$m in InGaAs QW microdisks at $\lambda = 1.55\mu$m were carried out by Slusher et al [61] but they propose that further theoretical study is necessary for fully understand observed line width behavior.

In this section, a very preliminary analysis of laser line width of device 10 is carried out. A typical process for solving for frequency noise or phase noise can be found in several sources: [83, 59, 84, 25]. The rate equation analysis will stay consistent with equations in section 5.5.1 and line width analysis relies on reference [62]. I will very briefly outline the analysis and then just use the stated result.

Typically Langevin noise terms are introduced to the rate equations for photon number (P), carrier number (N), and phase (ϕ):

$$\frac{dN}{dt} = I/q - \gamma_e N - G_p + F_N(t) \tag{5.7}$$

$$\frac{dP}{dt} = (G-\gamma) + R_{sp} + F_P(t) \tag{5.8}$$

$$\frac{d\phi}{dt} = -(\omega_0 - \omega_{th}) + \frac{1}{2}\alpha(G-\gamma) + F_\phi(T) \tag{5.9}$$

It is assumed that the noise terms are Markovian, meaning the noise correlations are much faster in time scale than either the cavity photon decay or the recombination rate (γ_e). Such an assumption

leads to previously derived correlations among noise terms [59, 88, 89]. Steady state values for P, N, and ϕ are perturbed by time varying terms δP, δN, and $\delta\phi$. The equations are linearized and then fourier transformed. The spectral density of the frequency noise is defined as $S_f = < |\omega\delta\tilde{\phi}(w)|^2 >$ and the line width at $\omega = 0$ is:

$$\Delta\nu = \frac{S_f(0)}{2\pi} = \frac{2R_{sp}}{P}(1+(\alpha G_N P)^2\frac{G'^2+2\Gamma_P G'+\Gamma_P^2(1+\gamma_e N/(R_{sp}P))}{(\Omega_R^2+\Gamma_R^2)^2} \tag{5.10}$$

$$\Omega_R = [G'(G_N P+2R_{sp}/N)-\frac{1}{4}(\Gamma_N-\Gamma_P)^2]^{1/2}, \quad \Gamma_R = (\Gamma_N+\Gamma_P)/2 \tag{5.11}$$

$$\Gamma_P = R_{sp}/P+\varepsilon_{NL}GP, \quad \Gamma_N = \gamma_e+N(\partial\gamma_e/\partial N)+G_N P(1-\varepsilon_{NL}P) \tag{5.12}$$

where Ω_R is the relaxation oscillation frequency and Γ_R is the damping rate of the relaxation oscillations. The non linear gain $G' = G(1-2\varepsilon_{NL})$ but we have set $\varepsilon_{NL} = 0$. We plug the threshold fit from section 5.5.1 in equation 5.10 and plot line width as a function of inverse integrated laser power. The same scaling factor used earlier for fitting the threshold curve is used in figure 5.11(a). The line width enhancement factor α is fit or adjusted until the local line width maximum matches that of the data $\delta\nu \sim 44.5$GHz. Using an $\alpha = 3.34$ the model fits the data only in a qualitative fashion, the line width decreases with increased power, temporarily increases, and then decreases again. Since the out coupling is not a calibrated quantity if it is further reduced by a factor of 4 the model more closely follows the data as can be seen in figure 5.11(b). Further understanding of the model needs to occur to explain the out coupling efficiency difference between the threshold curve and the line width curve. The line width predicted by the model for lower powers is lower than observed in the data.

An $\alpha = 3.34$ falls on the low end, but well within the range of line width enhancements previously measured of $\alpha = 2-5$[61]. By slightly adjusting the values one can see that the fit value of α is sensitive to the recombination rate including the surface recombination rate added to this model.

5.6 Conclusions

In this chapter we have been able to measure anti-crossing behavior in a sub-wavelength microdisk. Several iterations of FEM simulations have been undertaken, highlighting the need for very accurate knowledge of the material refractive indices and precise knowledge of the geometry. Lasing was

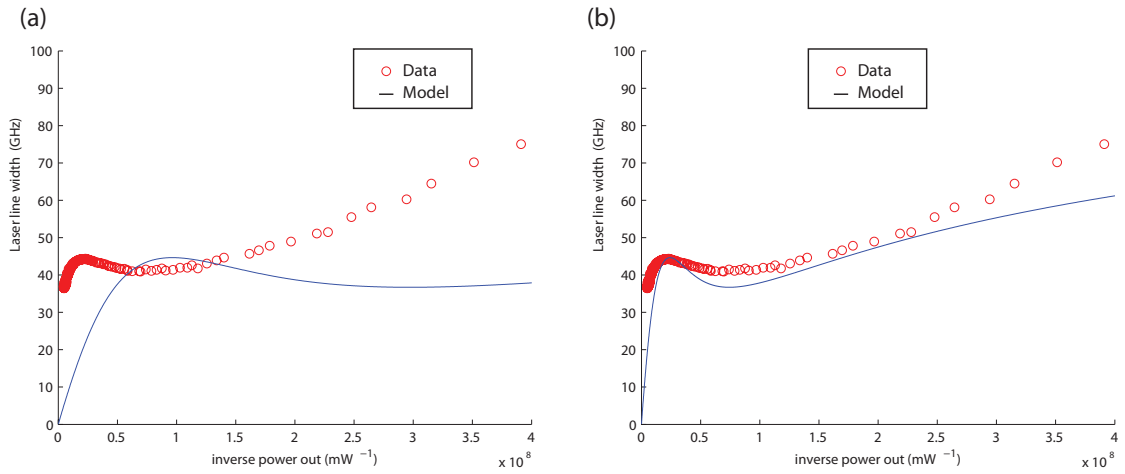

Figure 5.11: (a) Line width data from device 10 and model. (b) Model with out coupling scaled.

achieved in a weakly hybridized disk with an intimate metal contact. The significant role of surface recombination due to a high surface to volume ratio in these cavities is highlighted by the fact the surface recombination makes is difficult to estimate the rate of spontaneous emission going into the lasing mode (β) from the threshold curve. A super linear recombination term is added so the sub-threshold slope can be properly fit. A first pass line width modeling was carried out. Further future work could be carried out on both the threshold and line width models for them to be commensurate with the requirement posed by Björk and Yamamoto that the spontaneous emission must equal the differential gain when there is one photon in the cavity [60]. Of course Purcell enhancement of the spontaneous emission can be included [92]. The next experimental step would be to carry out correlation HBT measurements. Even further down the line, one would want to carry out these same experiment with an electrically pumped active material. A top metal contact would allow for even better heat sinking as well as observation of current behavior.

Chapter 6

Quantum Dot Microdisk Cavities for Strong Coupling

6.1 Introduction

Over the past several years, our group has been developing techniques and tools for studying cavity quantum electrodynamics (cQED). This included both the development of microdisk and photonic crystal cavities as well as further developing the evanescent fiber taper coupling techniques [93, 94]. In order to observe cQED behavior, an "atomlike" system coupled to an optical cavity, must be in the strong coupling regime. Strong coupling is a regime where coherent interaction can occur between the "atomlike" system and the cavity field. This means that the interaction timescale is faster than any other dephasing timescales in the coupled system. In our lab we have focused on solid state system of a quantum dot within a microdisk cavity. The "atomlike" system is an exciton in an InAs QD embedded in $In_{0.7}Ga_{0.85}As$ quantum well (Dot-in-Well material, i.e., DWELL [95, 96]), all within a 256nm thick GaAs microdisk cavity. A schematic and SEM micrograph of the system are shown in figure 6.1. Getting to the strong coupling regime involves getting all of the loss rates to be smaller than the quantum-dot–cavity coupling rate (g):

$$\frac{g}{2\pi} = \sqrt{\frac{3c\lambda_0\tau_{sp}}{2\pi n^3 V_{eff}}}, \tag{6.1}$$

where c is the speed of light, V_{eff} is the mode volume, λ_0 the free space wavelength, n the refractive index, and τ_{sp} the radiative lifetime. The cavity loss is parametrized by κ:

$$\frac{\kappa_i}{2\pi} = \frac{\omega}{4\pi Q}, \tag{6.2}$$

where ω is the frequency and Q is the optical quality factor of the resonator. One can see that to get to the strong coupling regime, g must be optimized and κ_i minimized. Optimization of the microdisk cavity geometry leads to a choice or radius which minimizes V_{eff} and optimizes Q. It is of course important to note that the coupling rate to the fiber taper, which provides input/output from the cavity, not limit the cavity Q.

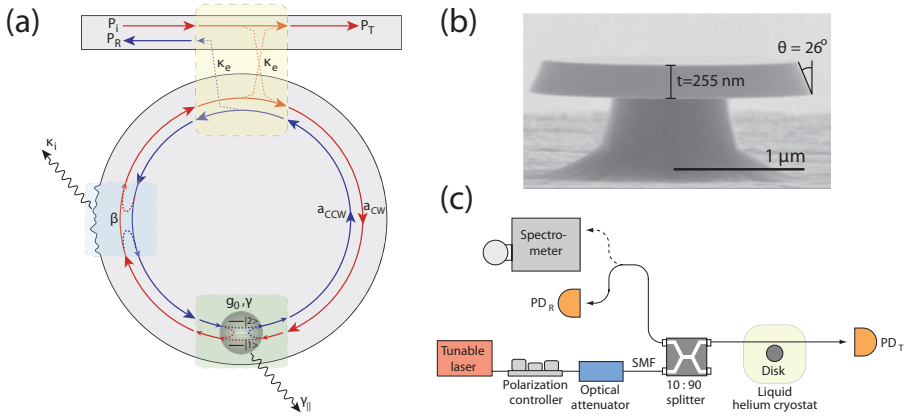

Figure 6.1: Illustration of the system under investigation, reproduced from reference [4]. The microcavity-quantum-dot system is driven near resonance by coupling light into and out of it using an optical fiber taper waveguide, with a cavity-waveguide coupling rate κ_e (κ_e is a field amplitude decay rate. Imperfections in the microdisk cause a coupling of the clockwise and counterclockwise whispering-gallery modes, at a rate β. These two whispering-gallery modes have a quantum-dot-cavity coupling rate g_0 and intrinsic cavity decay rate κ_i. The quantum dot, approximated as a two-level system, has a radiative decay rate $\gamma_{||}$ and a total transverse decay rate $\gamma_{\perp}$. (b) SEM micrograph of microdisk cavity. (c) Schematic for fiber taper based spectroscopy of cavity-QD system.

In 2007 Srinivasan was able to get to the strong coupling regime [85, 13]. Microdisks are placed in a liquid helium flow cryostat and are probed using fiber taper based spectroscopy at $T = 8 - 15$K. The optical modes are tuned into the exciton resonance by controlled Nitrogen ice deposition. Srinivasan was able to show that strong coupling was achieved by observing vacuum Rabi splitting as well as saturation of the cavity-quantum dot response with less then one photon in the cavity. In a theoretical paper, Srinivasan predicts the behavior of the intensity correlation function $g^{(2)}(\tau)$. Such behavior is associated with nonclassical behavior of the optical field [97] and is of importance in the characterization of QD-cavity based devices such as single photon sources [98, 99, 100, 101]. There are of course competing efforts, some of which are included in references [102, 85, 13, 103, 104]. Recently in reference [105] correlation functions were measured. The hope is that the better quantitative knowledge of pump and probe powers due to the use of the tapered optical fiber will let

us more fully probe the system.

We would like to experimentally measure $g^{(2)}(\tau)$ in a strongly coupled QD-microdisk system. Unfortunately, the sample Q has degraded over time and the strong coupling regime can no longer be reached with samples used in Srinivasan's work. Reasons for degradation are not yet fully understood, but repeated cool downs and exposure to air may be factors. Therefore new devices must be made. In this chapter work towards making another strongly coupled sample with improved odds is presented. Before the methods are discussed, the general process of finding a strongly coupled device must be described. A detailed methods description is found in reference [5]. I will briefly summarize. DWELL material has a randomly distributed QD layer with a density of $\sim 300\mu\text{m}^{-2}$. Microdisks are fabricated with resonances at the far red tail of the QD distribution ($\lambda_0 \sim 1295$nm) where isolated QD lines can be found [106]. Many devices are made and fiber taper spectroscopy is carried out to determine which disks have high-Q resonances at $\lambda_0 \sim 1300-1310$nm (the resonances blueshift at low temperature.) The sample is then cooled and the periphery of the disk is resonantly pumped with a 980nm laser and PL is collected. This allows us to look for dots with isolated exciton resonances that are found along the periphery of the disk. Once such a device is found, one is ready to probe it for strong coupling and associated phenomena.

In this chapter we attempt to improve the microdisk cavity fabrication and design in order to achieve strong coupling more easily by (i) using newly grown DWELL material, (ii) moving beam writing from our homemade beam writer based on an SEM to a high precision Leica 5000+ beam writer, (iii) using passivation techniques to mitigate optical loss due to surface states, and (iv) changing microdisk geometry to avoid or mitigate low Q TM whispering gallery modes that limit the Q of our desired TE modes. Work on this project is done in close collaboration with T. Alegre.

6.2 Fabrication

QD microdisk cavities are fabricated in a very similar fashion to GaInAsP based lasers fabrication in chapter 4. The DWELL material used is a layer of InAs dot with InGaAs QW buried in a GaAs waveguide layer, on top of an AlGaAs sacrificial layer. Details of the epitaxy are shown in table 6.1. A 240nm layer of SiNx is deposited via PECVD. The samples are then cleaved into $\sim$ 10mm by 10mm squares. E-beam resist ZEON ZEP520A is spun at 2500RPM for 60sec and oven baked at 180C for 20min. Yielding a layer that is $\sim$ 450nm thick in preparation for electron beam lithography. A very brief $3-5$sec dip in buffered HF Improved (Transene) was carried out to aid in adherence

Table 6.1: 1-Dot-in-Well (1-DWELL) material epitaxy. Growth run 2579. (ML: mono layer)

Layer	Material	(nm)
Waveguide layer	GaAs	10nm
	$Al_{0.3}Ga_{0.7}As$	40nm
	GaAs	74nm
Quantum Well	$In_{0.15}Ga_{0.85}As$	6nm
Quantum Dot	InAs	1.57ML
Quantum Well	$In_{0.15}Ga_{0.85}As$	1nm
	InAs	0.83ML
	GaAs	74nm
	$Al_{0.3}Ga_{0.7}As$	50nm
Sacrificial layer:	$Al_{0.7}Ga_{0.3}As$	1500nm
	GaAs	200nm
Substrate:	GaAs S.I.	

of the resist.

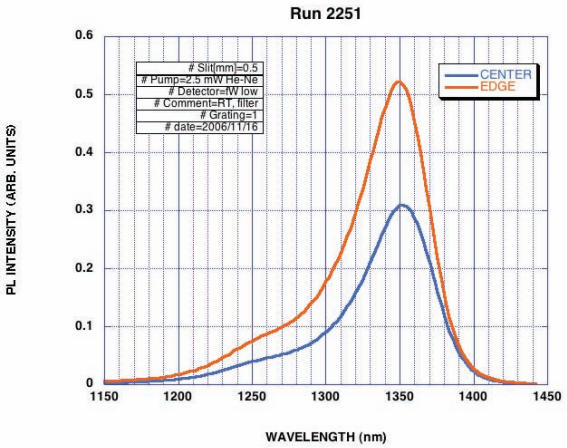

Figure 6.2: Room temperature photoluminescence from growth run 2251.

The beam write is carried out on the Leica 5000+ beam writer in the KNI facility. The beam write is designed to significantly increase the chance of finding a strongly coupled QD. In work by Srinivasan summarized in reference [5] only up to $\sim$ 100 devices (with a very slight size variation) were beam written due to limited speed, beam current stability, and a 2D flat plane (beam writing is typically done along one direction which is known to be flat.) In the past, once etched and tested, the microdisks were digitally etched in peroxide and citric acid to blue tune the resonances to overlap

with single exciton lines. For a single peroxide/citric acid cycle, a Q of 10^5 decays by less than 10% and the wavelength blueshifts by ~ 4.5nm. By the time the modes are shifted by 6 cycles (~ 42nm) the Q can degrade by as much as 25%. Using the beam writer 100 disks of one diameter are beam written. Twenty-five such patterns are beam written with incrementally increasing disk diameter. The hope is that one or two patterns will overlap with the red tail of the QD emission at low temperature and we will have $100-200$ devices of the appropriate wavelength. Digital etching will hopefully be avoided. Each sample is typically beam written with a 4 by 4 array of 25 patterns. This lets us make 16 close to identical samples per beam write. It is important to note that this layout is designed for dimple fiber testing so no optical isolation step is needed [79]. Dose runs were done and an optimal dose of $120\mu\text{Ccm}^{-2}$ is used. With ~ 1.3nA beam and speeds of ~ 45MHz a typical beam write takes $\sim 8-9$ hours. A typical beam write and beam write pattern are shown in figure 6.3.

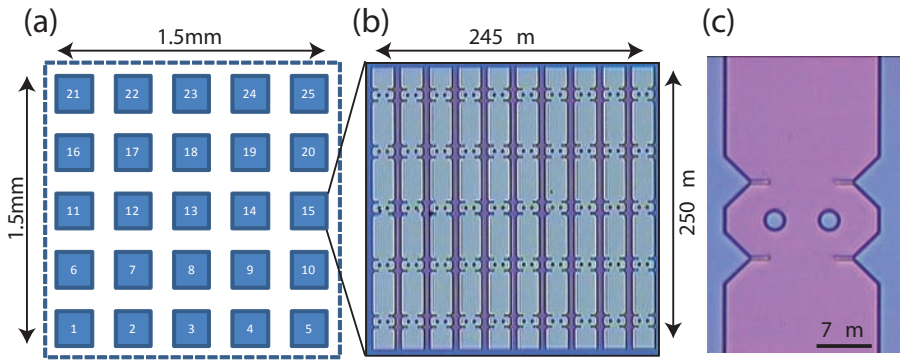

Figure 6.3: The beam write usually consists of a 4 by 4 array of individual sample dyes. (a) Schematic of each dye: 25 patterns each with increasing disk diameter. (b) Optical image of each pattern that contains 100 disks of the same size. (c) Zoom in of a set of two disks with forks.

Since the eventual goal is to measure photon statistics, i.e., correlation functions, of strongly coupled QD-microdisk cavity system one will need to carry out Hanbury-Brown-Twiss (HBT) based experiments. Due to the long recovery time of the single photon counters in Geiger mode, the light sent to them must be significantly attenuated and the experiment must therefore be run for long periods of time, i.e., hours. Fiber taper spectroscopy can be carried out with the fiber hovering (un stable) or touching (stable) the microdisk. A feature incorporated into this beam write are forks. Forks are cantilevers on either side of the disk which extend towards it [107]. The fiber taper can be rested on the cantilevers for stability. By careful placement of the fiber on the forks the distance between the disk and the taper can be controlled. This will allow for optimizing the coupling from

Table 6.2: ICP/RIE - DWELL/GaAs etch conditions

Parameter	Value Requested	Actual Value
RF	245W	(248/17W)
ICP	175W	(159/1W)
DC Bias		$\sim$ 385V
Cl_2/Ar	3.5/16sccm	(3.1/15.6sccm)
P_{ch}	2mTorr/APC 15deg	(1.9mTorr)
P_{He}	15Torr	(12.2sccm
T	20C	(32C)
t	3min	

disk to taper (κ_e.)

Once the samples are beam written, they are developed for 3min in ZEON ZED-ND, rinsed in ZEON ZMD-D for 30sec and are reflown at 165C for 5min, yielding highly sloped side walls. The samples are typically cleaved several times to allow for process development and control. The e-beam resist mask is transferred to the SiNx via ICP/RIE etching as is shown in table 4.3. The resist is then removed after level 1 ultrasonic cleaning in TCE for 10min. The GaAs waveguide layer is then etched via Ar/Cl_2 based ICP/RIE etching (details in table 6.2). The key to this clean smooth etch is the high bias coupled with significant cooling due to high helium backing.

To undercut the disks, 60:1 H_2O:HF is used (starting HF percentage is 49%). The undercut is carried out immediately after the sample comes out of vacuum. If there is a delay a significant layer of residue, possible attributed to oxidation of the AlGaAs, accumulates on the disks. The leftover SiNx hard mask is partially receded during the HF undercut. It is then fully removed using an ICP/RIE etch as in chapter 4. SEM micrographs of the various fabrication steps are shown in figure 6.4.

6.3 Room Temperature Testing

The devices are then tested. Testing is carried via dimpled fiber taper spectroscopy either in the cryostat or in a similar setup outside of the cryostat. The samples are tested in the 1300nm band using a Velocity tunable laser (New Focus), as well as the 1500nm with either a Velocity or Vidia tunable lasers (New Focus). Testing is done in both bands for several reasons. The room temperature PL shows the QD spectrum blue tail to overlap with the testing region, see figure 6.2. One can then

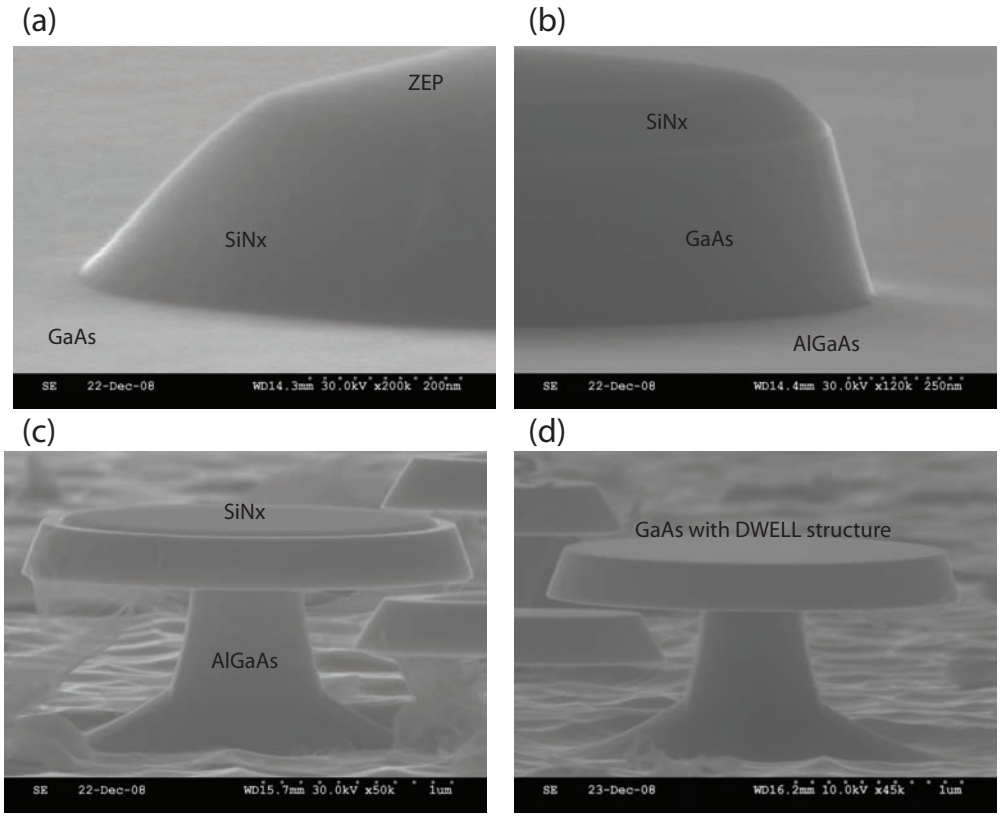

Figure 6.4: (a) SiNx ICP/RIE etch with leftover resist. Etch stops on GaAs surface. (b) GaAs ICP/RIE etch with leftover SiNx. Etch proceeds smoothly into AlGaAs sacrificial layer. (c) HF undercut. (d) ICP/RIE SiNx removal.

test in the 1500nm band to avoid absorption, but then one has to make sure the disks are not too small and are therefore radiation limited. Furthermore a disparity in material absorption and sensitivity to surface roughness may very well exist. These factors should be kept in mind when reviewing the following testing data.

Testing is carried out with the fiber taper hovering, not touching, the disks. Forks are not used to increase the speed of testing. The fiber taper is typically brought in close to the disk, polarization is optimized, and then the taper is backed away until fiber-disk coupling is $\sim 5\%$. In both wavelength bands the power is kept low to avoid thermal bistability, i.e., thermal tuning of the modes. A typical mode scan is shown in figure 6.5(a) exhibiting a doublet indicating clockwise and counterclockwise modes whose degeneracy is split by surface scattering. The data is fit (see reference [108]) and both Q and mode splitting ($\Delta\lambda$) are extracted. Q is inversely proportional to line width ($\delta\lambda$). $\Delta\lambda$ is an indication for backscattering from CW to CCW modes and can therefore be an indication of surface roughness. A summary of wavelength vs. pattern number for several samples with

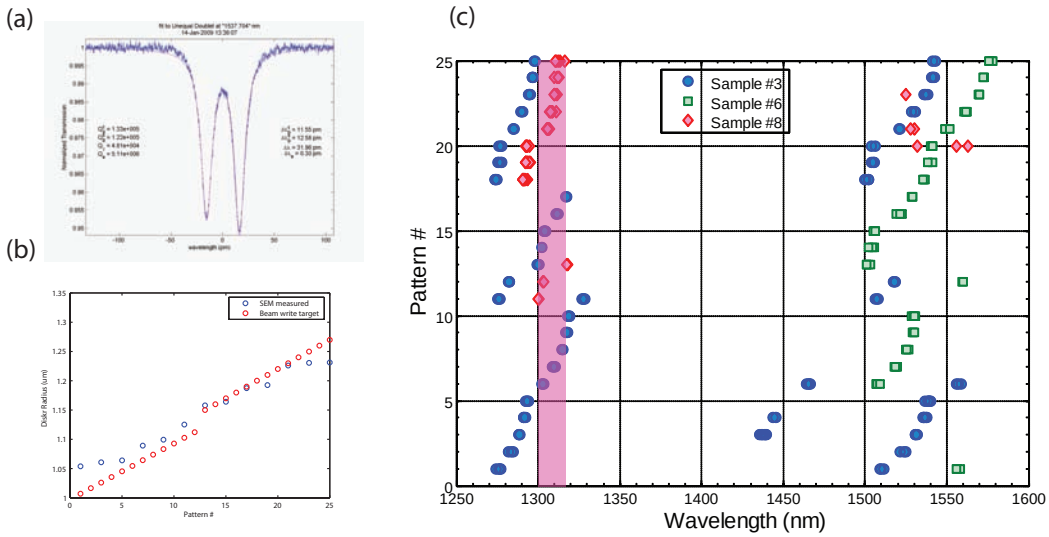

Figure 6.5: (a)Typical fit and analysis of transmission spectra of a doublet. Both Q and splitting are calculated. (b) Comparison of beam written target radius and achieved radius. Radius values are used for reference in subsequent figures. (c) Summary of microdisk resonances as a function of pattern number in both the 1300nm and 1500nm band. Diagonal grouping of resonances indicated modes of same m number.

slightly different processing conditions is summarized in figure 6.5(c) for both wavelength bands. The samples mainly differ in depth of the GaAs etch. The diagonal grouping of modes indicate tuning of specific m number modes. In the 1300nm band the samples span 3 m number modes. It is important to note that final samples considered candidates from strong couping are not SEMed for fear that imaging may damage their Qs or shift their wavelength due to carbon deposition. A plot of pattern number vs. measured size for a similarly processed device to the ones tested is shown in figure 6.5(c). Disk sizes of radius $R = 1 - 1.25\mu$m can be achieved with high fidelity to intended beam write.

In the 1500nm band the Q steadily improves as a function of pattern number or disk size. This could be attributed to the radiation limit, though not necessarily as the Q is wavelength independent. Splittings under 100pm show very little effect on Q indicating that Q is not limited by surface roughness. In the 1300nm band, the Q increases with disk size but decreases with wavelength, most likely due to QD absorption. As in the 1500nm, band below a splitting level of 70pm the Q is splitting independent.

The drop in Q in Sample 8 in the 1300nm band may also be explained by mode mixing of a low Q TM mode with our high Q TE modes. In figure 6.7 transmission spectra for the two polarization

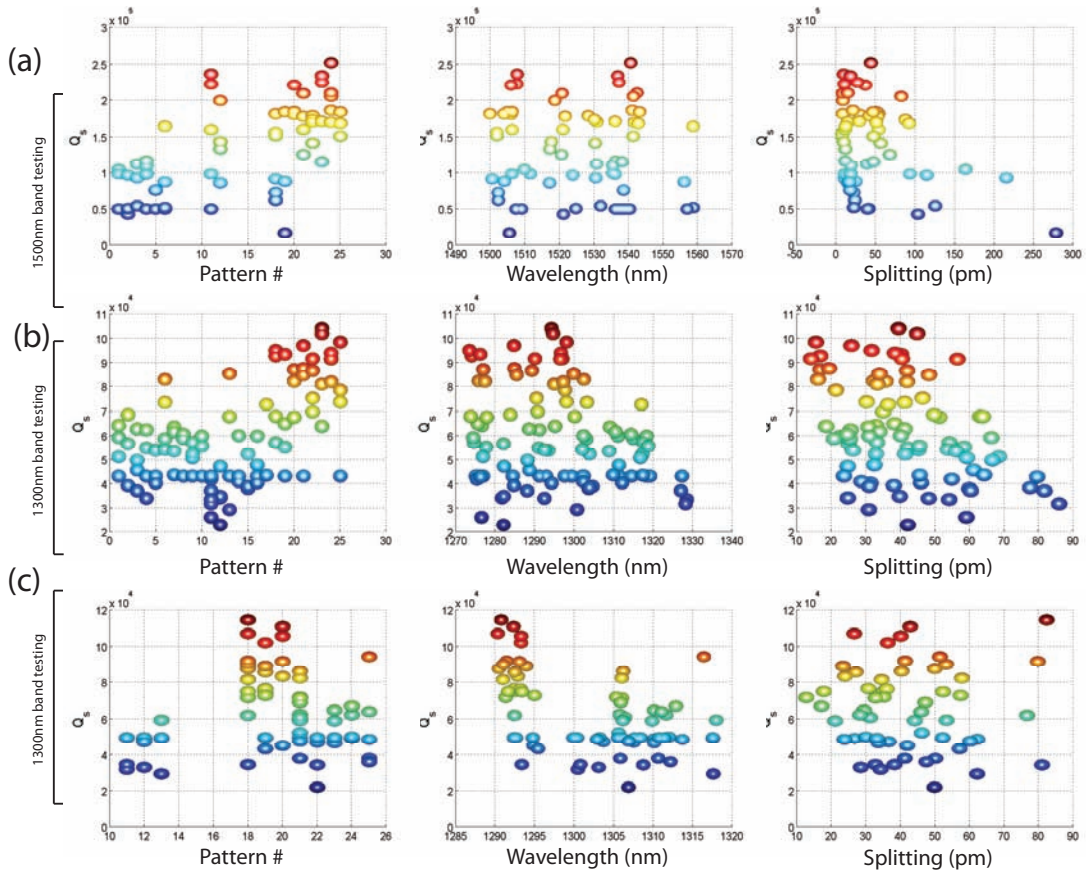

Figure 6.6: Q as a function of pattern number, wavelength, and splitting is shown for (a) sample 3 in the 1500nm band, (b) sample 3 in the 1300nm band, and (c) sample 8 in the 1300nm band.

modes are plotted. Spectra are taken with the fiber taper touching the disks, explaining the high degree of coupling. The polarization for the TE mode is first optimized (red) and subsequently the polarization is changed in an attempt to optimize the coupling of the TM mode. The TM mode is clearly broader, and therefore lower Q. Furthermore it is not possible to completely extinguish the TE mode. The modes are therefore partially coupled and the low Q of the TM mode could be limiting the Q of the TE mode. This mode mixing needs to be avoided. But if it can not be, then the TM mode needs to come up in Q as to not limit the TE mode. The disks therefore need to be made larger to avoid the lower radiation limit of TM modes. This is necessary as the modes of interest with $\lambda = 1310$nm seem to be affected.

We also look the wavelength and Q uniformity within each disk-size subpattern. Q and wavelength as function of spatial location within a subpattern are shown in figure 6.8. The wavelengths all fall with in roughly a 4nm window with the exception of the subpattern edges. This may be

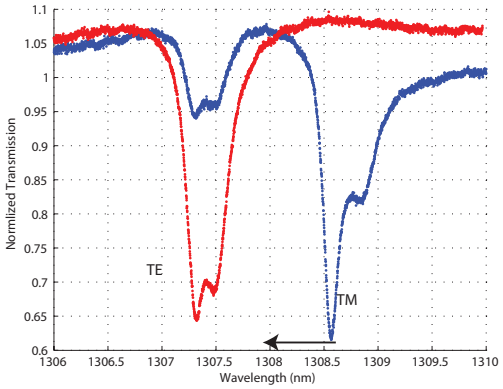

Figure 6.7: TM and TE modes of microdisk in pattern 22

explained by proximity effects of the beam write. What is interesting and encouraging to see is that the Q has no spatial dependence. It appears that the Q is random or most likely associated with particulate residue left over from the undercut process. An improvement of the undercut process may yield more uniform results.

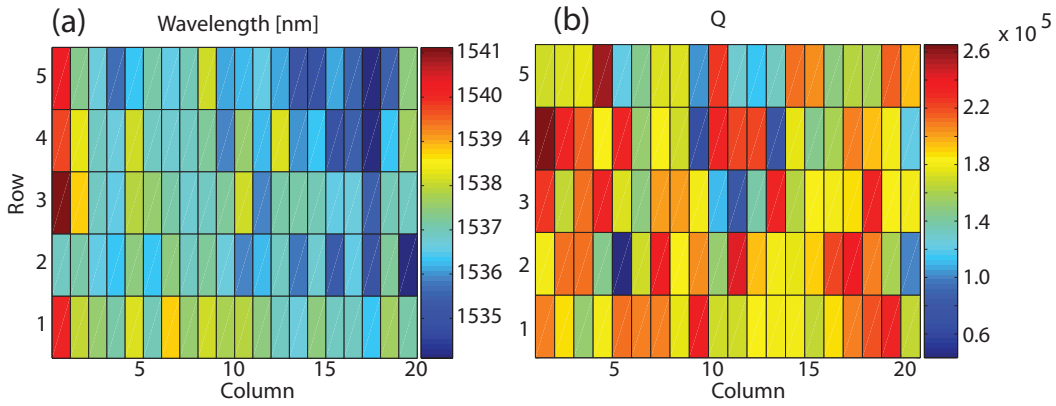

Figure 6.8: (a) Spatial distribution of wavelength within one pattern beam written to be one disk size. (b) Spatial Q distribution within one pattern.

6.4 GaAs Surface Passivation Using Ammonium Sulfide

With significant reduction in the dimensions of microdisk GaAs cavities, the surface-to-volume ratio is significantly increased. It is therefore possible that surface absorption is a significant contributor to optical loss. GaAS surfaces are known to have large recombination velocities ($S_0 \sim 10^6$cm/s)

and high surface state densities ($N_s \sim 10^{12}\text{cm}^{-2}\text{eV}^{-1}$) [109]. This leads to both electrical and optical performance device limitations and has been studied and mitigated via sulfur based passivation since the late 1980s [110, 111, 109]. Original passivation techniques utilized sodium sulfide but many other sulfur based compounds have been used since [112]. Ammonium sulfide based passivation techniques have been applied both to microdisk and photonic crystal lasers with significantly reduced thresholds [23, 113]. Such performance increases may indicate that we can reduce surface loss in our QD microdisk cavities through similar treatments. For our passivation recipe we choose reference [112] as it takes a systematic approach to measuring etch rates for GaAs and $Al_xGa_{1-x}As$ as a function of temperature and excess sulfur.

In order to passivate our GaAs/DWELL microdisk a double boiler system was set up. A large water filled beaker is kept at 60C. A test tube filled with $\sim$ 50ml of 20% ammonium sulfide in water is suspended in the water bath. The sample is held by Teflon tweezers with a bolted squeeze mechanism. The tweezers are suspended in the test tube by Teflon string. A stopper with Teflon tape keeps the solution from evaporating and anchors the Teflon string. Through the stopper a thermometer is used to keep track of the solution temperature. Magnetic spinners are used to agitate and maintain constant bath and solution temperature.

To begin, ammonium sulfide passivation is carried out on sample which had previously been only partially undercut. This is necessary as the sacrificial $Al_{0.7}Ga_{0.3}As$ etches extremely quickly. At 60C the GaAs disk should etch at $\sim$ 11nm/hour while $Al_{0.7}Ga_{0.3}As$ etches at least two orders of magnitude faster. The sample is first dipped in ammonium hydroxide solution (NH_4OH:H_2O 1:25) at room temperature for 2min to remove any native oxide growth. It is then placed in 20% solution at 60C. The sample is then rinsed in water, IPA, and N_2 dried. Patterns $1-15$ are undercut fully due to their smaller diameter and the microdisk cavities are no longer testable. Larger disks from pattern 19 through 25 are tested in both the 1500nm and 1300nm bands.

Data for Q versus wavelength before and after treatment for both bands can be seen in figure 6.9. The Q of modes in the 1300nm band improves. This improvement is coupled with a wavelength shift which can be attributed the reduced size due to the etching of the GaAs microdisk both in thickness and radius. In the 1500nm no improvement is observed. The improvement in the Qs in the 1300nm band may be attributed to shifting of the resonances away from the absorption maximum at $\lambda = 1350$nm (see figure 6.2.) In order to gauge the success or failure of these treatments two things need to be done. Bigger disks need to be made to make sure the region of low Q TM and high TE mode mixing is avoided. Second, low temperature measurements of the devices in the 1300nm band

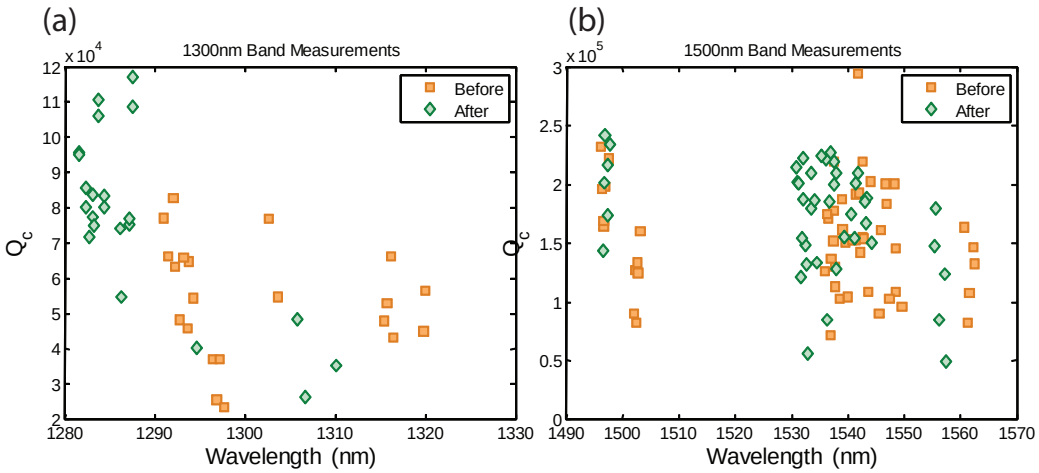

Figure 6.9: (a) Optical Q before and after $(NH_4)_2S$ treatment in the 1300nm band. (b) Optical Q before and after $(NH_4)_2S$ treatment in the 1500nm band.

need to be carried out as to avoid the QD absorption.

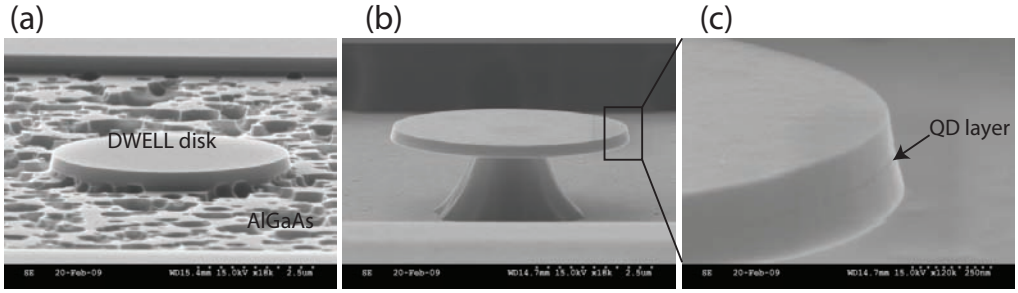

Figure 6.10: (a) SEM micrograph of HF undercut after direct resist to GaAs processing. AlGaAs is pocked and un etched indicating some sort of barrier layer. (b) SEM micrograph of subsequent 20*min* $(NH_4)OH/(NH_4)_2S$ treatment. (c) Zoomed in SEM of disk edge showing some QD layer damage.

Previous attempts were made in the past to make larger Microdisks ($R = 1.5\mu$m) using a direct e-beam resist to GaAs pattern transfer. While a very nice etch was optimized, undercutting the disks proved strangely difficult. A disk after HF undercut is shown in figure 6.10(a). There appears to be either a deposited layer of etch products remaining on the surface or a modified top surface, preventing the undercut process. It is possible for example that the Al concentration is reduced by the etch making the top layer behave more like GaAs and therefore etch slower. Since ammonium sulfide etches $Al_{0.7}Ga_{0.3}As$ quite easily as well as GaAs, we are now able to successfully undercut the disk with a 20min etch. Looking at the pedestal interface with the substrate, it appears like the

$Al_{0.7}Ga_{0.3}$ is fully removed.

Accordingly, we develop a process to fabricate GaAs/DWELL Microdisks using only e-beam lithography and a GaAs etch. The hope is that in avoiding the use of SiNx hard mask we would benefit is several ways. First, the sample's temperature would never be elevated above the bake temperature of the resist. Second, the epitaxy will not be strained by the deposition of strain relieved, but never the less strained, SiNx. And finally, we can avoid the delicate process of removing the hard mask without damaging the semiconductor surface.

The fabrication process is summarized with SEM micrographs in figure 6.11. The main differences from the SiNx mask based process is that the lithography reflow is more a more gentle 145C for 7.5min. The GaAs ICP/RIE is changed a bit. The RF/ICP powers are changed to 150W/225W and the He cooling is reduced to P=10Torr. It takes about 1min 45sec to get through the GaAs disk.

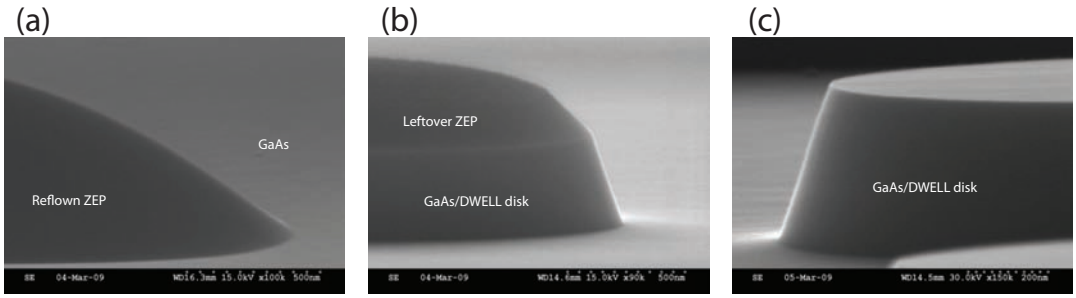

Figure 6.11: (a)SEM micrograph of reflown ZEP mask directly on GaAs. (b) SEM micrograph of ICP/RIE etched GaAs using only a ZEP resist mask. (c) SEM micrograph of GaAs etch after resist has been easily removed.

The undercut is slightly more challenging than expected. As before an HF undercut is halted at the surface with a bit of pock marking occurring, even with an ammonium hydroxide oxide removal step (figure 6.12(b)). On the other hand, an ammonium hydroxide cleaning step plus an ammonium sulfide undercut step leads to significant build up of residue on the disk edges as seen in figure 6.12(a). It turns out that a combination of HF undercutting and subsequent ammonium sulfide undercutting yields a very clean and smooth disk surface.

Larger disks were then fabricated using direct e-beam resist to GaAs mask transfer. Disk sizes varied between $R = 1.25 - 1.5\mu$m. Undercutting the Microdisks cleanly took two cycles of 1min HF etch and 4.5min of ammonium sulfide etch. Each etch was always preceded by a 2min ammonium hydroxide etch to remove any possible oxide. Current room temperature and low temperature testing is ongoing.

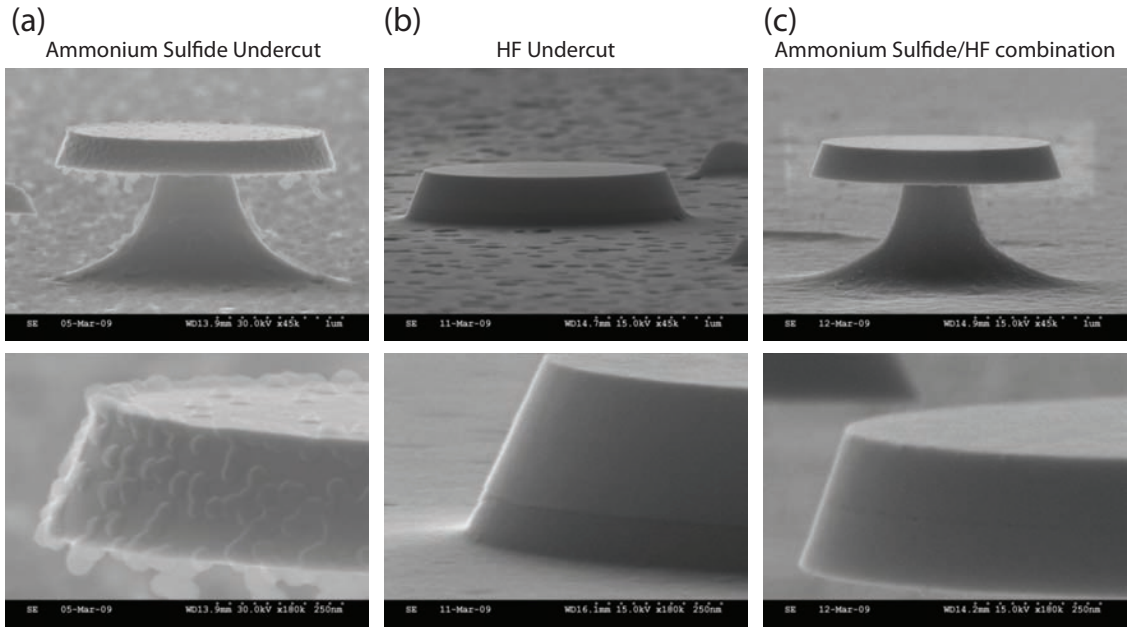

Figure 6.12: (a) SEM micrograph of Ammonium Sulfide undercut showing residue. (b) SEM micrograph of HF undercut showing no undercutting action. (c) SEM micrograph of a combination HF/Ammonium Sulfide undercut showing a very clean undercut.

6.5 Low Temperature Testing

The next step in this process is to measure the disks at low temperature. First, at $T = 15$K the QD absorption spectrum will shift to the blue of the cavity modes and allow for true cavity Q measurements in the 1300nm band. Second, the disks will be tested for the presence of QDs in the periphery of the disks. The disks will be pumped by a 980nm whispering gallery mode and QD emission is collected and sent to the spectrometer. An example from a previous round of measurements [5] of expected behavior is shown in figure 6.13.

6.6 Conclusions

We have devices ready for exciton hunting. Over the next several weeks 100 to 200 will be tested for resonance position, Q, and exciton spectral position. Once several candidates are chosen N_2 ice tuning will be used to test for strong coupling. In this chapter we have significantly improved our chances of finding a strongly coupled device, as well as added forks for stability, and explored surface passivation techniques. Even thought the benefit of surface passivation is questionable at the moment, ammonium sulfide based undercuts have solved the difficulty of etching AlGaAs cleanly

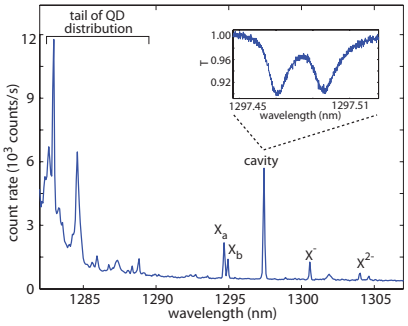

Figure 6.13: Example of fiber-collected PL spectrum under pumping of a 980nm band WGM (5nW input power into the fiber taper). QD states are labeled as X^a/X^b (fine-structure split neutral exciton states), X^- (negatively charged exciton), and X^{2-} (double negatively charged exciton.) The inset shows a normalized transmission scan of the cavity mode at $\lambda = 1297.5$nm. Sample temperature $T = 15$K. [5]

and consistently. The use of ammonium hydroxide relaxes the need to carry out the undercut etch immediately after the dry etch of the QD layer.

Chapter 7

Initial Work Towards Quantum Dot Optomechanically Tuned Cantilever Laser

Very recently there has been a great interest in optomechanically coupled systems. A review of recent advances and systems is found in reference [114]. In our group, in an effort led by M. Eichenfield, mechanical oscillations of a fiber taper coupled to a microdisk were observed [11]. Followed by the design and demonstration of "zipper" cavities [115, 116]. A schematic of "zipper" structure is shown in Fig. 7.1(a). This structure is comprised of two doubly clamped cantilevers next to each other, each with a 1D photonic crystal hole pattern. This structure supports optical resonant modes as well as vibrational mechanical modes. The optical and mechanical modes are coupled by an optical gradient force.

There are many interesting phenomena, both classical and quantum mechanical, such as optical spring and back action cooling [116] that can be explored in this system. There is one though, that is most applicable the projects previously discussed in this dissertation: wide-band tuning of active optical cavities. In each and every project discussed above, a significant effort is made to fabricate devices which are spectrally aligned with a resonance of interest whether it be QW gain or QD exciton lines. Even once close enough, methods such as N_2 ice deposition must be used to tune the cavity resonances across the resonance of interest. Furthermore, almost every experiment carried out in our lab depends on a typical spectroscopic setup where a wide-band tunable external cavity diode laser is scanned and the response of the system or cavity under investigation is measured.

It has been shown, as can be seen in Fig. 7.1(c) that the resonant wavelength of a SiN_x zipper cavities can be drastically tuned by varying the photon number within the cavity and therefore the spacing between the cantilevers. Similar cavities can be designed in InP and GaAs based material

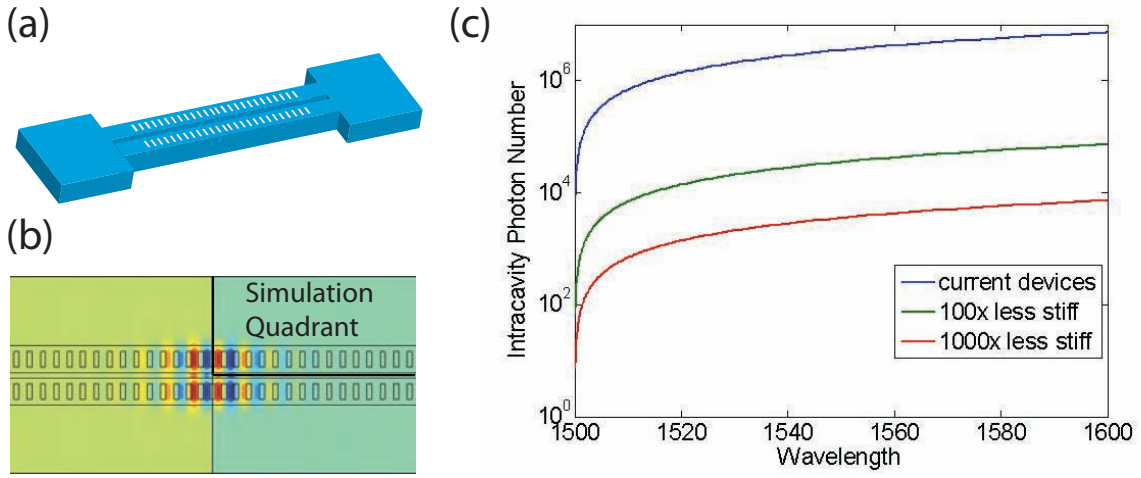

Figure 7.1: (a) Photonic crystal zipper structure. (b) Optical mode simulation (E_y) in GaAs material. (c) Optical tuning for a SiN_x zipper structure (generated by R. Camacho).

systems though their dimensions are somewhat reduced due the increase in refractive index. A simulated bonded mode in a zipper cavity is shown in Fig. 7.1(b). The purpose of this nascent project is to integrate active cavities with the ability to tune them. A first experiment would be to fabricate and test tunable chip based QD lasers. This project is a collaboration with T. Alegre, with helpful discussions with R. Camacho.

Two possible mechanisms for tuning are presented in figure 7.2. In both cases a zipper cavity is used to tune the wavelength of the cavity as a function of displacement between cantilevers. The first scheme would involve capacitive actuation of the cantilever spacing. Such a system would allow for a laser cavity to be tuned or modulated via electrical control. This would also offer a great on chip transduction of mechanical motion to an electrical signal. The second scheme is an all optical scheme that involves two zipper cavities. One zipper cavity would be the control cavity with a resonance at one wavelength. It would induce motion in the second cavity tuning its resonance. While in the schemes shown the cavity and metal contacts are physically separate, that does not necessarily need to be the case. The hope is to combine lessons learned from SP-WG hybridization and thermal management to design compact tunable cavities.

The immediate application is to create a tunable laser. Such a tunable diode laser could turn out to be much more robust than the macroscopic external cavity diode laser. Furthermore, the light will already be on the chip where it could be routed via waveguides, thus eliminating some difficulties in couping the light into high-index devices.

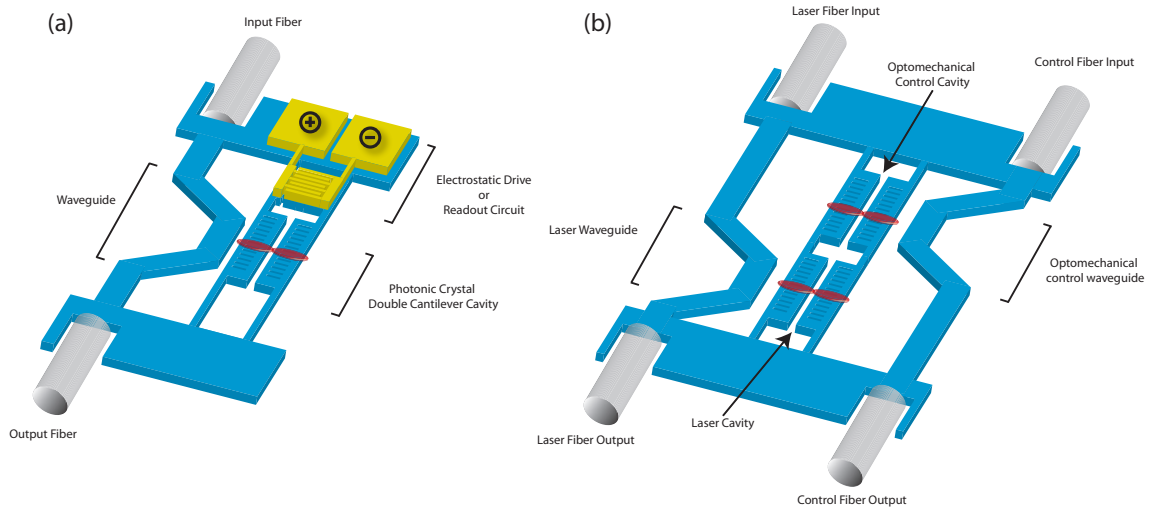

Figure 7.2: (a) Electrical tuning or induction through capacitance actuation of an optomechanically coupled microcavity. (b) An all-optical tuning scheme with two optomechanically coupled cavities.

Initial fabrication efforts to make such a zipper cavity structure in active DWELL material have begun. It turns out the these structures may be a bit of a challenge to beam write. The dimensions of the structures are fairly taxing as the gap spacing needs to be on the order of 100nm, the hole spacing $\sim$ 300nm, and width and height of the holes $\sim$ 100nm and 300nm respectively. While such a structure has been easily made by our group in both SiN_x and Si (SOI), beam writing this structure in GaAs based systems is a bit of a challenge due to significant electron backscatter and proximity effects. Lithography at both 100KeV and 30KeV has been attempted. An initial successful beam write of a zipper cavity on DWELL active material is shown in figure 7.3. At first our difficulty with beam writing seemed a bit out of the ordinary as there are countless examples of photonic crystal structures beam written on GaAs- and InP-based active material. The difference in these structures is the presence of a very large open area yielding a very significant background dosing of the few PC holes on the cantilever. We are currently exploring geometries that would limit this outside region, yielding a much more controllable beam write. This project is in its nascent stages and will hopefully lead to some very exciting results in the months to come.

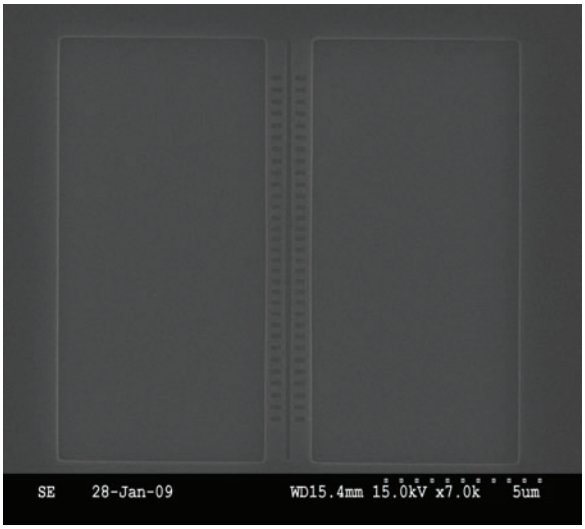

Figure 7.3: (a) SEM of Zipper cavity beam write on GaAs based QD material.

Chapter 8

Conclusion

This dissertation is a culmination of work on the investigation and application of microscale semiconductor lasers and cavities. Work concentrated on four projects: microfluidic sensing based on QC lasers, sub-wavelength hybrid mode lasers, QD based cavities for strong coupling, and nascent work on optomechanical tuning of microlasers.

Mid-infrared QC lasers were developed in photonic crystal, microdisk, and ridge geometries. Laser designs were optimized for surface sensitivity. Microfluidic and macrofluidic delivery systems were developed and implemented. A successful experimental demonstration of sensing was carried out. Laser spectra were effected by the spectral profile of the solvents leading to their differentiation. While this project met with some initial success it could be taken much further. I believe the future of QC based devices is extremely bright. The mid-infrared and terahertz regions of the spectrum are extremely important and can lead to a multitude of applications from medicine to national security. As the growth techniques for QC material mature and become more prevalent the application of QC lasers in novel geometries will become easier and more wide spread.

Work on sub-wavelength scale lasers was explored in a microdisk geometry including the beneficial inclusion of metal into the cavities. Hybridization behavior was predicted and experimentally measured in GaInAsP strained quantum well laser material. Lasing in a very small cavity was achieved and both interesting threshold and line width phenomena were observed. The next step is to fabricate and test electrically pumped lasers. This will make these lasers more technologically useful and add electrical current as another handle on the cavity physics.

QD microdisk work was carried out with the goal of making strong coupling experiments easier. Fabrication and testing methods were improved to allow for a higher chance of finding strongly coupled devices. A combination of techniques learned from the design and fabrication of hybrid mode lasers may open the door to new experiments using charge control and applying an electric

field across the QDs. Experiments are currently ongoing.

Finally, a new direction is taking form at the moment. Up untill now we have married optical, electrical, and thermal design to create very small semiconductor cavities. It is the future synergy between this effort and optomechanics that I believe has the most potential. A successful integration of optomechanics into microscale optical semiconductor cavities would be a boon for technology. The prospects of an on-chip laser that tunes across 100nm is hopefully within reach.

Appendix A

Perturbation Theory and Basic QC Laser Equations

From first-order perturbation theory of Maxwell's equations, the frequency shift of a given electromagnetic mode associated with a perturbation in the spatially dependent dielectric constant is given by [117]

$$\frac{(\omega^2-\omega_0^2)}{\omega_0^2} \cong -\frac{\int_V \left(\frac{n_e^2-n^2}{n^2}\right) n^2|\mathbf{E}|^2 d^3r}{\int_V n^2|\mathbf{E}|^2 d^3r} = -\left(\frac{n_e^2-n_0^2}{n_0^2}\right)\frac{\int_{V_e} n^2|\mathbf{E}|^2 d^3r}{\int_V n^2|\mathbf{E}|^2 d^3r}, \tag{A.1}$$

where $n(\mathbf{r})$ is the unperturbed refractive index profile, V_e is the volume encompassing the perturbation region, and n_e (n_0) is the perturbed (unperturbed) refractive index in volume V_e (the *external* cladding region in the case of the QC lasers studied here). The confinement factor of the unperturbed mode to the perturbation region is given by,

$$\Gamma_e = \frac{\int_{V_e} n^2|\mathbf{E}|^2 d^3r}{\int_V n^2|\mathbf{E}|^2 d^3r}. \tag{A.2}$$

Expanding eq. (A.1) in terms of the real (Δn_r) and imaginary ($-\Delta n_i$) components of the perturbation in the external cladding refractive index ($\Delta n = n_e - n_0$), and the resulting real ($\Delta\omega_r$) and imaginary ($\Delta\omega_i$) modal frequency shift, one obtains:

$$\left(\frac{2\Delta\omega_r}{\omega_0} - \frac{\Delta\omega_i^2}{\omega_0^2}\right) + i\left(\frac{2\Delta\omega_i}{\omega_0}\right)\left(1+\frac{\Delta\omega_r}{\omega_0}\right) \cong -\left[\left(\frac{2\Delta n_r}{n_0} - \frac{\Delta n_i^2}{n_0^2}\right) - i\left(\frac{2\Delta n_i}{n_0}\right)\left(1+\frac{\Delta n_r}{n_0}\right)\right]\Gamma_e. \tag{A.3}$$

For small fractional frequency shifts ($\Delta\omega_r, \Delta\omega_i \ll \omega_0$), and to first order in Γ_e, the real and imaginary modal frequency shifts are approximately,

$$\frac{\Delta\omega_r}{\omega_0} \cong -\frac{\Delta\lambda}{\lambda_0} \cong -\left[\frac{\Delta n_r}{n_0} - \frac{\Delta n_i^2}{2n_0^2}\right]\Gamma_e, \tag{A.4}$$

$$\frac{\Delta\omega_i}{\omega_0} \equiv \frac{1}{2Q_e} \cong \left[\left(\frac{\Delta n_i}{n_0}\right)\left(1+\frac{\Delta n_r}{n_0}\right)\right]\Gamma_e. \tag{A.5}$$

For small fractional perturbations to the refractive index of the external cladding one obtains to first order a modal frequency shift which is linear in the refractive index shift,

$$\frac{\Delta\omega_r}{\omega_0} \cong -\left(\frac{\Delta n_r}{n_0}\right)\Gamma_e, \tag{A.6}$$

$$\frac{\Delta\omega_i}{\omega_0} \cong \left(\frac{\Delta n_i}{n_0}\right)\Gamma_e. \tag{A.7}$$

The field amplitude decay per-unit-time represented by $\Delta\omega_i$ can be related to an energy loss per unit length through the modal group velocity ($v_g \equiv c/n_g$),

$$\bar{\alpha}_e \equiv \frac{2\Delta\omega_i}{v_g} \cong \left(\frac{n_g}{n_0}\right)\left(\frac{4\pi\Delta n_i}{\lambda_0}\right)\Gamma_e = \left(\frac{n_g}{n_0}\right)\alpha_e\Gamma_e, \tag{A.8}$$

where α_e is the *bulk material* exponential energy loss coefficient of the dielectric perturbation. Note that the prefactor n_g/n_0 in eq. (A.8) accounts for the fact that the guided mode energy may propagate at different effective velocity than a wave in the bulk cladding material for which n_e (and thus Δn_i) are written.

One can show [118] that for quantum cascade active regions, the modal gain is directly proportional to injection current density (J) through a differential modal gain constant (g_m'). In what follows, we carefully derive a relation for modal gain which takes into account both electronic properties of the QC active region (laser transition dipole moment, carrier lifetimes, etc.) as well as properties of the laser mode (active region overlap, energy velocity, etc.). We begin with a standard result from quantum optics which relates the spontaneous emission rate from the laser transition dipole to the local cavity mode electric field strength *per photon* and the dipole dephasing rate:

$$g_m = \frac{\mu \cdot \mathbf{E}_m}{\hbar}, \tag{A.9}$$

$$\mu = e\langle \hat{\mathbf{r}} \rangle \approx e\langle \hat{z} \rangle, \tag{A.10}$$

$$|\mathbf{E}_m(\mathbf{r}_0)| = \sqrt{\frac{\hbar\omega}{\varepsilon_0 n^2(\mathbf{r}_0) V_{\text{eff}}(\mathbf{r}_0)}}, \tag{A.11}$$

$$V_{\text{eff}}(\mathbf{r}_0) = \frac{\int_V \varepsilon_0 n^2 |\mathbf{E}_m|^2 \mathrm{d}^3\mathbf{r}}{\varepsilon_0 n^2(\mathbf{r}_0)|\mathbf{E}_m(\mathbf{r}_0)|^2} = \frac{\hbar\omega}{\varepsilon_0 n^2(\mathbf{r}_0)|\mathbf{E}_m(\mathbf{r}_0)|^2}, \tag{A.12}$$

$$R_{\text{sp},m}(\mathbf{r}_0) \approx \frac{g_m^2}{\gamma_e} = \frac{|e|^2 |\langle \hat{z} \rangle|^2 \omega}{(\hbar\gamma_e)\varepsilon_0 n^2(\mathbf{r}_0) V_{\text{eff}}(\mathbf{r}_0)}, \tag{A.13}$$

$$\tag{A.14}$$

where g_m is the coherent coupling rate between the cavity mode and electronic dipole moment of the laser transition (μ), V_{eff} is an effective volume of the cavity mode, $\mathbf{E}_m(\mathbf{r})$ is the cavity mode electric field profile, and γ_e is an effective excited electronic state decay rate which includes such effects as the broadening due to the energy distribution of carriers in the upper and lower laser transition levels (assumed much faster than the cavity mode decay rate). The spontaneous emission rate into the cavity mode, $R_{\text{sp},m}$, is equal to the stimulated emission (absorption) rate per photon into the cavity mode from a single occupied excited (ground) electronic state, which yields for the modal gain *per-unit-time*,

$$\langle G_m \rangle_t = \int_V (n_e - n_g) R_{\text{sp},m}(\mathbf{r}) \mathrm{d}^3\mathbf{r}, \tag{A.15}$$

where n_e and n_g are the upper (excited) and lower (ground) state carrier densities (per unit volume) of the laser transition, respectively. If we assume that n_e and n_g are constant in the active region volume (V_a) and zero elsewhere, we can write for the modal gain per-unit-time,

$$\langle G_m \rangle_t \approx \left[\frac{(n_e - n_g)|e|^2 |\langle \hat{z} \rangle|^2 \omega}{\hbar\gamma_e} \right] \left[\frac{\int_{V_a} |\mathbf{E}_m(\mathbf{r})|^2 \mathrm{d}^3\mathbf{r}}{\int_V \varepsilon_0 n^2(\mathbf{r}) |\mathbf{E}_m(\mathbf{r})|^2 \mathrm{d}^3\mathbf{r}} \right]. \tag{A.16}$$

Typically, for waveguide-based laser cavities (Fabry-Perot or otherwise) one deals with a modal gain *per unit length*, which is related to the derived modal gain per-unit-time through the group (energy) velocity of the laser mode ($v_g = c/n_g$),

$$\langle G_m \rangle_l = \frac{\langle G_m \rangle_t}{v_g} \approx \left[\frac{2\pi(n_e - n_g)|e|^2 |\langle \hat{z} \rangle|^2 n_g}{(\hbar\gamma_e)\lambda_0 \varepsilon_0 n_a^2} \right] \Gamma_a, \tag{A.17}$$

where we have assumed that the refractive index of the active region is a constant, n_a, and Γ_a is the active region confinement factor,

$$\Gamma_a = \frac{\int_{V_a} \varepsilon_0 n_a^2 |\mathbf{E}_m(\mathbf{r})|^2 \mathrm{d}^3\mathbf{r}}{\int_V \varepsilon_0 n^2(\mathbf{r}) |\mathbf{E}_m(\mathbf{r})|^2 \mathrm{d}^3\mathbf{r}}. \tag{A.18}$$

The carrier density population of the upper and lower levels of the laser transition in the QC active region can be related to the current density flowing through the active region. Following Ref. [118], the steady-state current density (neglecting stimulated emission) is approximately,

$$J = \frac{e(n_3 - n_2)}{\tau_3(1 - \tau_2/\tau_{32})}, \tag{A.19}$$

where n_3 and n_2 are the sheet carrier densities (per unit area) of the upper (3) and lower (2) energy levels of the laser transition, τ_3 is the *total* lifetime of the upper state, τ_{32} is the effective lifetime corresponding to decay of the upper level into the lower level, and τ_2 is the lifetime corresponding to decay out of the lower state. One can relate the sheet densities of state 3 and 2 to the effective volumetric carrier densities n_e and n_g of eq. (A.17) by dividing through by the length of a single "step" of the cascaded active region, L_p. Doing so yields finally for the modal gain per unit length,

$$\langle G_m \rangle_l = \left(J \left[\frac{(2\pi)\tau_3(1 - \tau_2/\tau_{32})|e||\langle \hat{z} \rangle|^2}{L_p(\hbar\gamma_e)\lambda_0 \varepsilon_0 n_a} \right] \right) \left(\frac{n_g}{n_a} \right) \Gamma_a.. \tag{A.20}$$

The term in square brackets of eq. (A.20) corresponds to the aforementioned differential modal gain constant g'_m,

$$g'_m \equiv \frac{(2\pi)\tau_3(1 - \tau_2/\tau_{32})|e||\langle \hat{z} \rangle|^2}{L_p(\hbar\gamma_e)\lambda_0 \varepsilon_0 n_a}. \tag{A.21}$$

Note that we have purposely separated the laser mode parameters, such as confinement to the active region and energy velocity, from the electronic material properties in g'_m. g'_m is thus a purely material property of the QC active region, independent of the guided wave properties of the laser structure.

We are now in a position to derive several *figures of merit* describing the suitability of a QC laser cavity structure for performing near-field sensing. The classical lasing threshold occurs at the point where modal gain is equal to modal loss, which allows us to relate the absorptive shift caused by

a dielectric perturbation of the laser cladding to a shift in the threshold current density of the laser. The total modal loss consists of an intrinsic loss component (α_i), an effective mirror loss component (α_m; equal to $-\ln(R)/L_c$ for a Fabry-Perot cavity with mirror power reflectivity R and cavity length L_c), and the added loss due to the external cladding perturbation ($\bar{\alpha}_e$ of eq. (A.8)). Substituting eq. (A.21) into (A.20) and equating modal loss to modal gain, the threshold current density is found to be equal to,

$$J_{th} \cong \frac{\alpha_i}{g'_m(n_g/n_a)\Gamma_a}\left(1+\frac{\alpha_m+\bar{\alpha}_e}{\alpha_i}\right) = \frac{\alpha_i}{g'_m(n_g/n_a)\Gamma_a}\left(1+\frac{\alpha_m+(n_g/n_0)\alpha_e\Gamma_e}{\alpha_i}\right). \tag{A.22}$$

The overall threshold current density scales inversely with,

$$\Pi = \frac{(n_g/n_a)\Gamma_a}{\alpha_i}, \tag{A.23}$$

the conventional figure of merit used to assess QC laser cavity structures. A figure of merit describing the absorptive sensitivity of a given QC laser cavity design can similarly be defined:

$$\Lambda_e = \frac{(n_g/n_0)\Gamma_e}{\alpha_i}, \tag{A.24}$$

where the fractional change in threshold current is equal to $\Delta J_{th}/J_{th,0} = \alpha_e\Lambda_e$. Π may be viewed as an effective propagation length of light in the bare laser cavity, whereas Λ_e is an effective path length that laser light traverses in the external perturbing medium. Both of these parameters depend upon the wavelength of operation through α_i (just as g'_m scales with $1/\lambda_0$, so to will α_i). Unitless, universal figures of merit may then be defined as,

$$\bar{\Pi} = \left(\frac{2\pi}{\lambda_0/n_a}\right)\Pi = \Gamma_a Q_i, \tag{A.25}$$

$$\bar{\Lambda}_e = \left(\frac{2\pi}{\lambda_0/n_0}\right)\Lambda_e = \Gamma_e Q_i, \tag{A.26}$$

where Q_i is the intrinsic Q-factor of the laser cavity ($\omega/Q_i = (c/n_g)\alpha_i$).

For laser cavities which are not simple linear waveguides, such as many microcavity resonators, it is typically more effective to consider per-unit-time quantities as opposed to per unit length ones. The energy loss per-unit-time of the laser cavity mode is given by,

$$\gamma_T = \omega\left(\frac{1}{Q_i} + \frac{1}{Q_e}\right), \tag{A.27}$$

where Q_i is the intrinsic Q-factor of the laser cavity and Q_e is the Q-factor associated with optical loss from the presence of an external cladding perturbation. Eq. (A.7) relates Q_e directly to the imaginary part of the index of refraction of the external cladding perturbation. Defining a per-unit-time differential material gain constant, $\langle g'_m \rangle_t = (c/n_a) g'_m$, and equating the modal gain rate to the modal loss rate, one finds a threshold current density given by,

$$J_{th} \cong \frac{\omega}{\langle g'_m \rangle_t \Gamma_a Q_i}\left(1 + \frac{Q_i}{Q_e}\right) \cong \frac{\omega}{\langle g'_m \rangle_t \Gamma_a Q_i}\left(1 + \Gamma_e Q_i \frac{2\Delta n_i}{n_0}\right). \tag{A.28}$$

This yields directly the unitless figures of merit, $\bar{\Pi} = \Gamma_a Q_i$ and $\bar{\Lambda}_e = \Gamma_e Q_i$.

Appendix B

Electrically Pumped Laser Epitaxy and Thermal Parameters

Table B.1: Epitaxy for medium thickness p-clad 1.3 micron DIODE laser (5 InAsP QWs). 1.12Q stands for quaternary GaInAsP layers, lattice matched to InP, with photoluminescence peak at 1.12μm ($Ga_{0.15}In_{0.85}As_{0.32}P_{0.68}$).

Layer		Materials	Strain (rel. to InP)	Thickness	Doping (cm^{-3})
Ohmic contact		$Ga_{0.47}In_{0.53}As$:Be	unstrained	500Å	4×10^{19}
Top cladding		1.12Q:Be	unstrained	550Å	1×10^{18}
Separate confinement		1.12Q	unstrained	810Å	undoped
Active region	5 wells	$InAs_{0.48}P_{0.52}$	1.5% compressive	60Å	undoped
	4 barriers	$Ga_{0.24}In_{0.76}As_{0.32}P_{0.68}$	0.65% tensile	120Å	undoped
Separate confinement		1.12Q	unstrained	810Å	undoped
Bottom cladding		1.12Q:Si	unstrained	550Å	8×10^{17}
Lower cladding		InP:Si	unstrained	2400Å	8×10^{17}
Substrate		InP:S	unstrained	N/A	$(0.5-2)\times10^{18}$

Table B.2: Thermal properties used in joule heating FEM simulations. Properties for semiconductor layers are from reference [7]. Thermal conductivity for silver is from reference [8]

Layer	Heat Conductivity κ ($Wm^{-1}k^{-1}$)	Heat Capacity c ($Jg^{-1}K^{-1}$	density ρ (g cm^{-3})	electrical conductivity (S/m)
Silver	429	235.1	10500	6.14×10^{7}
Ohmic contact	2.5	300	5500	1.47×10^{3} [75]
Top cladding	40	310	4810	4.8e3 [76]
Separate confinement	4.4	320	5050	3.15×10^{-1}
Active	0.5	310	5550	3.15×10^{-1}
Separate confinement	4.4	320	5050	3.15×10^{-1}
Bottom cladding	40	310	4810	3.52×10^{4} [76]
Lower cladding	40	310	4810	2.88×10^{4} [77]
Substrate	40	310	4810	3.6×10^{4} [77]

Appendix C

List of Publications

R. Perahia, T. P. Mayer Alegre, A. Safavi-Naeini, and O. Painter, "Surface plasmon mode hybridization in sub-wavelength microdisk lasers" (in preparation, APL)

R. Perahia, V. Moreau, R. Colombelli, O. Painter, "Design of quantum cascade lasers for intracavity sensing in the mid infrared" (in preparation, OE)

K. Srinivasan, C. P. Michael, R. Perahia, and O. Painter, "Investigations of a coherently driven semiconductor optical cavity QED system", Physical Review A (Atomic, Molecular, and Optical Physics) 78, 033839 (2008).

V. Moreau, R. Colombelli, R. Perahia, O. Painter, L. R. Wilson, and A. B. Krysa, "Proof-of-principle of surface detection with air-guided quantum cascade lasers", Optics Express 16, 6387 (2008).

Q. Lin, T. J. Johnson, R. Perahia, C. P. Michael, and O. J. Painter, "A proposal for highly tunable optical parametric oscillation in silicon micro-resonators", Optics Express 16, 10596 (2008).

V. Moreau, M. Bahriz, R. Colombelli, R. Perahia, O. Painter, L. R. Wilson, and A. B. Krysa, "Demonstration of air-guided quantum cascade lasers without top claddings", Optics Express 15, 14861 (2007).

M. Eichenfield, C. P. Michael, R. Perahia, and O. Painter, "Actuation of micro-optomechanical systems via cavity-enhanced optical dipole forces", Nature Photonics 1, 416 (2007).

K. T. Posani, V. Tripathi, S. Annamalai, N. R. Weisse-Bernstein, S. Krishna, R. Perahia, O. Crisafulli, and O. J. Painter, “Nanoscale quantum dot infrared sensors with photonic crystal cavity”, Applied Physics Letters 88 (2006).

Bibliography

[1] L. M. Miller, G. D. Smith, and G. L. Carr. Synchroton-based biological microspectroscopy: From the mid-infrared through the far-infrared regimes. *J. of Bio. Phys.*, 29(2) 219–230, 2003.

[2] L. M. Miller, P. Dumas Nd N. Jamin, J. L. Teillaud, J. Miklossy, and L. Forro. Combining IR spectroscopy with fluorescence imagin in a single microscopoe: Biomedial applications using a synchotron infrared source. *Rev. Sci. Inst.*, 73(3) 1357–1360, March 2002.

[3] O. Crescenzi, S. Tomaselli, R. Guerrini, S. Salvadori, A. M. D'Ursi, P. A. Temussi, and D. Picone. (pdb protein bank id: 1iyt), solution structure of the alzheimer amyloid beta-peptide (1-42) in an apolar microenvironment. similarity with a virus fusion domain. *Euro. J. Bio. Chem.*, 269 5642–5648, 2002.

[4] K. Srinivasan and O. Painter. Mode coupling and cavity—quantum-dot interactions in a fiber-coupled microdisk cavity. *Phys. Rev. A*, 75(023814), February 2007.

[5] K. Srinivasan, C. P. Michael, R. Perahia, and O. Painter. Investigations of coherently driven semiconductor optical cavity QED system. *Phys. Rev. A*, 78(033839), September 2008.

[6] A. B. Krysa, I. S. Roberts, R. P. Green, L. R. Wilson, H. Page, M. Garcia, and J. W. Cockburn. MOVPE-grown quantum cascade lasers operating at similar to 9μm wavelength. *J. Crystal Growth*, 272(1–4) 682–685, December 2004.

[7] C. Zhu, Y. G. Zhang, and Y. L. Zheng. Comparison of thermal characteristics of antimonide and phosphide MQW lasers. *Semiconductor Sci. and Tech.*, 20(6) 563–567, June 2005.

[8] D. R. Lide. *CRC Handbook of Chemistry and Physics*. CRC Press, Tylor & Francis Group, Boca Raton, 87th edition, 2006.

[9] C. Gmachl, F. Capasso, D. L. Sivco, and A. Y. Cho. Recent progress in quantum cascade lasers and applications. *Rep. Prog. Phys*, 64 1533, 2001.

[10] R. Colombelli, K. Srinivasan, M. Troccoli, O. Painter, C. Gmachl, D. M. Tennant, A. M. Sergent, D. L. Sivco, A. Y. Cho, and F. Capasso. Quantum cascade surface-emitting photonic crystal laser. *Science*, 302 1374, November 2003.

[11] M. Eichenfield, C. P. Michael, R. Perahia, and O. Painter. Actuation of micro-optomechanical systems via cavity-enhanced optical dipole forces. *Nature Photonics*, 1(7) 416–422, July 2007.

[12] W.-Y Hwang, J.N. Baillargeon, S. N. G. Chu, P. F. Sciortino, and A. Y. Cho. GaInAsP/InP distributed feedback lasres grown directly on grated substrates by solid-source molecular beam epitaxy. *J. Vac. S. Tech. B*, 16(3) 1422–1425, May 1998.

[13] K. Srinivasan and O. Painter. Linear and non-linear optical spectrsocopy of a strongly coupled microdisk-quantum dot system. *Nature (London)*, 450(7171) 862–866, December 2007.

[14] J. Faist, F. Capasso, D. L. Sivco, C. Sirtori, A. L. Hutchinson, and A. Y. Cho. Quantum cascade laser. *Science*, 264 553–556, April 1994.

[15] M. Beck, D. Hofstetter, T. Aellen, J. Faist, U. Oesterle, M. Ilegems, E. Gini, and H. Melchior. Continuous wave operation of a mid-infrared semiconductor laser at room temperature. *Science*, 295 301–305, January 2002.

[16] J. Devenson, R. Teissier, O. Cathabard, and A. N. Baranov. InAs/AlSb quantum cascade lasers emitting below 3μm. *Appl. Phys. Lett.*, 90(11) 11111, March 2007.

[17] C. Walther, G. Scalari, J. Faist, H. Beere, and D. Ritchie. Low frequency terahertz quantum cascade laser operating from 1.6THz to 1.8THz. *Appl. Phys. Lett.*, 89(23) 231121–591, December 2006.

[18] J. Faist, C. Gmachl, M. Striccoli, C. Sirtori, D. L. Sivco, and A. Y. Cho. Quantum cascade disk lasers. *Appl. Phys. Lett.*, 69 2456–2458, 1996.

[19] S. Anders, V. Tamosiunas, W. Schrenk, and G. Strasser. Optical modes in mesoscopic quantum cascade ring lasers. *Phys. Rev. B*, 69 73309, February 2004.

[20] S. Hofling, J. Heinrich, H. Hofmann, M. Kamp, J. P. Reithmaier, A. Forchel, and J. Seufert. Photonic crystal quantum cascade lasers with improved threshold characteristics at room temperature. *Appl. Phys. Lett.*, 89(191113) 191113, November 2006.

[21] J. Faist, C. Gmachl, F. Capasso, C. Sirtori, D.L. Sivco, J.N. Baillargeon, and A.Y. Cho. Distributed feedback quantum cascade lasers. *Appl. Phys. Lett.*, 70(20) 2670–2672, May 1997.

[22] J. A. Fan, M. A. Belkin, F. Capasso, S. Khanna, M. Lachb, A. G. Davies, and E. H. Linfield. Surface emitting terahertz quantum cascade laser with double-metal waveguide. *Opt. Express*, 14(24) 11672–11680, November 2006.

[23] W. S. Hobson, F. Ren, U. Mohideen, R. E. Slusher, M. L. Schnoes, and S. J. Pearton. Silicon-nitride encapsulation of sulfide passivated GaAs/AlGaAs microdisk lasers. *J. Vac. Sci. Tech. A*, 13(3) 642–645, May 1995.

[24] K. Tai, T. R. Hayes, S. L. McCall, and W. T. Tsang. Optical measurement of surface recombination in InGaAs quantum well mesa structures. *Appl. Phys. Lett.*, 53(4) 302–303, July 1988.

[25] L. A. Coldren and S. W. Corzine. *Diode Lasers and Photonic Integrated Circuits*. John Wiley & Sons, New York, NY, 1995.

[26] M. Lončar, B. G. Lee, L. Diehl, M. A. Belkin, F. Capasso, M. Giovannini, J. Faist, and E. Gini. Design and fabrication of photonic crystal quantum cascade lasers for optofluidics. *Opt. Express*, 15(8) 4499–4514, April 2007.

[27] M. Bahriz, V. Moreau, J. Palomo, R. Colombelli, D. Austin, J. Cockburn, L. Wilson, A. Krysa, and J. Roberts. Room-temperature operation of $\lambda = 7.5$ μm surface-plasmon quantum cascade lasers. *Appl. Phys. Lett.*, 88 181103–1, 2006.

[28] K. Unterrainer, R. Colombelli, C. Gmachl, F. Capasso, H. Y. Hwang, A. M. Sergent, D. L. Sivco, and A. Y. Cho. Quantum cascade lasers with double metal-semiconductor waveguide resonators. *Appl. Phys. Lett.*, 80(17) 3060–3062, April 2002.

[29] B.S. Williams, S. Kumar, H. Callebaut, Q. Hu, and J.L. Reno. Terahertz quantum-cascade laser at $\lambda \approx 100$ μm using metal waveguide for mode confinement. *Appl. Phys. Lett.*, 83(11) 2124–2126, September 2003.

[30] M. Bahriz, O. Crisafulli, V. Moreau, R. Colombelli, and O. Painter. Design of mid-IR and THz quantum cascade laser cavities with complete TM photonic bandgap. *Opt. Express*, 12(10) 5948–5965, May 2007.

[31] A. A. Kosterev and F. K. Tittel. Chemical sensors based on quantum cascade lasers. *IEEE J. Quan. Elec.*, 38(6) 582–591, June 2002.

[32] C. Gmachl, F. Capasso, R. Kohler, A. Tredicucci, A.L. Hutchinson, D. L. Sivco, J.N. Baillargeon, and A. Y. Cho. The sense-ability of semiconductor lasers. *IEEE Circuits and Devices*, 16 10–18, May 2000.

[33] B. Lendl, J. Frank, R. Schindler, A Muller, M Beck, and J Faist. Mid-infrared quantum cascade lasers for flow injection analysis. *Anal. Chem*, 72(7) 1645–1648, April 2000.

[34] A. Edelmann, C. Ruzicka, J. Frank, B. Lendl, W. Schrenk, E. Gornik, and G. Strasser. Towards functional group-specific detection in high-performance liquid chromatography using mid-infrared quantum cascade lasers. *J. Chrom. A*, 934 123–128, November 2001.

[35] S. Schaden, M. Haberkorn, J. Frank, J. R. Baena, and B. Lendl. Direct determination of carbon dioxide in aqueous solution using mid-infrared quantum cascade lasers. *App. Spec.*, 58(6) 667–670, June 2004.

[36] J.Z. Chen, Z. Liu, C. F. Gmachl, and D. L. Sivco. Silver halide fiber-based evanescent-wave liquid droplet sensing with room tempreature mid-infrared quantum cascade lasers. *Opt. Express*, 13(16) 5953–5960, August 2005.

[37] C. Charlton, A. Katzir, and B. Mizaikoff. Infrared evanescent field sensing with quantum cascade lasers and planar silver halide saveguides. *Anal. Chem.*, 77(14) 4398–4403, 2005.

[38] S. Schaden, A. Domínguez-Vidal, and B. Lendl. Quantum cascade modulation for correction of matrix-induced background changes in aqueous samples. *Appl. Phys. B*, 86(2) 347–351, January 2007.

[39] K. Namjou, S. Cai, E. A. Whittaker, J. Faist, C. Gmachl, F. Capasso, D. L. Sivco, and A. Y. Cho. Sensitive absorption spectroscopy with a room-temperature distributed-feedback quantum-cascade laser. *Opt. Lett.*, 23(3) 219–221, February 1998.

[40] S. Song, S. S. Howard, Z. Liu, A. O. Dirisu, C. F. Gmachl, and C. B. Arnold. Mode tuning of quantum cascade lasers through optical processing of chalcogenide glass claddings. *Appl. Phys. Lett.*, 89 41115, 2006.

[41] L. Diehl, B. G. Lee, P. Behroozi, M. Loncar, M. A. Belkin, F. Capasso, T. Aellen, D. Hofstetter, M. Beck, and J. Faist. Microfluidic tuning of distributed feedback quantum cascade lasers. *Opt. Express*, 14(24) 11660–11667, November 2006.

[42] V. Moreau, M. Bahriz, R. Colombelli, R. Perahia, O. Painter, L. R. Wilson, and A. B. Kyrsa. Demonstration of air-guided quantum cascade lasers without top claddings. *Opt. Express*, 15(22) 14861–14869, October 2007.

[43] E. Palik. *Handbook of Optical Constants of Solids II*. Academic Press., Orlando, Florida, 1991.

[44] M. Borselli, T. J. Johnson, and O. Painter. Measuring the role of surface chemistry in silicon microphotonics. *Appl. Phys. Lett.*, 88 13114, March 2006.

[45] D. Hofstetter, T. Aellen, M. Beck, and J. Faist. High average power first-order distributed feedback quantum cascade lasers. *IEEE Photonics Tech. Lett.*, 12(12) 1610–1612, December 2000.

[46] K. Srinivasan and O. Painter. Fourier space design of high-Q cavities in standard and compressed hexagonal lattice photonic crystals. *Opt. Express*, 11(6) 579–593, March 2003.

[47] K. Srinivasan and O. Painter. Design of two-dimensional photonic crystal defect states for quantum cascade laser resonators. *www.arxiv.org/abs/physics/0410068*, 2004.

[48] R. Colombelli, K. Srinivasan, M. Troccoli, O. Painter, C. Gmachl, D. M. Tennant, A. M. Sergent, D. L. Sivco, A. Y. Cho, and F. Capasso. Fabrication technologies for quantum cascade photonic crystal microlasers. *Nanotechnology*, 15 675–681, March 2004.

[49] K. Srinivasan, O. Painter, R. Colombelli, C. Gmachl, D.M. Tennant, A.M. Sergent, D.L. Sivco, A. Y. Cho., M. Troccoli, and F. Capasso. Lasing mode pattern of a quantum cascade photonic crystal surface-emitting microcavity laser. *Appl. Phys. Lett.*, 84(20) 3990, May 2004.

[50] O. Dial, C. C. Cheng, and A. Scherer. Fabrication of high-density nanostructures by electron beam lithography. *J. Vac. S. Tech. B*, 16(6) 3887–3890, November 1998.

[51] R. P. Green, L. R. Wilson, E. A. Zibik, D. G. Revin, J. W. Cockburn, C. Pfugl, W. Schrenk, G. Strasser, A. B. Kyrsa, J. S. Roberts, C. M. Tey, and A. G. Cullis. High-performance distributed feedback quantum cascade lasers grown by metalorganic vapor phase epitaxy. *Appl. Phys. Lett.*, 85(23) 5529–5531, December 2004.

[52] M. A. Holden and P. S. Cremer. Microfluidic tools for studying the specific binding, adsorption, and displacement of proteins at interfaces. *Annu. Rev. Phys. Chem.*, 56 369–387, 2005.

[53] M. A. Unger, H. P. Chou, T. Thorsen, A. Scherer, and S. R. Quake. Monolithic microfabricated valves and pumps by multilayer soft lithography. *Science*, 288 113–116, April 2000.

[54] V. Moreau, R. Colombelli, R. Perahia, O. Painter, L. R. Wilson, and A. B. Krysa. Proof-of-principle of surface detection with air-guided quntum cascade lasers. *Opt. Express*, 16(9) 8387–6396, April 2008.

[55] V. Moreau, M. Bahriz, R. Colombelli, P. A. Lemoine, Y. De Wilde, L. R. Wilson, and A. B. Krysa. Direct imaging of a laser mode via midinfrared near-field microscopy. *Appl. Phys. Lett.*, 90(20) 201114, May 2007.

[56] M. A. Belkin, M. Loncar, B. G. Lee, C. Pflugl, R. Audet, L. Diehl, F. Capasso, D. Bour, S. Corzine, and G. Hofler. Intra-cavity absorption spectroscopy with narrow-ridge microfluidic quantum cascade lasers. *Opt. Express*, 15(18) 11262, September 2007.

[57] Y. Yamamoto and R. E. Slusher. Optical processes in microcavities. *Physics Today*, 46(6) 66–73, June 1993.

[58] P. R. Rice and H. J. Carmichael. Photon statistics of a cavity-QED laser: A comment on the laser-phase transition analogy. *Phys. Rev. A*, 50(5) 4318–4329, November 1994.

[59] C. H. Henry. Phase noise in semiconductor lasers. *J. Lightwave Tech.*, 4(3) 298–311, March 1986.

[60] G. Björk, A. Karlsson, and Y. Yamamoto. On the line width of lasers. *Appl. Phys. Lett.*, 60(3) 304–306, January 1992.

[61] U. Mohideen, R. E. Slusher, F. Jahnke, and S. W. Koch. Semiconductor Microlaser Linewidths. *Phys. Rev. Lett.*, 73(13) 1785–1788, September 1994.

[62] G. P. Agrawal and G. R. Gray. Intensity and phase noise in microcavity surface-emitting semiconductor lasers. *Appl. Phys. Lett.*, 59(4) 399–401, July 1991.

[63] K. Vahala and A. Yariv. Semiclassical theory of noise in semiconductor lasers part II. *IEEE J. Quan. Elec.*, 19(6) 1102–1109, 1983.

[64] A. F. J. Levi, S. L. McCall, S. J. Pearton, and R. A. Logan. Room temperature operation of submicrometre radius disk laser. *IEEE Elec. Lett.*, 29(18) 1666–1667, September 1993.

[65] S. L. McCall, A. F. J. Levi, R. E. Slusher, S. J. Pearton, and R. A. Logan. Whispering-gallery mode lasers. *Appl. Phys. Lett.*, 60(3) 289–291, January 1992.

[66] R. E. Slusher, A. F. J. Levi, U. Mohideen, S. L. McCall, S. J. Pearton, and R. A. Logan. Threshold characteristics of semiconductor microdisk lasers. *Appl. Phys. Lett.*, 63(10) 1310–1312, 1993.

[67] T. Baba, M. Fujita, A. Sakai, M. Kihara, and R. Watanabe. Lasing characteristics of GaInAsP-InP strained quantum-well injection lasers with diameter of 2-10 μm. *IEEE Photonics Tech. Lett.*, 9(7) 878–880, July 1997.

[68] W. L. Barnes, A. Dereux, and T. W. Ebbesen. Surface plasmon subwavelength optics. *Nature*, 424 824–830, August 2003.

[69] C. Sirtori, C. Gmachl, F. Capasso, J. Faist, D. L. Sivco, A. L. Hutchinson, and A. Y. Cho. Long-wavelength ($\lambda \approx 8 - 11.5\mu$m) semiconductor lasers with waveguides based on surface plasmons. *Opt. Lett.*, 23(17) 1366–1368, September 1998.

[70] R. F. Oulton, V. J. Sorger, D. A. Genov, D. F. P. Pile, and X. Zhang. A hybrid plasmonic waveguide for subwavelength and long-range propagation. *Nature Photonics*, 2(8) 496–500, August 2008.

[71] M. T. Hill, Y. S. Oei, B. Smalbrugge, Y. Zhu, T. De Vries, P. J. Veldhoven, F. W. M. Van Otten, J. P. Turkiewicz, H. De Waardt, E. J. Geluk, S. H. Kwon, Y. H. Lee, R. Notzel, and M. K. Smit. Lasing in metallic-coated nanocavities. *Nature Photonics*, 1(10) 589–594, October 2007.

[72] B. K. Min, E. Ostby, V. Sorger, E. Ulin-Avita, L. Yang, X. Zhang, and K. Vahala. High-Q surface-plasmon-polariton whispering-gallery microcavity. *Nature (London)*, 457(7228) 455, January 2009.

[73] K. Srinivasan, P. E. Barclay, O. Painter, J. Chen, and A. Y. Cho. Fabrication of high-Q photonic crystal microcavities in InAsP/InGaAsP multi-quantum well membranes. *J. Vac. S. Tech. B*, 22(3) 875, May 2004.

[74] P. B. Johnson and R. W. Christy. Optical constants of the noble metals. *Phys. Rev. B*, 6(12) 4370–4379, December 1972.

[75] T. Kaneto, K. W. Kim, and M. A. Littlejohn. A comparison of minority electron transport in $In_{0.53}Ga_{0.47}As$ and GaAs. *Appl. Phys. Lett.*, 63(1) 48–50, 1993.

[76] K. Tappura. Electrical and optical properties of GaInAsP grown by gas-source molecular beam epitaxy. *J. Appl. Phys.*, 74(7) 4565–4570, October 1993.

[77] D. A. Anderson, N. Apsley, P. Davies, and P. L. Giles. Compensation in heavily doped N-type InP and GaAs. *J. Appl. Phys.*, 58(8) 3059–3067, October 1985.

[78] L. Vj, N. P. Kobayashi, W. Wu, M. Saif Islam, N. X. Fang, S. Y. Wang, and R. S. Williams. Smooth Ag film deposited using e-beam evaporated Ge as an intermediate layer for applications in nanoscale devices and optical superlens. *Mater. Res. Soc. Symp. Proc.*, 990(0990-B08-18), 2007.

[79] C. P. Michael, M. Borselli, T. J. Johnson, C. Chrystal, and O. Painter. An optical fiber-taper probe for wafer-scale microphotonic device characterization. *Opt. Express*, 15(8) 4745–4752, April 2007.

[80] K. Srinivasan and O. Painter. Optical fiber taper coupling and high-resolution wavelength tuning of microdisk resonators at cryogenic temperatures. *Appl. Phys. Lett.*, 90 031114, 2007.

[81] M. Notomi, A. Shinya, S. Mitsugi, G. Kira, E. Kuramochi, and T. Tanabe. Optical bistable switching action of Si high-Q photonic-crystal nanocavities. *Opt. Express*, 13(7) 2678–2687, April 2005.

[82] P. E. Barclay, K. Srinivasan, and O. Painter. Nonlinear response of silicon photonic crystal microcavities excited via an integrated waveguide and fiber taper. *Opt. Express*, 13(3) 801–820, January 2005.

[83] G. P. Agrawal and N. K. Dutta. *Semiconductor Lasers*. Van Nostrand Reinhold, New York, NY, 1993.

[84] Y. Yamamoto and N. Imoto. Internal and external field fluctuations of a laser oscillator: part I-quantum mechanical langenvin treatment. *IEEE J. Quan. Elec.*, QE-22(10) 2032–2042, October 1986.

[85] K. Srinivasan, M. Borselli, O. Painter, A. Stintz, and S. Krishna. Cavity Q, mode volume, and lasing threshold in small diameter AlGaAs microdisks with embedded quantum dots. *Opt. Express*, 14(3) 1094–1105, February 2006.

[86] H. J. Pask, H. D. Summers, and P. Blood. Light-current characteristics of quantum dots with localized recombination. *Appl. Phys. Lett.*, 87(8) 083109, August 2005.

[87] A. L. Schawlow and C. H. Townes. Infraredand optical masers. *Phys. Rev.*, 112(6) 1940–1949, December 1958.

[88] M. Lax. *Physics and Quantum Electronics, P. L. Kelley, B. Lax and P.E. Tannenwald, Eds.* McGraw-Hill, New York, 1966.

[89] M. Lax. Classical Noise v.noise in self sustained oscillators. *Phys. Rev*, 160 290–307, 1967.

[90] C. H. Henry. Theory of the linewidth of semiconductor lasers. *IEEE J. Quan. Elec.*, QE-18(2) 259–264, February 1982.

[91] C. Harder, K. Vahala, and A. Yariv. Measurment of the inewidth enhancement factor α of semiconductor lasers. *Appl. Phys. Lett.*, 42(4) 328–330, February 1983.

[92] E. M. Purcell. Spontaneous emission probabilities at radio frequencies. *Phys. Rev.*, 69 681, 1946.

[93] Kartik Srinivasan. *Semiconductor Optical Microcavities for Chip-Based Cavity QED*. PhD thesis, California Institute of Technology, 2006.

[94] Paul Barclay. *Fiber-coupled nanophotonic devices for nonlinear optics and cavity QED*. PhD thesis, California Institute of Technology, 2007.

[95] G. T. Liu, A. Stintz, H. Li, T. C. Newell, A. L. Gray, P. M. Varangis, K. J. Malloy, and L. F. Lester. The influence of quantum-well composition on the performance of quantum dot lasers using InAs/InGaAs dots-in-a-well (DWELL) structures. *IEEE J. Quan. Elec.*, 36(11) 1272–1279, November 2000.

[96] A. Stintz, G. T. Liu, H. Li, L. F. Lester, and K. J. Malloy. Low-threshold current density 1.3-μm InAs quantum-dot lasers with the dots-in-a-well (DWELL) structure. *IEEE Photonics Tech. Lett.*, 12(6) 591–593, 2000.

[97] L. Mandel and E. Wolf. *Optical Coherence and Quantum Optics*. Cambridge University Press, Cambridge, United Kingdom, 1995.

[98] K. M. Birnbaum, A. Boca, R. Miller, A.D. Boozer, T. E. Northup, and H. J. Kimble. Photon blockade in an optical cavity with one trapped atom. *Nature*, 436 87–90, July 2005.

[99] P. Michler, A. Kiraz, C. Becher, W. V. Schoenfeld, P. M. Petroff, L. Zhang, E. Hu, and A. Imamoglu. A quantum dot single-photon turnstile device. *Science*, 290 2282–2285, December 2000.

[100] C. Santori, M. Pelton, G. Solomon, Y. Dale, and Y. Yamamoto. Triggered single photons from a quantum dot. *Phys. Rev. Lett.*, 86(8) 1502–1505, February 2001.

[101] J. McKeever, A. Boca, A. D. Boozer, R. Miller, J. R. Buck, A. Kuzmich, and H. J. Kimble. Deterministic generation of single photons from one atom trapped in a cavity. *Science*, 303(5666) 1992–1994, February 2004.

[102] J. P. Reithmaier, G. Sek, A. Loffer, C. Hoffman, S. Kuhn, S. Reitzenstein, L. V. Keldysh, V. D. Kulakovskii, T. L. Reinecke, and A. Forchel. Strong coupling in a single quantum dot-semiconductor microcavity system. *Nature*, 432 197–200, November 2004.

[103] P. Michler, A. Imamoglu, M. D. Mason, P. J. Carson, G. F. Strouse, and S. K. Buratto. Quantum correlatin among photons from a single quantum dot at room temperature. *Nature (London)*, 406 968–970, August 2000.

[104] K. Hennessy, A. Badolato, M. Wigner, D. Grace, M. Atature, S. Gulde, S. Falt, E. L. Hu, and A. Imamoglu. Quantum nature of a strongly coupled single quantum dot-cavity system. *Nature (London)*, 445 896–899, February 2007.

[105] E. B. Flagg, A. Muller, J. W. Robertson, S. Founta, D. G. Deppe, M. Xiao, W. Ma, G. J. Salamo, and C. K. Shih. Resonantly driven coherent oscillations in a solid-state quantum emitter. *Nat Phys*, 5(3) 203–207, March 2009.

[106] K. Srinivasan, O. Painter, A. Stintz, and S. Krishna. Single quantum dot spectroscopy using a fiber taper near-field optic. *Appl. Phys. Lett.*, 91(3) 091102, August 2007.

[107] P. E. Barclay, K. Srinivasan, O. Painter, B. Lev, and H. Mabuchi. Integration of fiber-coupled high-Q SiN_x microdisks with atom chips. *Appl. Phys. Lett.*, 89(13) 131108, September 2006.

[108] M. Borselli, T. J. Johnson, and O. Painter. Beyond the Rayleigh scattering limit in high-Q silicon microdisks: theory and experiment. *Opt. Express*, 13(5) 1515–1530, March 2005.

[109] C. J. Sandroff, R. N. Nottenburg, J. C. Bischoff, and R. Bhat. Dramatic enhancement in the gain of a GaAs/AlGaAs heterostructure bipolar-transistor by surface passivation. *Appl. Phys. Lett.*, 51(1) 33–35, July 1987.

[110] E. Yablonovitch, C. J. Sandorff, R. Bhat, and T. Gmitter. Nearly ideal electronic-properties of sulfide coated GaAs-surfaces. *Appl. Phys. Lett.*, 51(6) 439–441, August 1987.

[111] B. J. Skromme, C. J Sandroff, E. Yablonovitch, and T. Gmitter. Effects of passivating ionic films on the photoluminescence properties of GaAs. *Appl. Phys. Lett.*, 51(24) 2022–2024, December 1987.

[112] J. W. Seo, T. Koker, S. Agarwala, and I. Adesida. Etching characteristics of $Al_xGa_{1-x}As$ in $(NH_4)S_x$ solutions. *Appl. Phys. Lett.*, 60(9) 1114–1116, March 1992.

[113] D. Englund, H. Altug, and J. Vučković. Surface-passivated photonic crystal nanocavity laser. *Appl. Phys. Lett.*, 91(7) 071124, August 2007.

[114] T. J. Kippenberg and K. J. Vahala. Cavity Optomechanics: Back-Action at the Mesoscale. *Science*, 321 1172–1176, 2008.

[115] J. Chan, M. Eichenfield, R. Camacho, and O. Painter. Optical and mechanical desing of a "zipper" photonic crystal optomechanical cavity. *Opt. Express*, 17(5) 2802–3817, March 2009.

[116] M. Eichenfield, R. Camacho, J. Chan, K. J. Vahala, and O. Painter. A picogram and nanometer scale photonic crystal opto-mechanical cavity. *arXiv:0812.2953v1 [physics.optics]*, December 2008.

[117] S. G. Johnson, M. Ibanescu, M. A. Skorobogatiy, O. Weisberg, and J. D. Joannaooulos. Perturbation theory for Maxwell's equations with shifting material boundaries. *Phys. Rev. E*, 65(6) 66611, June 2002.

[118] H. C. Liu and F. Capasso. *Intersubband Transitions in Quantum Wells: Physics and Device Applications I, Semiconductors and Semimetals, Vol. 62*. Academic Press, San Diego, 2000.